SECA-TR-90-02

CR-183994

LOX MANIFOLD TEE ANALYSIS

Final Report, Contract NAS8-37285
Report No. SECA-TR-90-02

Prepared for

National Aeronautics and Space Administration
George C. Marshall Space Flight Center
Marshall Space Flight Center, AL 35812

By

Yen-Sen Chen
Peter G. Anderson

SECA, Inc.
3311 Bob Wallace Avenue
Suite 213
Huntsville, AL 35805

March 1990

LOX MANIFOLD TEE ANALYSIS

Final Report, Contract NAS8-37285
Report No. SECA-TR-90-02

Prepared for

National Aeronautics and Space Administration
George C. Marshall Space Flight Center
Marshall Space Flight Center, AL 35812

By

Yen-Sen Chen
Peter G. Anderson

SECA, Inc.
3311 Bob Wallace Avenue
Suite 213
Huntsville, AL 35805

March 1990

TABLE OF CONTENTS

ABSTRACT

A 4000 Hz vibration phenomena has been observed during the test firings of several space shuttle main engines (SSME). Experimental studies of this phenomena suggest that the problem might be associated with vortex shedding from the vanes within the LOX tee manifold. The objective of this study was to determine the unsteady, three-dimensional flow associated with these vanes by computational methods to identify and better understand the 4000 Hz vibration phenomena. A flow solver, FDNS, for the turbulent conservation equations was validated for predicting high-frequency vortex dynamics and used to predict 2-D dimensional and 3-dimensional flows within the LOX tee. 4000 Hz excitation oscillations were predicted for some flows and the entire 3-dimensional flow structure was predicted for LOX tee flow. The complexity of the flow was revealed by this analysis, and computational methods for predicting these high frequency oscillations in future engine systems were established.

INTRODUCTION

A 4000 Hz vibration phenomenon has been observed during the test firings of several space shuttle main engines (SSME). The phenomenon is manifested by high acceleration levels in the longitudinal direction at the gimbal block location, as shown in Fig. 1 for engine 2025 (Ref. 1). Data from engine accelerometers indicate that the vibration is isolated to the gimbal block and main injector head. The LOX manifold for the main injector head consists of a "hot dog" shaped inlet tee as shown in Fig. 2. The purpose of the manifold is to uniformly distribute the flow of oxygen. Turning vanes and slots within the LOX tee are used to control the flow pattern. Possible fluid dynamic contributions to the problem are: turbulence and ballcock instabilities from the MOV (these caused major engine problems and required redesign of earlier engines), vorticies caused by the elbow between the MOV and the tee inlet, vortex shedding at the edges of the turning vanes, and edge tones of the slots. Extensive experimental studies have been conducted to understand the 4000 Hz phenomenon and the flows which contribute to it. This study was undertaken to describe, by computational methods, the complex flows which occur in this subsystem of the SSME.

Based on the limited experimental evidence available at the time, NASA and Rocketdyne implemented a modification to the LOX tee vanes to alleviate the 4000 Hz problem. The opening between the two vanes was enlarged, and the trailing edge of the vanes was sharpened to shift the frequency of the shed vortex system. These modifications reduced the severity of the problem and are still in use. However, the value of understanding these flows in better detail is evident.

Detailed review of hot fire test data revealed that the 4000 Hz oscillation was present in all engines; however, its level

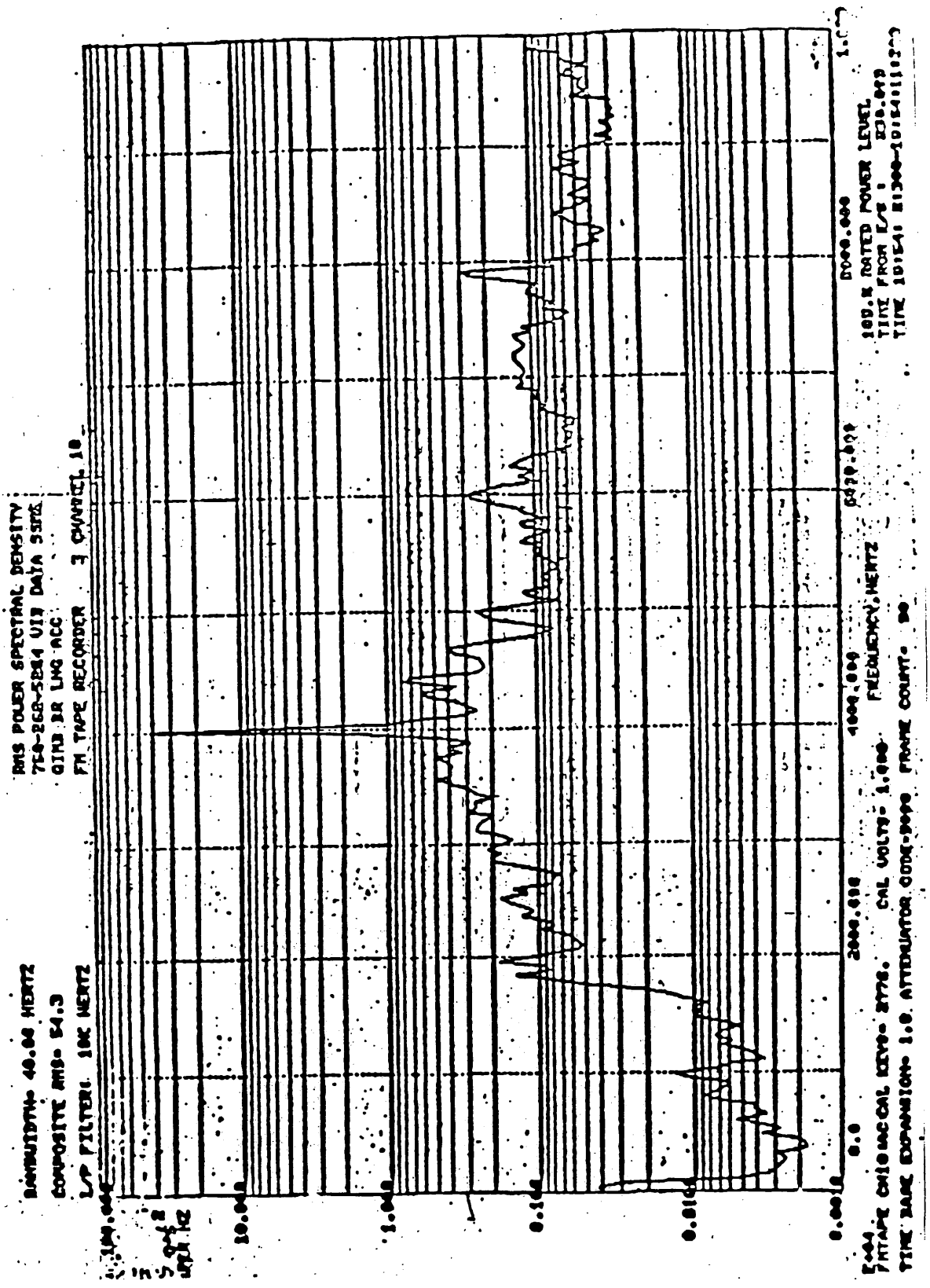

Figure 1. RMS PSD for Engine 2025

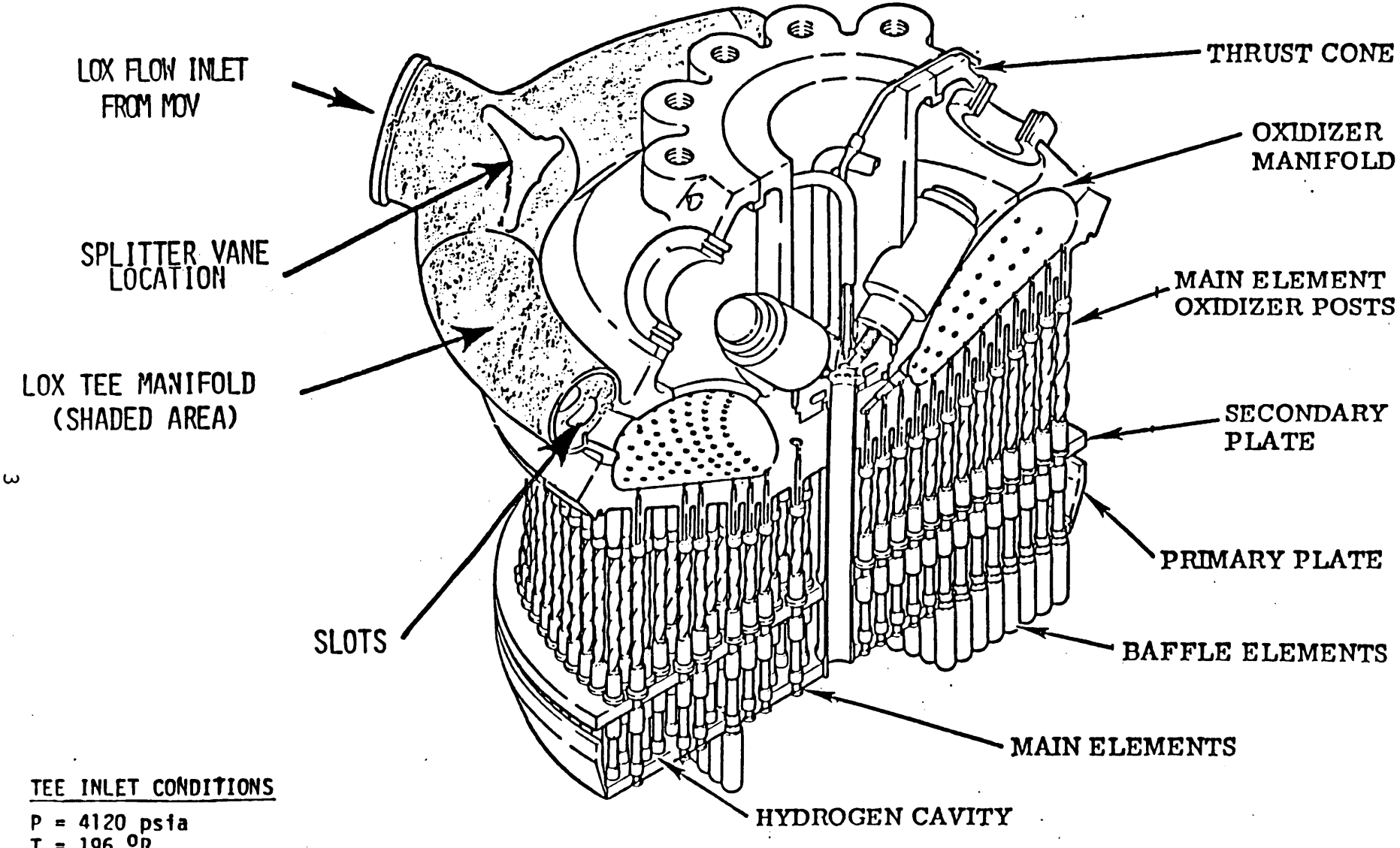

Figure 2. LOX Tee Manifold

TEE INLET CONDITIONS

P = 4120 psia
T = 196 ^{o}R
ρ = 69.6 lbm/ft^3
$\dot{m}$ = 855 lbm/sec
V = 184 ft/sec
q = 1/2 ρV^2 = 254 psia
Dia = 3.5 in

was much smaller in normal engines than in "buzzer" engines. Pressure measurements indicated the oscillations to be stronger between the MOV and LOX tee than within the LOX dome. The large amplitude vibrations showed sharp peaks in the 3600-4000 Hz range; the splitter vane bending and torsion natural frequency modes are 3500 to 4500 Hz. The frequency dropped by as much as 400 Hz during firing and did not return to higher levels on restart. The vibration occurred only during high power level firings. Since the phenomenon did not occur on all engines, it was assumed to be sensitive to slight geometric variations.

Water table experiments and preliminary inviscid, two-dimensional CFD analyses have shown strong vortical flow with smaller vortices in the wake of the vane. Geometric variations to the vane locations had a large effect on this vortex structure. In fact, the water table experiments can be made to exhibit non-symmetric flow behind the vanes by displacing one vane laterally into the flow and then returning it to its original position. The flow thus created was bistable and analogous to diffuser flow (Ref. 2). The significance of this observation has not been determined. None of these studies have shown flow oscillations typical of 4000 Hz frequency.

This study provides a three-dimensional computational fluid dynamic analysis of the unsteady flowfield within the LOX feedline from the MOV, the manifold tee, and the slots. Additional detailed studies of the flowfield near the trailing edge of two-dimensional blades were made to determine the effects of velocity and blade shape on the unsteady character of the flow. Such analyses were required to investigate unsteady loads and possible mechanisms of the 4000 Hz vibration phenomenon.

Incompressible flow for liquids was treated such that real time pressure wave speeds did not compromise the temporal

characteristics of the wake flow. Turbulence models were carefully selected, such that, realistic vortex structures at the trailing edge of the turning vanes were simulated.

The computational methodology required to analyze the unsteady flow in the LOX manifold tee will be discussed in order to establish the critical features which must be correctly simulated and the computation techniques which must be used to yield good results. Appropriate verifications and meaningful sample problem demonstrations were identified and investigated. Details of the computer code required and the results of the computational investigation are presented in the remainder of this report.

APPROACH

SECA's study was directed solely toward investigating the flowfield features which can excite the 4000 Hz vibration. Probably the phenomenon is a fluid/structures interaction, but a sufficiently detailed analysis of the flowfield to identify the flow driving the vibration must treat the structure as rigid in order to be tractable with state-of-the-art CFD methodology. To determine an optimum solution of the problem, the source of the oscillation must be determined. Following such a determination, a rational decision of whether to change the structural dynamics or the flowfield characteristics of the LOX manifold could be made.

The objective of this study was to determine the unsteady, three-dimensional, turbulent flow in the LOX manifold tee.

Ideally, the MOV, the high pressure duct from the MOV to the LOX tee, the LOX tee proper, and at least a portion of the LOX manifold should be included in the computational simulation.

Treating all of these components simultaneously was found to be impractical, therefore the three-dimensional cases analyzed were started at the inlet to the elbow located just upstream of the LOX tee and terminated at the slots between the LOX tee and the LOX manifold. In fact, several very complex problems required solution before meaningful simulations to this restricted region of the flowfield were achieved. Restricting the flow region under consideration, as just stated, should not greatly affect the engineering utility of the analysis.

The flowfield analysis presented herein required that turbulence effects introduced by vorticial flows in the elbow and those arising from interaction with vanes, be evaluated with respect to their possible contribution to the 4000 Hz phenomenon. If minor geometric variations between engines is indeed the explanation of why "buzzers" occur, vane geometry and wall boundary conditions within the LOX tee are crucial to the analysis.

To provide an analysis which describes the required flow detail, a three-dimensional, unsteady, incompressible, turbulent flowfield must be predicted. The solution must be time-accurate, which means that pressure waves must be allowed to travel in the analysis at the rapid sound speeds typical of the supercritical thermodynamic conditions prevalent in the LOX tee. A determination of a suitable flow solver was made, and its validity was verified. In addition to time accurate pressure predictions, boundary condition specifications must not be allowed to introduce computational noise into the solution. Waves adjacent to boundaries must not be produced by numerical error in the algorithm. Proper specification of subsonic boundary conditions was made so that such problems were not encountered.

The critical flow feature, which turbulence models and the solution methodology must correctly predict, is the vortex-induced vibrations from the trailing edge of the turning vane. This places a severe restraint on the type of turbulence model and on the grid density required.

The required simulation was performed by making an evaluation of the CFD code to be used, evaluating the effect of minor vane geometry variations with a two-dimensional calculation, and finally calculating the entire 3-dimensional LOX tee flowfield. These steps will be described in the next sections of this report.

FLOW SOLVER SELECTION

Three concepts are available for obtaining time-accurate solutions of the conservation equations for liquid flow. (1) A thermal equation of state may be used to introduce the actual wave speed for pressure pulses into the system of governing equations. (2) An incompressible, constant density analysis may be made whereby pressure wave speeds are treated as traveling at infinite speeds, i.e. there is no damping due to even small density changes. (3) Subiterations between time steps may be used to allow artificial compressibility methods to relax to obtain time accuracy. The approach proposed for this study was to develop a time-accurate CFD algorithm based on a realistic equation of state and then apply the method to the LOX tee investigation. This development resulted in generating the LWIND code, which is presented in Appendix A. However, before the validation of this code was completed, two other codes became available: INSUP2D and FDNS. INSUP2D was a modification to the NASA/Rocketdyne INS code for incompressible flow using artificial compressibility, which used subiterations to obtain time accuracy (Ref. 3). The equation solved for pressure contains unsteady

terms and a parameter to define the artificial compressibility. Solution of this equation is hyperbolic in nature and results in pressure waves progressing through the computational domain during the course of the solution. The speed of these waves depend on the value of artificial compressibility. The FDNS code (Appendix B) utilizes a pressure based soltuion which solves an approximate Poisson equation for pressure. This equation contains no unsteady terms, and its solution is elliptic like, in that pressure waves have traveled at infinite speed throughout the compututon domain to satisfy the pressure boundary conditions at all points on the boundary of the domain. Rather than belabor the value and degree of approximation used, INSUP2D and FDNS were both used to solve wake flow problems. If such problems could be accurately solved with either or both codes, development would be suspended on the LWIND and the more developed codes would be used. Before this comparison is presented, a discussion of the real fluid thermal equation for LOX will be made.

• The LWIND Code

To describe unsteady, 3-dimensional, turbulent flow of LOX, the interaction of pressure, density and temperature must be accurately simulated. Utilizing the parameters: β, the coefficient of volume expansion, and κ, the isothermal compressibility, the thermal equation of state, as derived in Appendix A, is:

$$P = (\beta T + \ln p - C_\rho)/\kappa$$

For reference conditions of pressure equal to 4000 psia, temperature of 200 °R, and density of 69.13465 lb_m/ft^3, the constants: C_ρ, κ, and β are:

$C\rho$ = 4.59672

κ = 1.3948E-5 (psi^{-1})

β = 2.0823E-3 (R^{-1})

The values of these parameters were obtained from Ref. 4. In general, κ and β are not constant, but are functions of temperature and density. However, the simplified equation of state is useful for determining an upwind algorithm for liquid flow which is approximately isobaric and isothermal.

The more direct approach is to determine an accurate equation of state, such an equation was developed in Ref. 5, based on the methods of Ref. 6. This equation is referred to as the HBMS equation of state, it is lengthly, but explicit for pressure as a function of density and temperature. The HBMS equation is quite accurate for a wide range of liquid and vapor flow conditions, including the supercritical. Although the HBMS equation gives accurate property values, it is too complex to incorporate into an eigenvalue solution for use as a switch in an upwind CFD algorithm. The κ,β equation is adequate for the latter purpose. For problems with large density and temperature variations, the HBMS equation can be used to modify local κ and β values during the course of the computation. It should be noted that artificial compressibility is a numerical parameter which is unrelated to fluid properties through an equation of state. This means that calculated pressure waves would propagate through the medium at a finite, but arbitrary velocity, if artificial compressibility methods were used.

• Evaluation of the INSUP2D and FDNS Codes for Wake Analyses

The incompressible, time-accurate CFD model, INSUP2D, was investigated by comparing computed results to measured vorticial flows, specifically, cylinders in cross-flow. Study of the time-

accurate, high order (5th, 3rd or 1st) upwind INSUP2D code was initiated with the intention of using and modifying this code for extensive use. A test run for a steady laminar flow past a cylinder at Re = 40 was successfully run with the artificial compressibility set equal to 5 and $\Delta\tau = \Delta T = 0.25$. The artificial compressibility is a constant parameter in the equation which relates pressure to the divergence of the velocity field. The residual (divmax) dropped 4 orders of magnitude in 1000 steps. Flow at this Re is steady, as was the calculated result calculated with the unsteady code. The code changes required to generalize the grid to other than cylindrical geometries and to add a turbulence model were identified and implemented. When a case is run, about half a dozen parameters must be specified. As the case is being run, intermediate checks are made to insure that these parameters were set at the proper levels.

As stated previously, the laminar wake behind a circular cylinder for Reynolds number 40 was predicted to be asymmetric by the INSUP2D code. The built-in initial boundary disturbance in subroutine BCIMP, used to initiate vortex shedding, rather than the grid used, caused the asymmetry. The same case was rerun with the initial disturbance turned off. The same steady-state input parameters were used. A steady-state solution was obtained in 2000 time steps. CPU time was 16 min, 16 sec. The results show a much more symmetric wake pattern. See Figs. 3 and 4 for stream function and pressure coefficient contour plots, respectively.

Experimental studies of the Re = 40 case have been presented by Coutanceau and Bouard (Ref. 7). The parameters reported are defined in Fig. 5 and summarized in Table 1. The experiment did not conform exactly to infinite flow around a cylinder because the flow was contained in a large pipe, therefore the

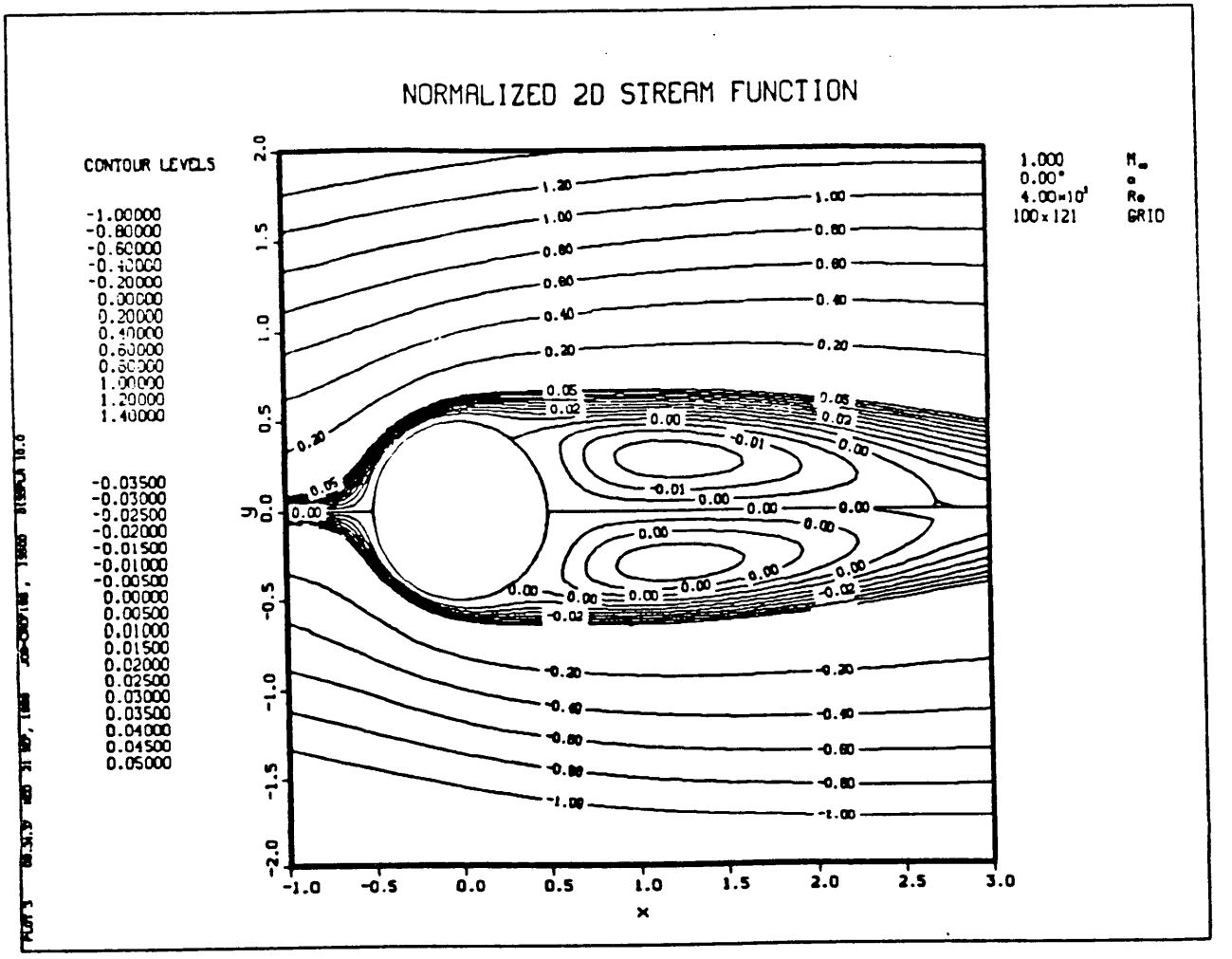

ORIGINAL PAGE IS
OF POOR QUALITY

Figure 3. Streamlines at Re = 40 for a Cylinder in Cross-Flow.

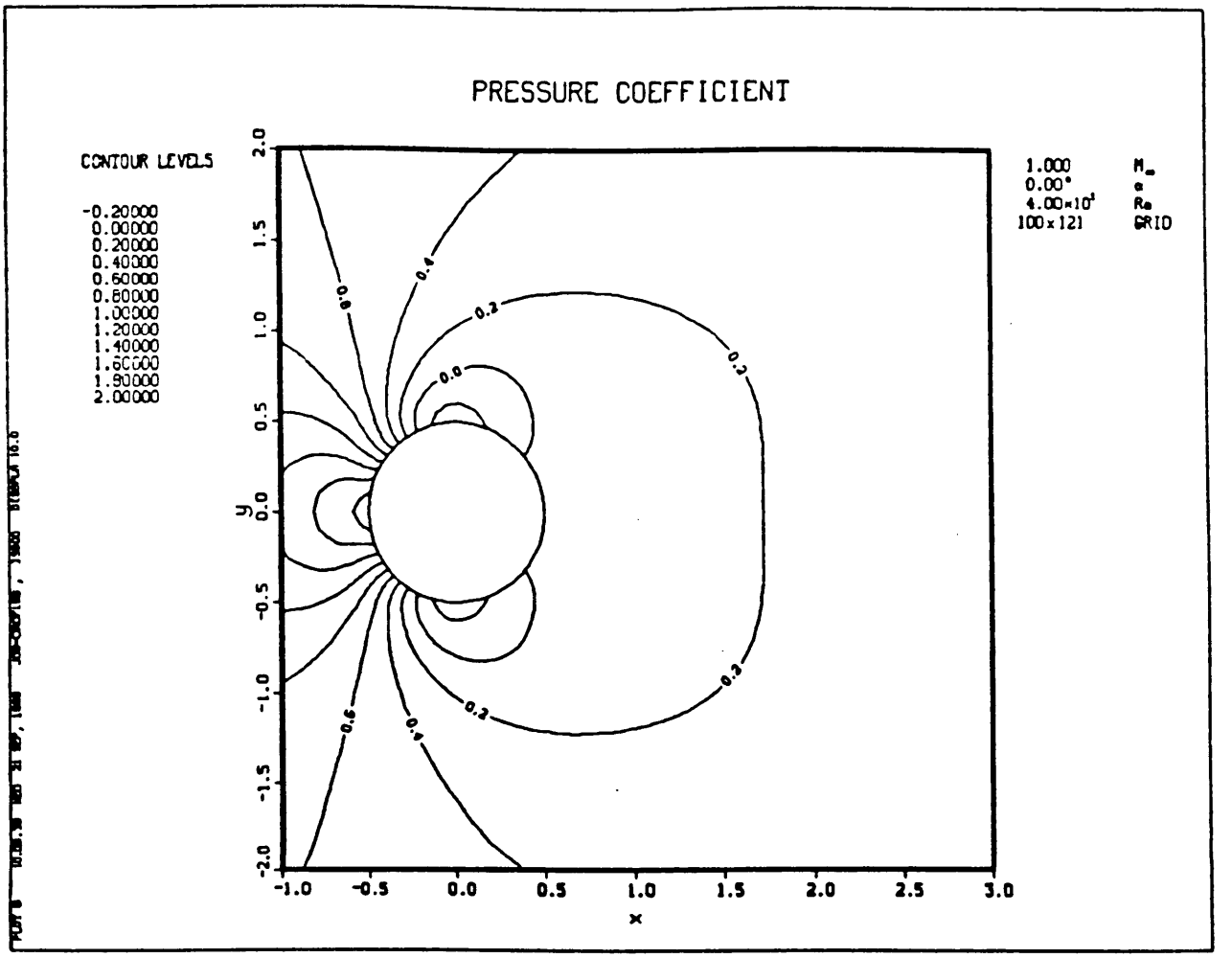

ORIGINAL PAGE IS
OF POOR QUALITY

Figure 4. Pressure Coefficient Contours at Re = 40 for a Cylinder in Cross-Flow.

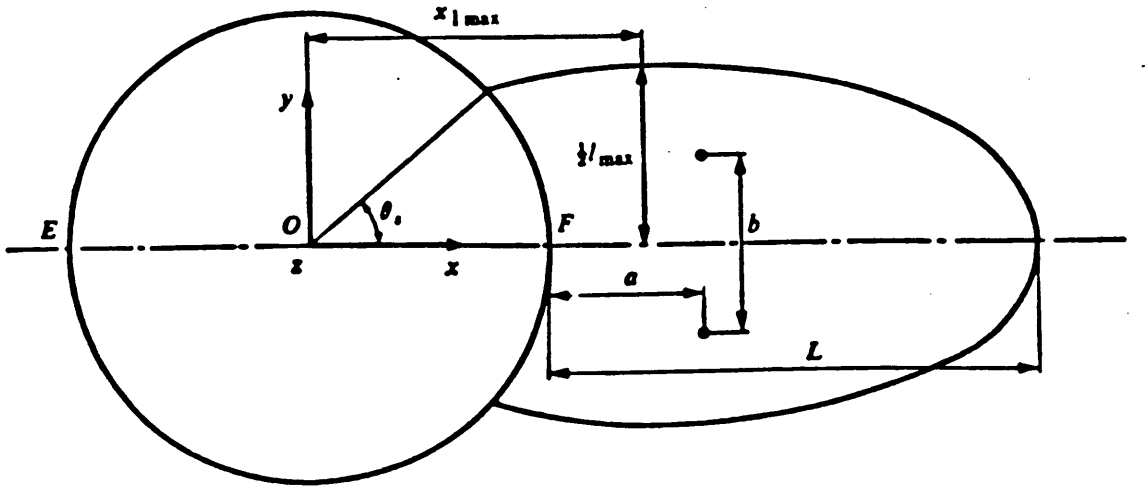

Figure 5. Geometrical parameters of the closed wake for a Cylinder in Cross-Flow.

Table 1. Re = 40 Comparisons

Parameter	Experiment	Prediction
D	1.0	1.0
L	2.13	2.2
a	0.73	0.77
b	0.59	0.57
l_{max}	1.08	1.08
X_{lmax}	0.99	1.0
r_s	53.5°	52.9°
C_D	1.55*	1.48

* from Braza, et al

investigators extrapolated their results to eliminate this effect. Their extrapolated results were compared to several other sets of data from the literature and found to be in good agreement with most of the other investigations. Table 1 also shows the results of the INSUP2D prediction; the prediction is excellent. Experimental results at Re = 10, 15, 20 & 30 were also reported by Coutanceau & Bouard. Qualitatively, all of these tests produced the same closed wakes with standing vorticies. All of the parameters could not be measured for the lower Reynolds number cases. For Reynolds numbers lower than 1, the standing vorticies would not be expected, but such flows are not considered to add to our understanding of the turbulent flows in the LOX tee. Additional cases run in the range of the referenced data should give comparisons very much like those shown in Table 1.

Cases of unsteady wake flow behind the same cylinder for Re = 200 were also simulated using the INSUP2D code. Two cases with and without the initial disturbance imposed were studied. The same mesh system with grid size of 100 x 120 was used. The physical and psuedo-time step sizes assigned were 0.025 and 1.0E10 respectively. The compressibility parameter was 2500.0, and the fifth-order upwind scheme was used. These parameters were suggested by Rogers and Kwak. A nearly periodic solution was obtained after 2000 time steps (CPU time = 5 hrs, 10 min, 10 sec) when the initial disturbance was activated. This results in a Strouhal number of 0.1942. Figs. 6 and 7 show the final stream function plot and pressure coefficient contours. For the second case without using the initial disturbance to generate flow disturbances, no vortex shedding pattern was predicted after 2000 time steps. The two cases, with and without initial boundary disturbances, were calculated until periodic solutions were obtained. With the initial disturbances, the first case produced a periodic solution with a Strouhal number of 0.194 in 2000 time

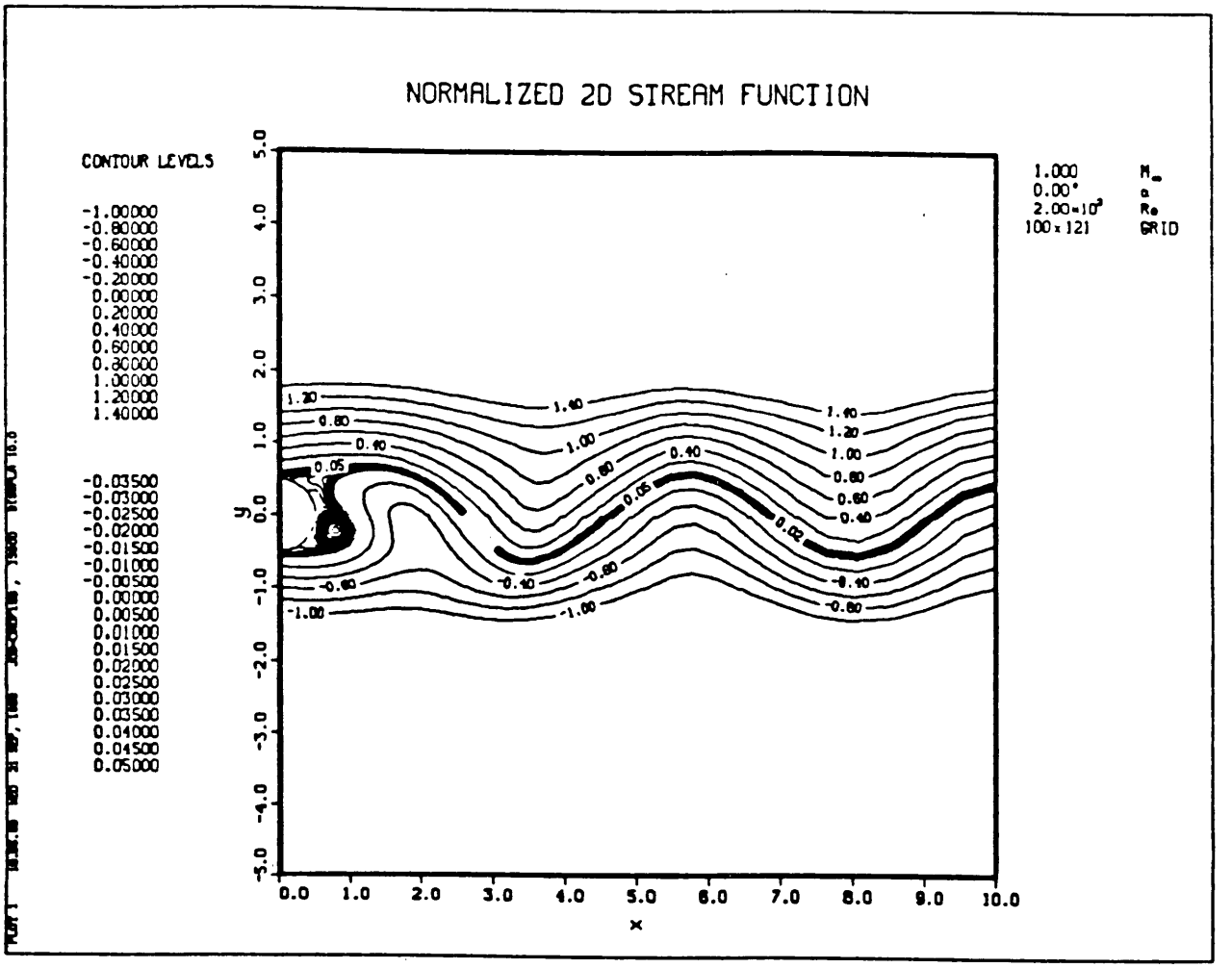

ORIGINAL PAGE IS
OF POOR QUALITY

Figure 6. Streamlines at Re = 200 for a Cylinder in Cross-Flow.

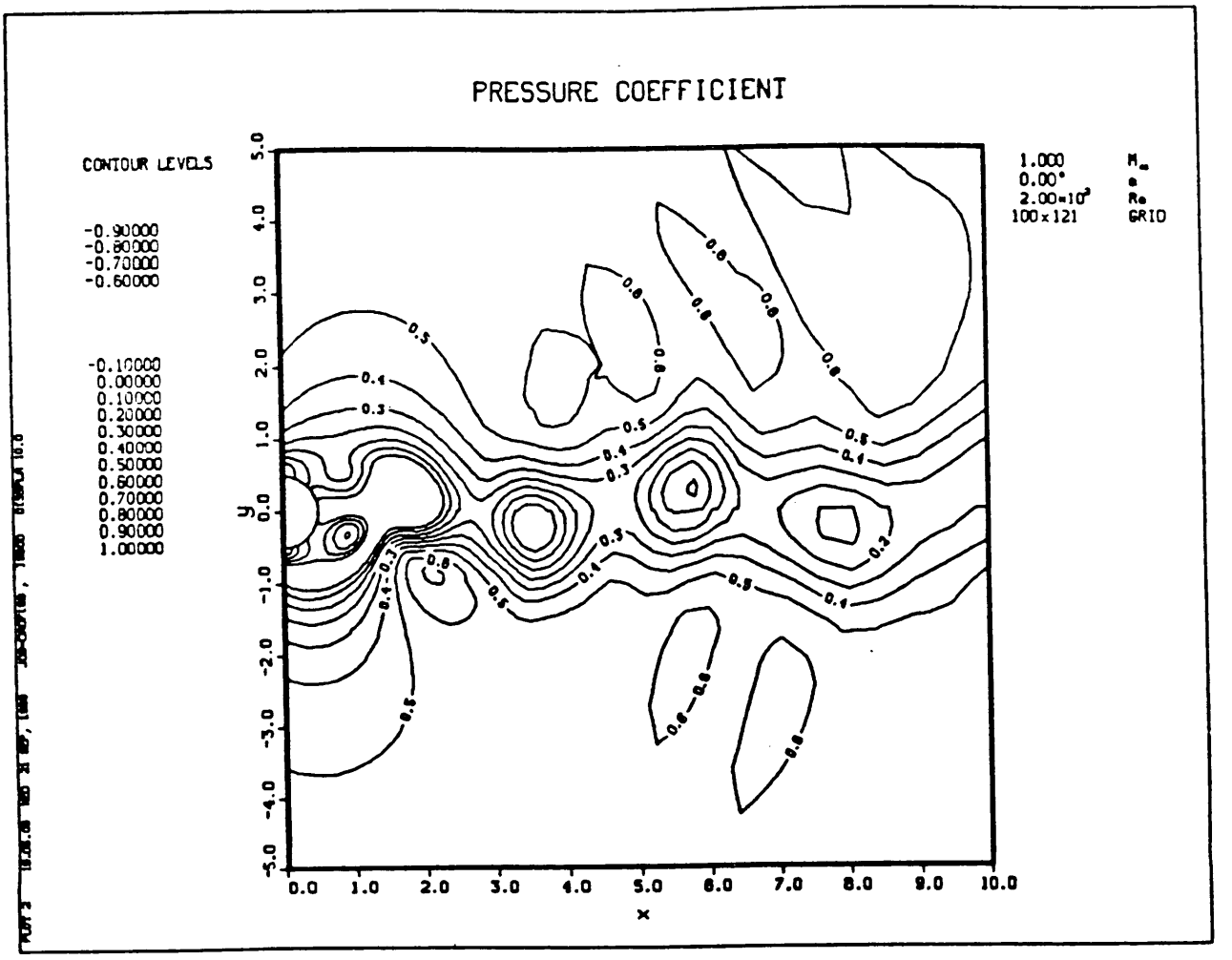

Figure 7. Pressure Cofficient Contour at Re = 200 for a Cylinder in Cross-Flow.

steps. A time step of 0.025 was required and about 5 hours of CPU time on the CRAY-XMP were used. For the second case, the flow started to oscillate at about 2000 time steps; it took another 2000 steps to reach a perodic solution. The overall CPU time for the second case was 7 hrs, 39 min, 46 sec, i.e., 6.89 sec/time step. It was also found that an average of 20 subiterations were required per time step. The same Strouhal number was obtained for both cases. Rogers & Kwak report a Strouhal number of 0.185 for these conditions; they reference a value of 0.194 calculated by Lecointe & Piquet. Experimental data from Schlichting indicate a value of 0.19. The unsteady laminar flow cases were satisfactorily predicted at Re = 200.

Reynolds number 100, 200, & 1000 cases were studied computationally with a laminar model by Braza, Chassaing, & Minh (Ref. 8). The reported Strouhal numbers at Re = 200 was 0.2; Roshko's experimental value was 0.194. SECA calculated a value of 0.194 with INSUP2D. The referenced Re = 1000 case indicated that three types of eddies contributed to the wake: (1) those associated with the separation point, (2) those associated with the free shear layers which separate the free stream from the wake, and (3) the classical Karman vorticies. Laminar, 2-D calculations are only approximate in this flow regime because the wake flow is turbulent and 3-D flow features are of importance. Turbulence models can account for both of these effects, if they are designed to do so. The turbulent energy spectra in the wake of a cylinder at Re = 540 are reviewed by Hinze (Ref. 9). Braza, et al, acknowledge the limitations of the analysis which they present, and they point out that the relative importance of the eddy structures change as the Reynolds number increases. It is known that as the Reynolds number increases, a stable turbulent wake is established with a laminar boundary layer ahead of the separation point on the cylinder, and at further increases the cylinder boundary layer becomes turbulent and the wake decreases

in size (Ref. 10). Classically, the Strouhal number is based on the observed vortex structure in the cylinder wake. Between Re = $5x10^5$ and $4x10^6$, vortex structure is not experimentally observed in the wake of cylinders (Ref. 11). All of these flow features are quite interesting but they can not be addressed computationally with a laminar flow analysis. The Re = 200 case run with INSUP2D was as successful as could be expected without using turbulence models. Other cases for Reynolds numbers up to 200 can be investigated with the original version of the INSUP2D code, which was for laminar, 2-dimensional only. Both of these restrictions must be removed before INSUP2D could be used to describe the LOX tee flow.

- Addition of Turbulence Models to the INSUP2D Code

Algebraic and low-Reynolds number, k-ϵ turbulence models were added to INSUP2D to determine if this code could be useful for simulating LOX tee flow.

The Baldwin-Lomax turbulence model (Ref. 12 AIAA Paper 78-257) was incorporated into INSUP2D. The cylinder in cross-flow was run at a Reynolds number of 10^6 with this turbulence model. Streamlines and pressure coefficient contours are shown in Figs. 8 & 9. The periodicity of the solution is demonstrated with Fig. 10 which shows the oscillation of the lift and drag coefficients. The Strouhal number predicted for this case was 0.29, not the 0.22 expected; therefore, the Baldwin-Lomax model alone does not predict accurate vortex shedding for cylinders. The run time for this case was 14.5 hours.

To improve the turbulence models in INSUP2D, a major effort was devoted to incorporating low-Reynolds number turbulence models into the INSUP2D code. The turbulence modeling constants, source terms, and wall damping functions of Chien's low Reynolds

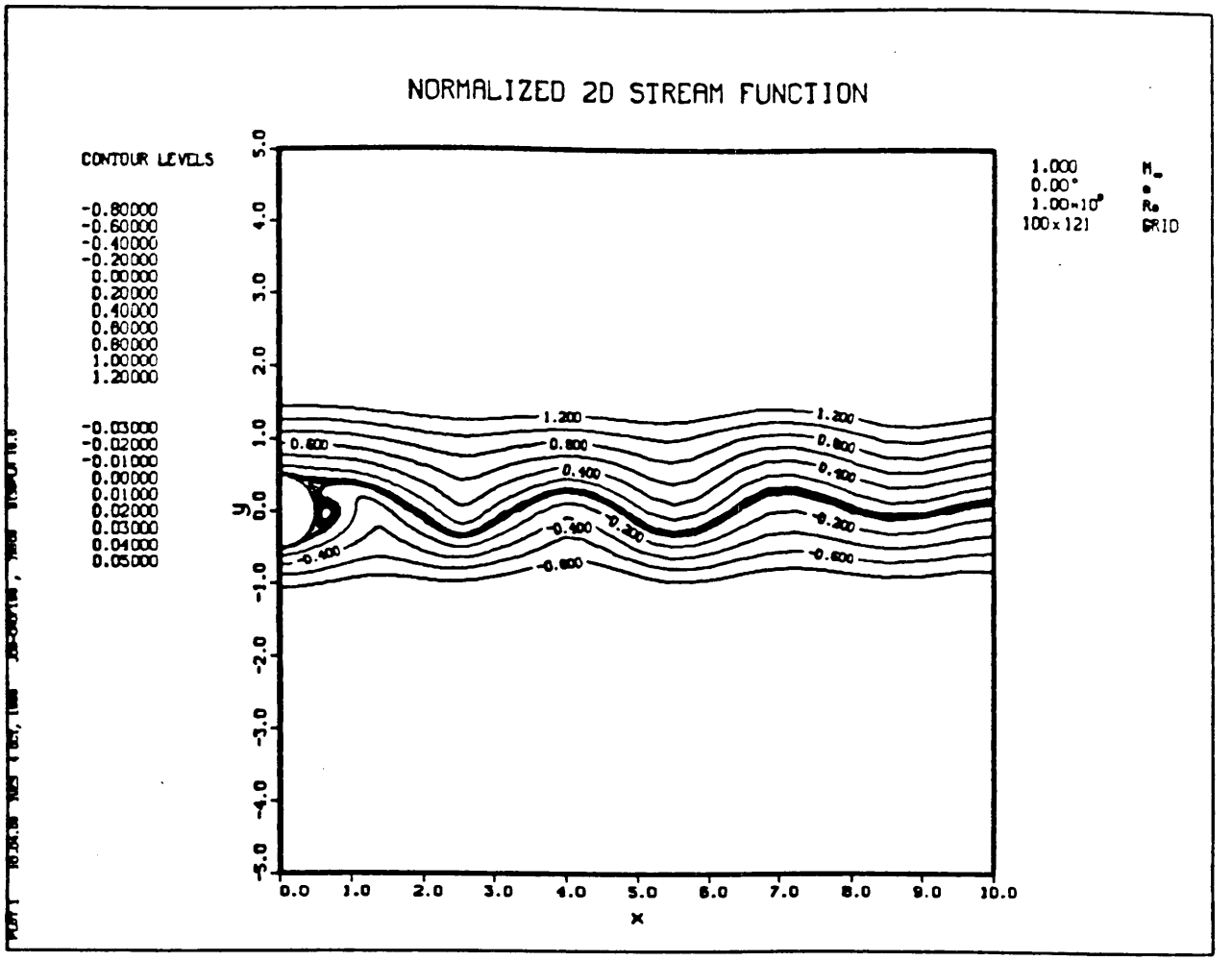

Figure 8. Streamlines at Re = 10^6 for a cylinder in Cross-Flow.

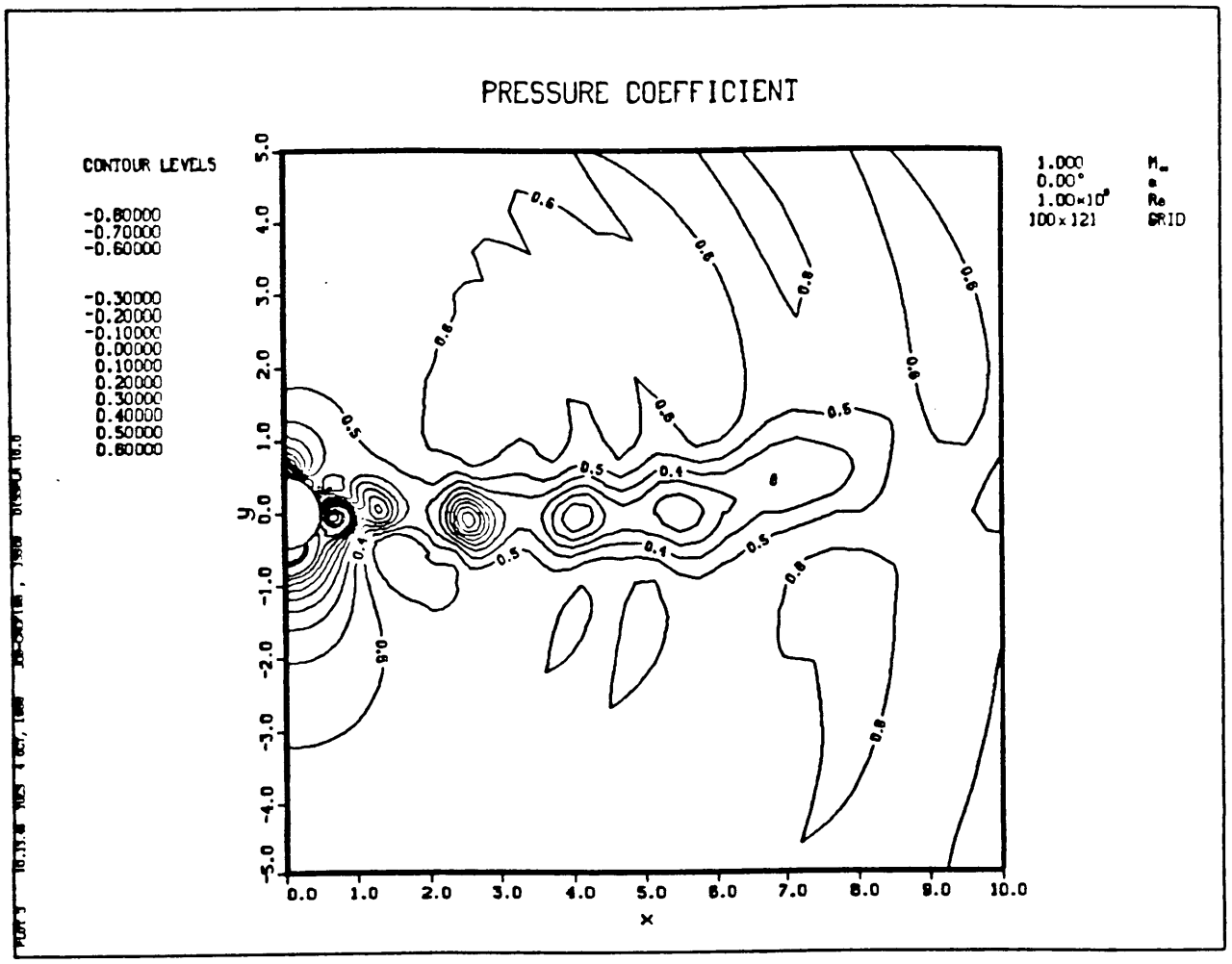

Figure 9. Pressure Coefficient Contours at Re = 10^6 for a Cylinder in Cross-Flow.

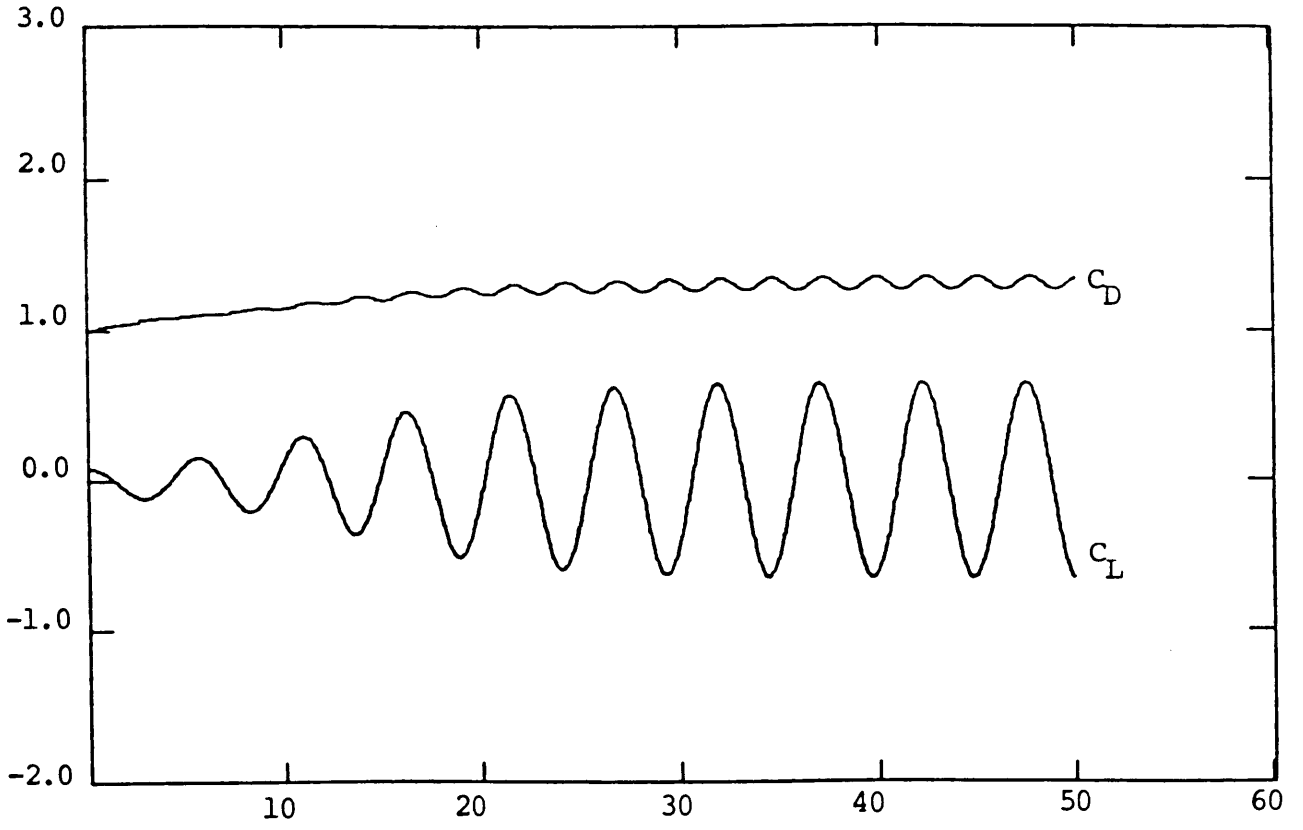

Figure 10. Lift and Drag Coefficients at Re = 10^6 for a Cylinder in Cross-Flow.

number two-equation turbulence model were added to the code (Ref. 13). A turbulence model control parameter, ITURB, was added for the selection of turbulence models. The convection terms and diffusion terms were also added to the code. Standard upwind methods were employed to treat the convection fluxes, and a central differencing scheme was used to approximate the diffusion terms. These left-hand-side terms were assembled and solved in a subroutine called STEPKE.

The basic features and performance of the eight most well known low-Reynolds k-ϵ turbulence models have been reviewed and tested by Patel, et al. (Ref. 14). These turbulence models were compared for several turbulent boundary layer flows with and without pressure gradient effects. All of the two-equation turbulence models considered in this study are summarized in Table 2. No one model was consistently valid for all the cases tested. Patel, et. al., concluded that, in general, the Chien and Lam-Bremhorst models performed the best. Low-Reynolds number turbulence models have not been developed to the point where they are engineering tools, rather they are computational models which must be carefully assessed before each application. For example, So, et al (Ref. 15) have recently suggested an important improvement in treating flows with pressure gradients which is applicable to this study.

The general form of these models can be expressed by:

$$k_t + uk_x + vk_y - (\nu_k k_x)_x - (\nu_k k_y)_y = P_r - \epsilon - D \qquad \text{Eq.1}$$

$$\epsilon_t + u\epsilon_x + v\epsilon_y - (\nu_\epsilon \epsilon_x)_x - (\nu_\epsilon \epsilon_y)_y = (C_1 f_1 P_r - C_2 f_2 \epsilon)\ (\epsilon/k) - E \qquad \text{Eq.2}$$

Table 2. Turbulence Models

The general form of two-equation k-ϵ turbulence models can be written as:

$$\rho D_t k = \nabla[(\mu+\mu_t/\sigma_k)\nabla k] + \rho(P_r-\epsilon+D)$$

$$\rho D_t \epsilon = \nabla[(\mu+\mu_t/\sigma_\epsilon)\nabla \epsilon] + \rho[(\epsilon/k)(C_1 f_1 P_r - C_2 f_2 \epsilon)+E)]$$

where the turbulent viscosity and kinetic energy production rate are given by:

$$\mu_t=\rho C_\mu f_\mu k^2/\epsilon$$

$$P_r=(\mu_t/\rho)[2(u_x^2+v_y^2+w_z^2)+(v_x+u_y)^2+(w_y+v_z)^2+(u_z+w_x)^2-(2/3)(u_x+v_y+w_z)^2]$$

D and E are defined by the following parameters:

R_T = turbulent Reynolds number = $\rho k^2/\mu\epsilon$

R_y = dimensionless distance from the wall = $\rho y\sqrt{(k)}/\mu$

y^+ = another dimensionless distance from the wall

= $\rho y\sqrt{(\tau w/\rho)}/\mu$

Also note: $\lambda \approx \sqrt{(10\nu k/\epsilon)}$

$$p^+=(\mu/\rho^2 u_\tau^3)(\partial_s p)_w$$

$$u_\tau=\sqrt{(\tau_w/\rho)}$$

The turbulence model constants, C_μ, C_1 and C_2, are tuned against basic turbulent flows (e.g. homogeneous turbulence, wall equilibrium conditions, planar and circular jets, etc.). The turbulence Schmidt numbers, σ_k and σ_ϵ, are determined based on the spreading rate of k and ϵ which satisfy the consistency condition.

The model constants and damping functions used in several k-ϵ models are summarized in subsequent pages of this table.

Table 2. Turbulence Models, cont. p.1

Model	standard	extended Chen-Kim	Launder-Sharma
k_w, ϵ_w B.C.	wall functions	wall functions	$k_w = \epsilon_w = 0$
C_μ	0.09	0.09	0.09
C_1	1.44	$1.15+0.25\text{Min}\{3, P_r/\epsilon\}$	1.44
C_2	1.92	1.90	1.92
σ_k	1.0	0.8927	1.0
σ_ϵ	1.3	1.15	1.3
f_μ	1.0	1.0	$\exp\{-3.4(1+R_T/50)^{-2}\}$
f_1	1.0	1.0	1.0
f_2	1.0	1.0	$1-0.3\exp\{-R_T^2\}$
D	0.0	0.0	$-2\nu(\partial_y\sqrt{k})^2$
E	0.0	0.0	$2\nu\nu_t(\partial_{yy}U)^2$

Model	Hassid-Poreh	Hoffman	Dutoya-Michard
k_w, ϵ_w B.C.	$k_w = \epsilon_w = 0$	$k_w = \epsilon_w = 0$	$k_w = \epsilon_w = 0$
C_μ	0.09	0.09	0.09
C_1	1.45	1.81	1.35
C_2	2.0	2.0	2.0
σ_k	1.0	2.0	0.9
σ_ϵ	1.3	3.0	0.95
f_μ	$1-\exp\{-0.0015R_T\}$	$\exp\{-1.75/(1+R_T/50)\}$	$1-0.86\exp\{-(R_T/600)^2\}$
f_1	1.0	1.0	$1-0.04\exp\{-(R_T/50)^2\}+(\lambda/2y)^2$
f_2	$1-0.3\exp\{-R_T^2\}$	$1-0.3\exp\{-R_T^2\}$	$1-0.3\exp\{-(R_T/50)^2\}-0.08(\lambda/y)^2$
D	$-2\nu k/y^2$	$-(\nu/y)\partial_y k$	$-2\nu(\partial_y\sqrt{k})^2$
E	$-2\nu(\partial_y\sqrt{\epsilon})^2$	0.0	$-C_2 f_2(\epsilon D/k)^2$

Table 2. Turbulence Models, cont. p.2

Model:	Reynolds	Chien	Lam-Bremhorst
k_w, ϵ_w B.C.	$k_w=0,\ \epsilon_w=\nu\partial_{yy}k$	$k_w = \epsilon_w = 0$	$k_w=0,\ \epsilon_w=\nu\partial_{yy}k$
C_μ	0.084	0.09	0.09
C_1	1.0	1.35	1.44
C_2	1.83	1.80	1.92
σ_k	1.69	1.0	1.0
σ_ϵ	1.3	1.3	1.3
f_μ	$1-\exp\{-0.0198R_y\}$	$1-\exp\{-0.0115y^+\}$	$[1-\exp\{-0.0165R_y\}]^2(1+20.5/R_T)$
f_1	1.0	1.0	$1+(0.05/f_\mu)^3$
f_2	$f_\mu[1-0.3\exp\{-R_T^2/9\}]$	$1-0.22\exp\{-R_T^2/36\}$	$1-\exp\{-R_T^2\}$
D	0.0	$-2\nu k/y^2$	0.0
E	0.0	$-2\nu(\epsilon/y^2)\exp\{-0.5y^+\}$	0.0

Model	Nagano-Hishida	Lai-So-Hwang
k_w, ϵ_w B.C.	$k_w = \epsilon_w = 0$	$k_w = \epsilon_w = 0$
C_μ	0.09	0.09
C_1	1.45	1.35
C_2	1.90	1.80
σ_k	1.0	1.0
σ_ϵ	1.3	1.3
f_μ	$[1-\exp\{-y^+/26.5\}]^2$	$1-\exp\{-0.0113y^+(1-4.372p^+)\}$
f_1	1.0	1.0
f_2	$1-0.3\exp\{-R_T^2\}$	$1-(2/9)\exp\{-R_T^2/36\}$
D	$-2\nu(\partial_y\sqrt{k})^2$	$-2\nu k/y^2$
E	$\nu\nu_t(1-f_\mu)(\partial_{yy}U)^2$	$-2\nu(\epsilon/y^2)\exp\{-0.5y^+\}$

where

$$P_r = \nu_t[(u_y + v_x)^2 + 2(u_x^2 + v_y^2)], \text{ in 2 dimensions.}$$

$$\nu_k = \nu + \nu_t/\sigma_k$$

$$\nu_\epsilon = \nu + \nu_t/\sigma_\epsilon$$

$$\nu_t = C_\mu f_\mu k^2/\epsilon$$

D, E, f_1, f_2 and f_μ are near-wall or low Re damping terms. C_μ, σ_k, σ_ϵ, C_1, and C_2 are turbulence modeling constants.

There are basically two ways of achieving near-wall damping among the turbulence models reviewed in Ref. 14. One group of models utilizes the D and E terms for near-wall damping (e.g. the Lauder-Sharma and Chien models). Others employ f_1 and f_2 terms in Eq. 2 to achieve the same effect (e.g. the Reynolds and Lam-Bremhorst (LB) models). The Chien and Lam-Bremhorst turbulence models were chosen for further study to represent the two different methods of near-wall damping.

The source terms and near-wall damping terms of the Chien and LB turbulence models were coded in subroutine VIST of INSUP2D. A new subroutine called STEPKE was created to assemble the matrix coefficients of the turbulence equations. In STEPKE, the right-hand-side terms of Eq. 1 and 2 are first computed. The convection terms were discretized with a first-order upwind approximation. A second-order central scheme was employed for all diffusion terms. Finally, the free-stream and solid-wall boundary conditions for a flat-plate boundary layer flow and a circular cylinder wake flow problem were coded. To solve the 2 x 2 matrix equations, two options, were provided: the original LU line-relaxation method and a pointwise over-relaxation matrix

method.

To determine if the numerical formulation and coding were correct, a flat plate turbulent boundary layer was analyzed. A measured turbulent boundary layer profile (Ref. 9) was imposed at the upstream boundary. The computational domain extends 4 initial boundary layer thicknesses in the cross-stream direction and 40 boundary layer thicknesses in the streamwise direction. Results using both the Chien and Lam-Bremhorst models shown in Figs. 11 and 12 indicate similar boundary layer development. With a grid size of 50 x 120 both models gave converged steady-state solutions in 1000 time steps. These results also show 2.31 times increase in CPU time when the turbulence models are activated. As indicated by the results of these studies, the incorporation of low-Re models into INSUP2D code was successful.

In order to compute boundary layer type flow problems, the INSUP2D code was rearranged to provide the correct geometric configuration. The conditions for boundary layer type flows are activated by setting the periodic boundary condition flag to false in the input data file. For the flat plate mesh system, more grid points were clustered near the solid wall, which is located at j = 1, to provide enough grid points (around 10 points) inside the viscous sublayer (y^+,10). A subroutine for generating the initial turbulent boundary layer profiles (at k=kmax) was also created. It was found that the low-Reynolds number turbulence models were very sensitive to the inlet turbulent boundary conditions since the wall damping terms are very sensitive functions of the turbulence quantities. As a result, the profiles of the inlet turbulence quantities (especially the non-measurable turbulent energy dissipation rate, ϵ) must be carefully selected or provided by experimental data.

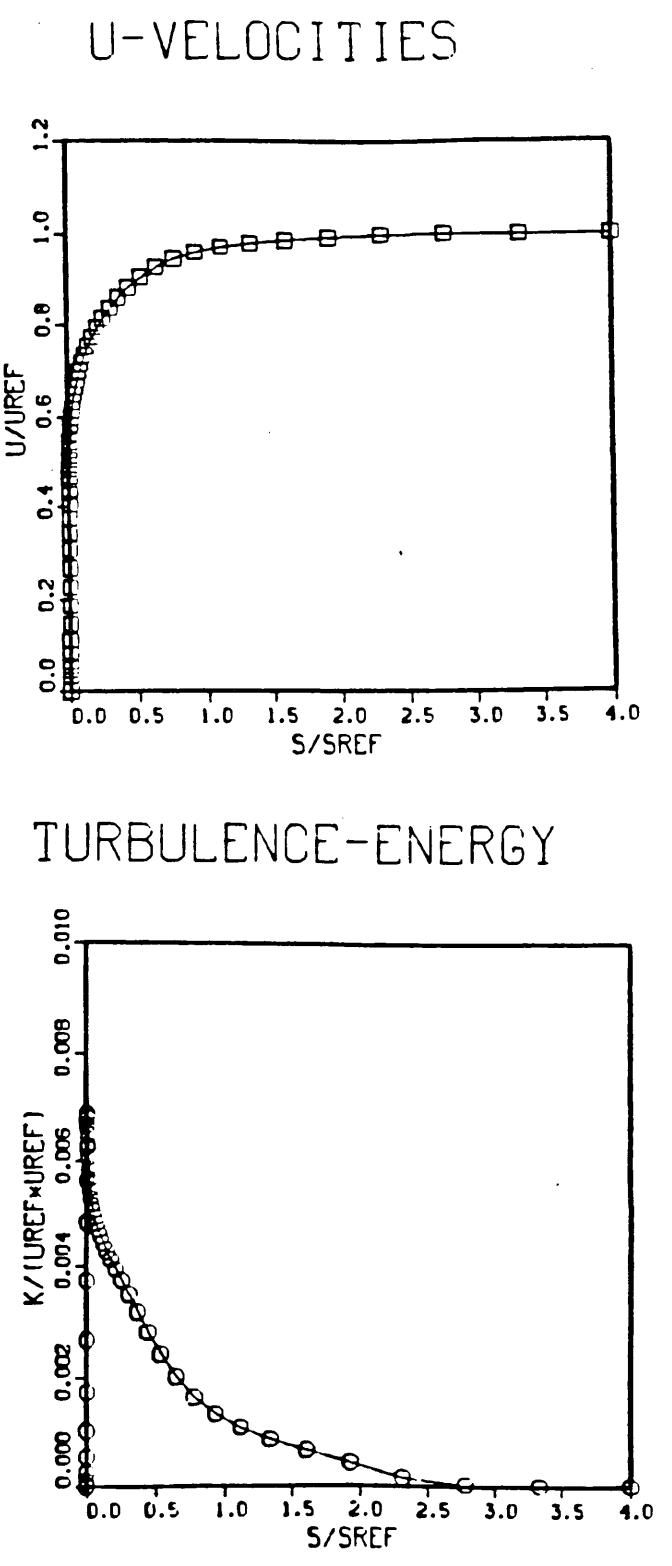

Figure 11. Boundary Layer Flow with the Chien Low-Re $\kappa\epsilon$ Model at X = 40 δ_o.

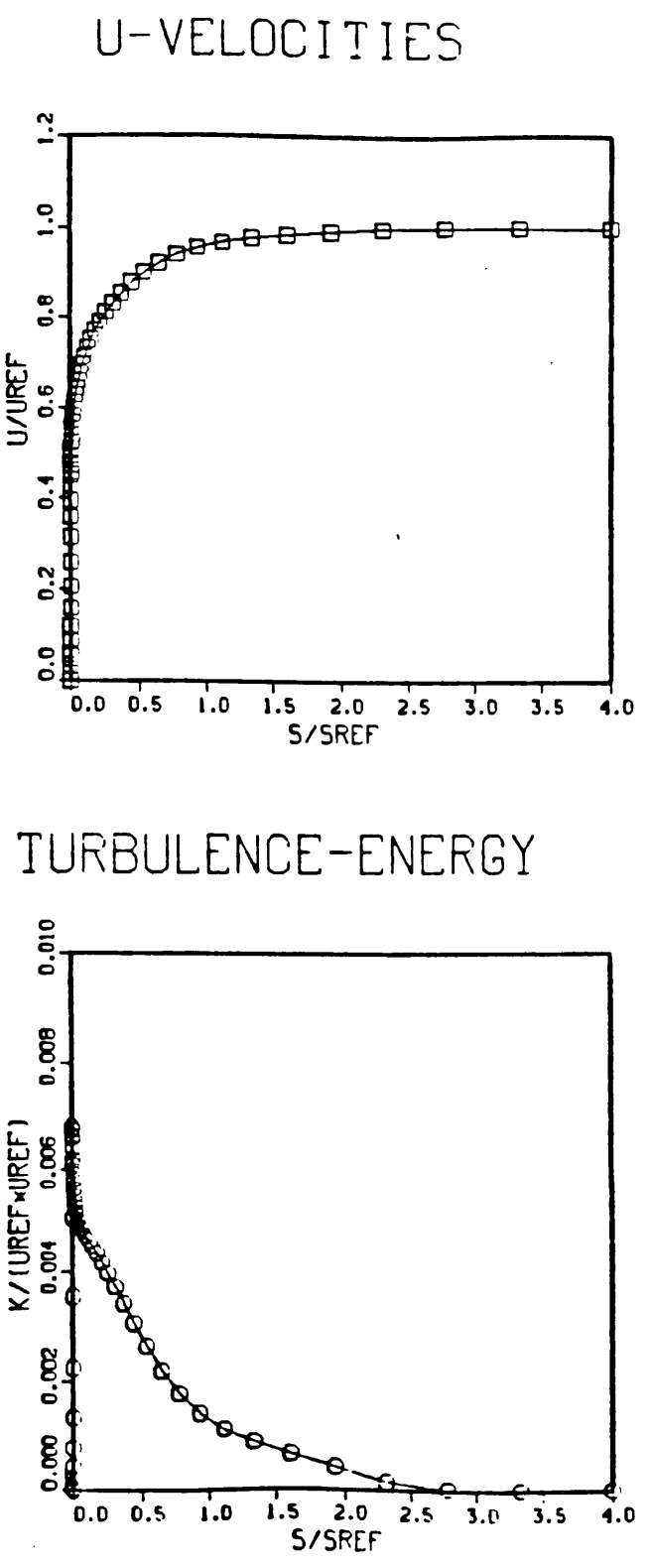

Figure 12. Boundary Layer Flow with the Lam-Bremhorst $\kappa\epsilon$ Model at X = 40 δ_o.

After the two low-Reynolds number turbulence models were added to the INSUP2D code and the turbulence models were verified to predict boundary layer flow on a flat plate at Re = 10E6, flow about a cylinder was analyzed. A solution for pressure contours and streamlines is shown in Fig. 13. Predicted turbulent kinetic energy is shown in Fig. 14. The free-stream was specified to have 1% TKE; the wake flow was found to have more than 30%. This value is not realistic, which means that this turbulence model requires additional tuning. Because this computation was very slow in terms of machine time used, developing a three-dimensional solution for the LOX tee manifold starting with INSUP2D is not recommended and was not further developed.

SECA's FDNS code has been used to simulate flow about a cylinder at Re = 40 and 200, Refs. 16 and 17, respectively. The results of these predictions are of comparable accuracy to those just presented for the INSUP2D study, but the calculation was made in less than 1/10 the time. Therefore, FDNS was selected for further development to investigate wake flow behind vanes and 3-dimensional LOX tee flow.

BLADE WAKE STUDIES

To expedite the study of vane wakes required for investigating the 4000 Hz problem, detailed two-dimensional analyses of flows around blades typical of those in the LOX tee were made. However, the time accuracy of such solutions was first validated by investigating two vane geometries for which experimental data were available. These validation cases were studied to determine if the effects of implicit damping in the algorithms and/or in the turbulence model overdamped the formation of vorticies in the wake of the blades. If the numerical flow solvers correctly predicted the vortex shedding

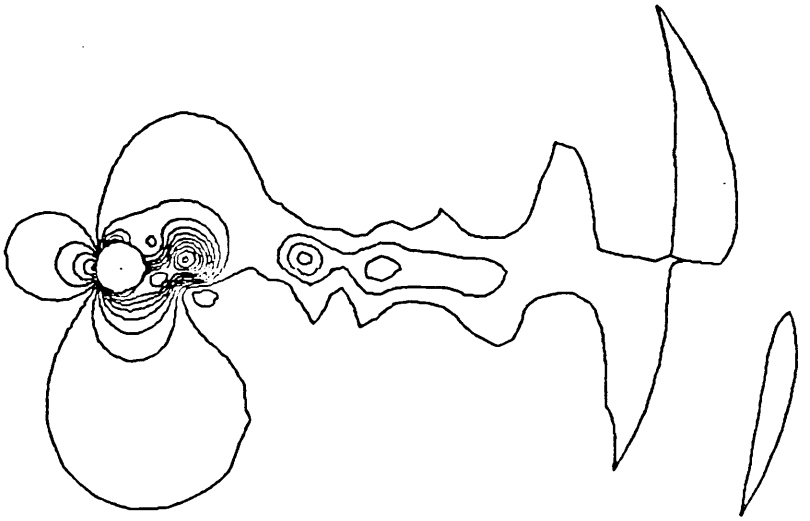

Pressure Contours

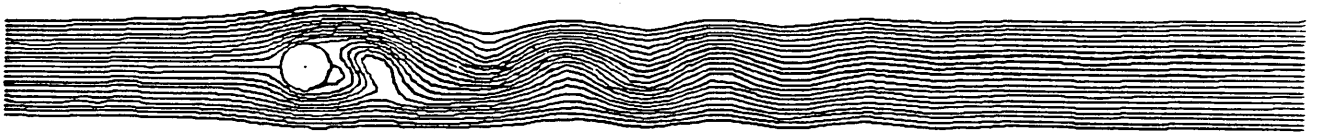

Streamlines

Figure 13. Turbulent Flow for a Cylinder in Cross-Flow with Chien's Low-Re Turbulence Model.

Figure 14. Turbulent Kinetic Energy Profiles for a Cylinder in Cross-Flow with Chien's Low-Re Turbulent Model.

frequency for these cases, more complex conditions could then be considered.

- Vane Validation Studies

Predictions of vortex shedding characteristics of rounded and sharp trailing edge blades were made. A second-order time-centered finite difference Navier-Stokes flow solver (FDNS2D) was used in this study. The flowfields around blade configurations which were experimentally investigated by A. Haji-Haidari and C. R. Smith (Ref. 18), were simulated. In these experiments, the water flows, upstream of the trailing edge, are turbulent with a Reynolds number of 32,000 (based on blade thickness and an average velocity). Mean velocity and turbulent intensity profiles inside the wake were measured using hot film anemometry. Flow visualization and recording techniques utilized a hydrogen bubble generator and a high-speed video system to determine the vortex shedding frequencies.

Two cases with flow Reynolds numbers of 1,000 and 32,000 were numerically simulated for each blade in the present study. For the low Reynolds number cases, the flow was assumed to be laminar. For the high Reynolds number cases, an extended two-equation turbulence model with wall function boundary conditions was employed for transient turbulent flow computations. A grid size of 101 x 73 was used. All of the 2-dimensional vane calculations were started from a computational plane normal to and cutting through the vane. This procedure greatly reduced the number of grid points required for a simulation. The experiments were performed in a duct such that bounding walls inclosed the vane tested. These walls were used with slip boundary conditions to bound the computation domain. In order to provide good temporal resolution, a dimensionless time step size of 0.025 (based on blade thickness and mean velocity) was used for each

case. Time-accurate periodic solutions were obtained in 5000 time steps for the Re = 1000 laminar flow past the round trailing edge blade starting from an initially uniform flow field. Fig. 15 (a)-(c) illustrates the solutions of velocity fields, pressure contours and stream function contours, respectively, at the end of 5000 time steps. An additional 3000 time steps were used to obtain a periodic turbulent flow solution starting from the laminar flow solution. Fig. 16 (a)-(c) shows the flowfield solutions for the turbulent flow case. Results of these two cases are quite similar in terms of the vortex shedding patterns except that the strength of the vortices are stronger for the laminar flow case. Both cases produce Strouhal numbers around 0.21. The experimental measurements for the turbulent flow case agree with this value, indicating that the present flow solver was time accurate.

For the sharp trailing edge cases, however, no periodic vortex shedding patterns were predicted even at the end of 6000 time steps. Pressure oscillations near the tip of the trailing edge indicated a very high frequency mode. This suggests that much better grid resolution and much smaller time-step size are required in order to accurately predict the vortex shedding at such high frequencies. This high frequency feature for this blade shape was also observed in the experiments (Strouhal number = 2.16 - 6.03). Fig. 17 (a)-(c) shows the present flow field solutions at the end of 6000 time steps.

The test case with the cylindrical trailing edge geometrically resembles the LOX tee vane trailing edge. This test case sheds vortices at about 1 Hz; for LOX manifold flow conditions and assuming the same Strouhal number, the frequency would be about 1100 Hz. Higher Reynolds numbers, three-dimensional flow effects, curvature of the vane, velocity imbalance on either side of the vane, and/or an inadequate

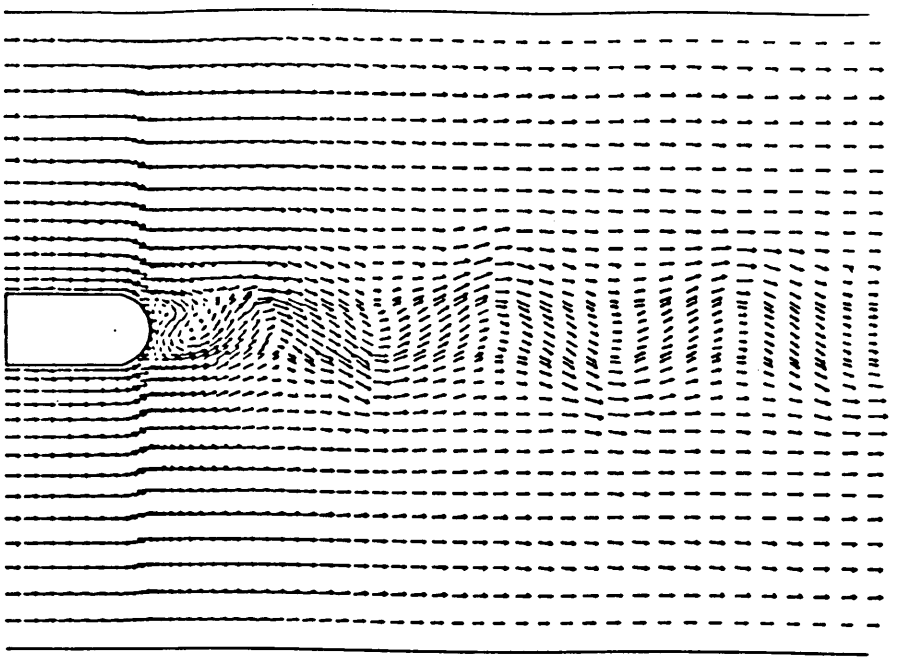

(a) Velocity Vectors.

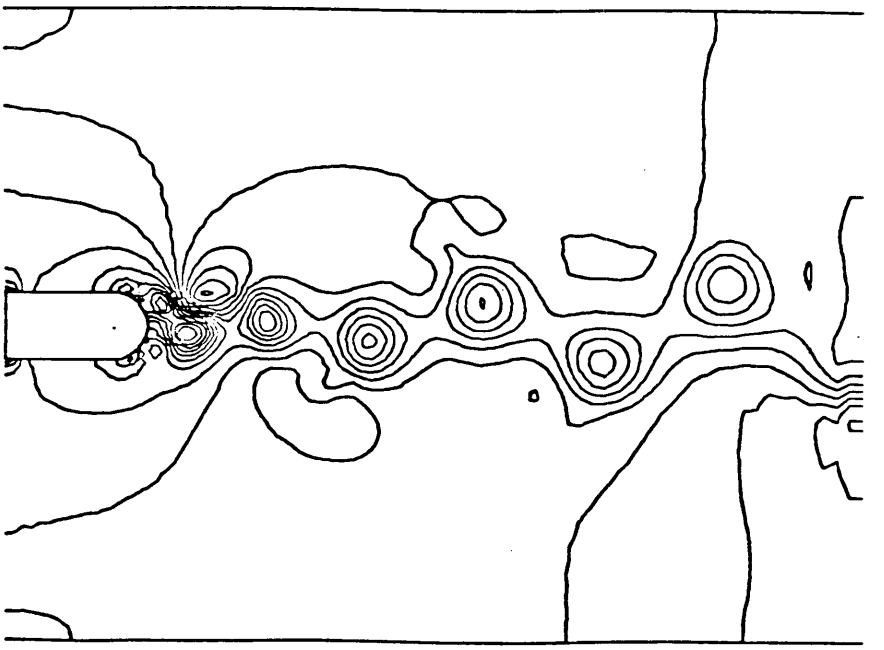

(b) Pressure Profiles.

Figure 15. Laminar Flow over a Vane.

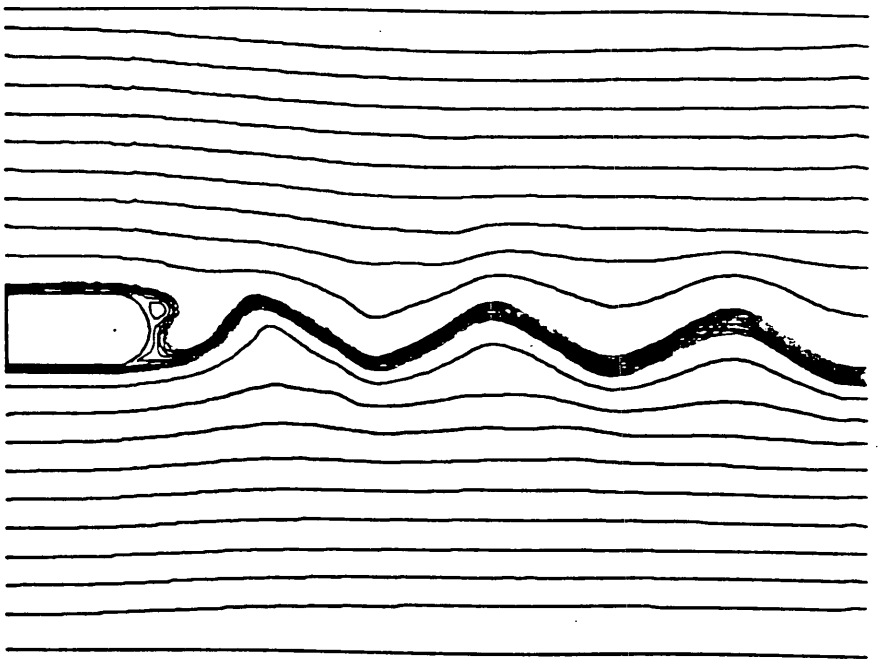

(c) Streamlines.

Figure 15. Laminar Flow over a Vane.

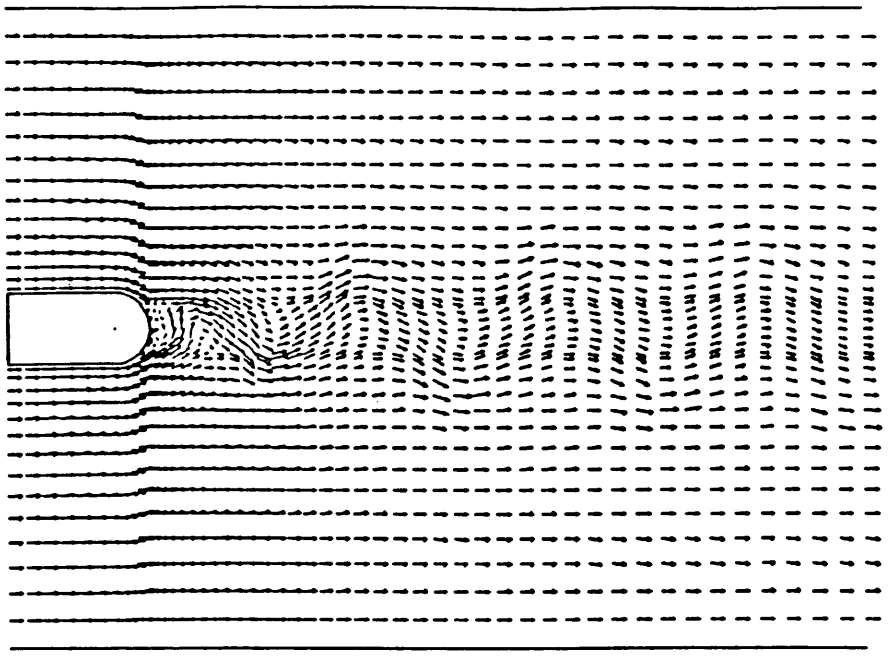

(a) Velocity Vectors.

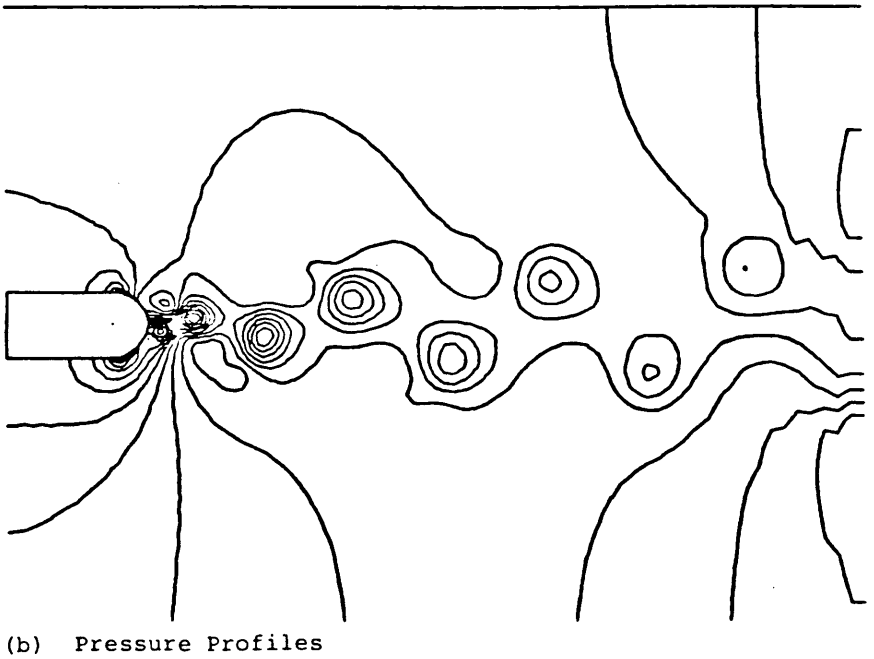

(b) Pressure Profiles

Figure 16. Turbulent Flow over a Vane.

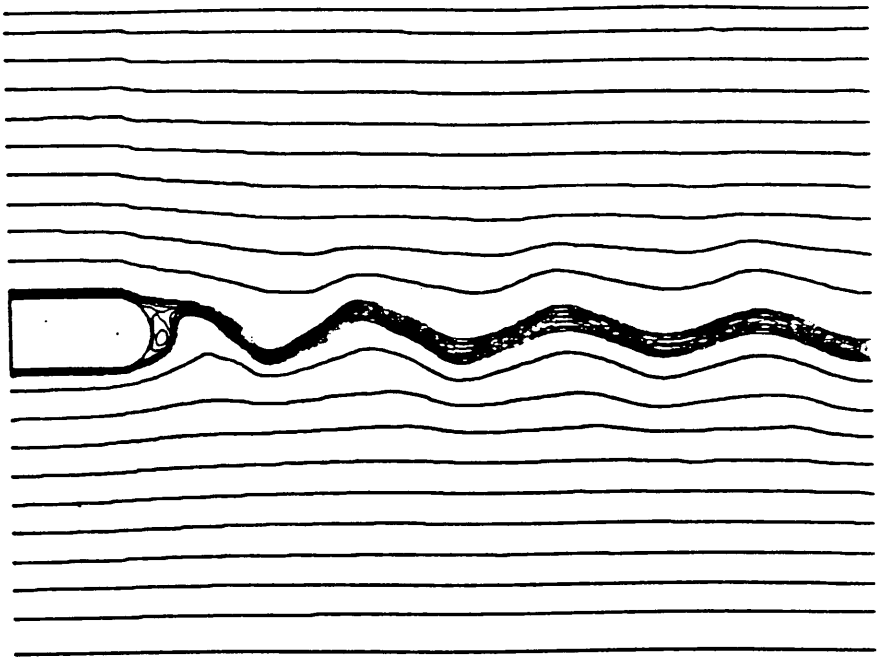

(c) Streamlines.

Figure 16. Turbulent Flow over a Vane.

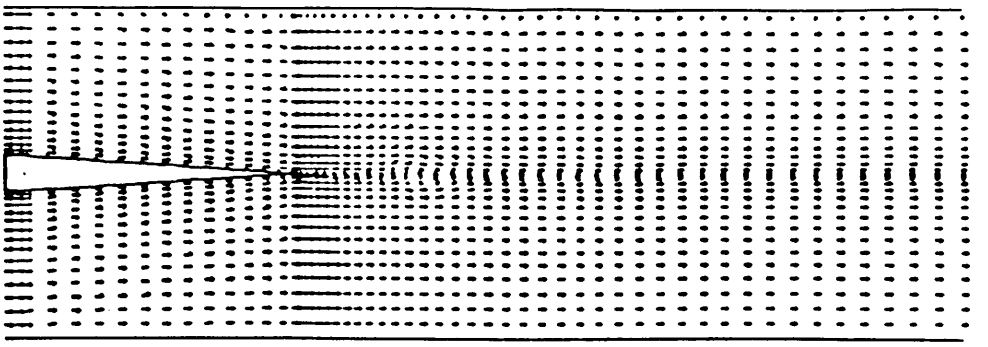

(a) Velocity Vectors

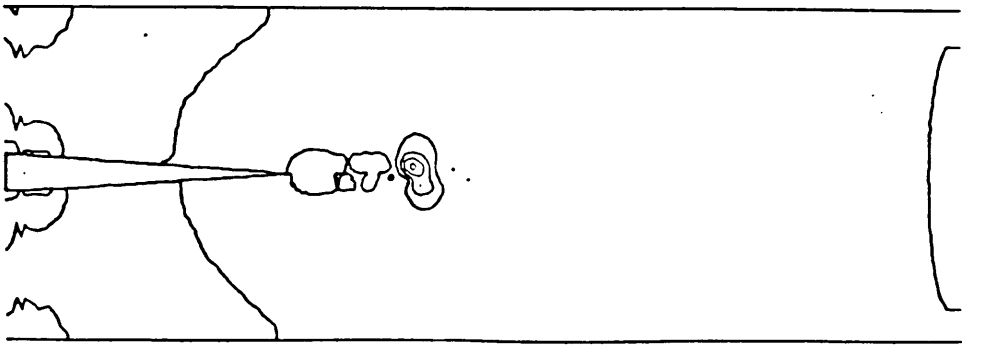

(b) Pressure Profiles

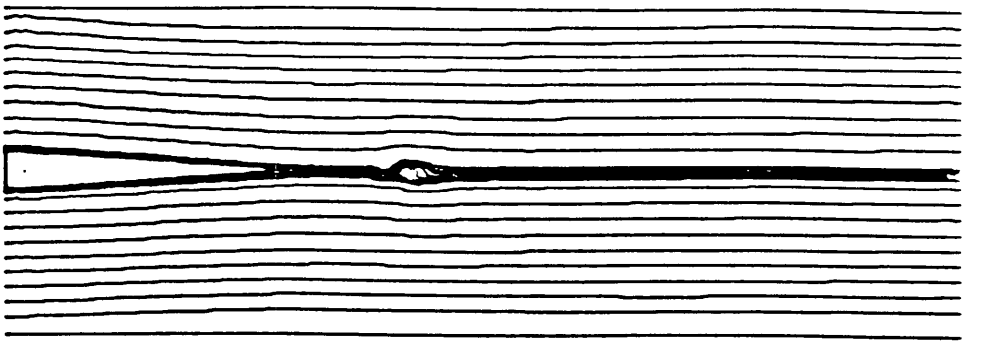

(c) Streamlines.

Figure 17. Turbulent Flow Over a Vane with a Sharp Trailing Edge.

turbulence model might contribute to the indication of too slow an excitation frequency being caused by the flow.

- LOX Vane Parametric Studies

Since the blade wake studies were conducted before results of the 3-dimensional flow calculations were available, several blade configurations with various flow conditions were studied parametrically. These simulations were used to determine if oscillating vorticies which could cause a 4000 Hz excitation could be generated by non-uniform velocity fields and blade curvature.

Two blade configurations were studied at a Reynolds number of 10^6 which is representative of that found in the LOX tee. One blade was straight; the other had the curvature of the blades in the LOX tee. Both of these blades were computed with bounding walls which roughly simulated those in the LOX tee. The FDNS2D code was used for these calculations with a k-ϵ turbulence model. Results for the flat blade case are shown in Fig. 18. The predicted Strouhal number for this case was 0.3. The increased Strouhal number was a result of the higher Reynolds number and of the bounding side walls being closer to the blade than was the case for the experimentally tested blade previously described. Note this result also differs from that experimentally observed for a cylinder for which a Strouhal number does not exist at this Reynolds number. Three reasons are suggested for a possible explanation of this difference: (1) the turbulence model used might not be appropriate, (2) experimentally a time average flow is observed, if an ensemble average were observed the vortex structure might be present for the flow over the sphere, and/or (3) the flow for a blade might be different than that for a cylinder. Regardless of the reason(s) for the discrepancy, the flows predicted with the k-ϵ model are yielding interesting

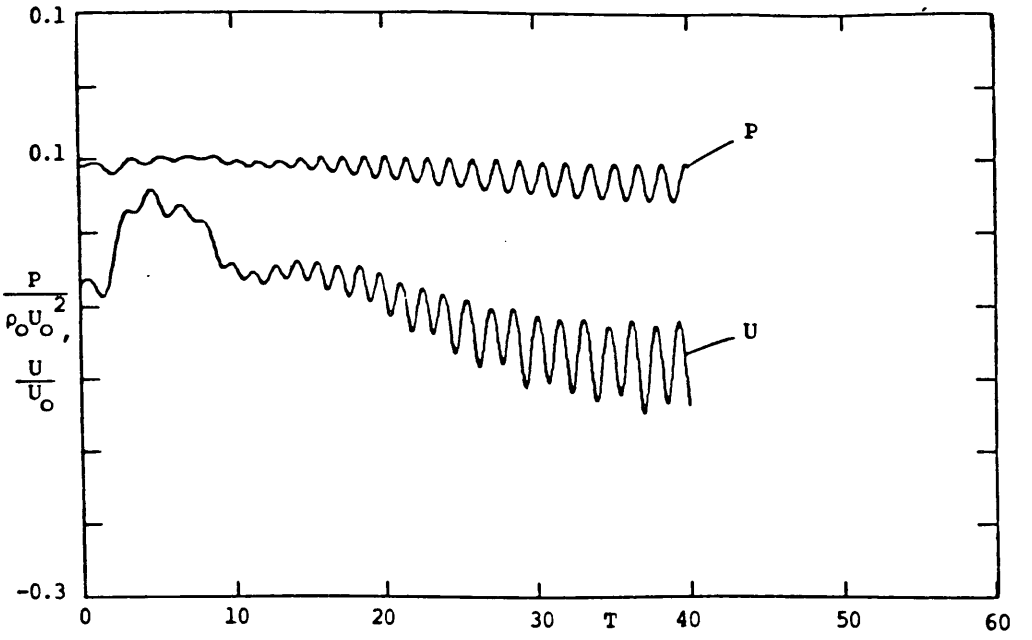

(a) Pressure and Velocity Oscillations.

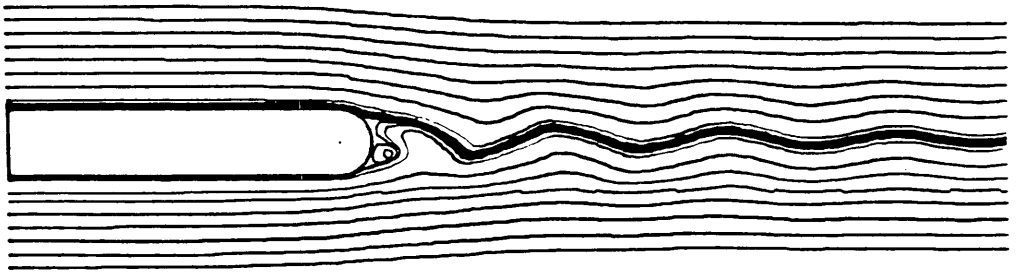

Instantaneous Streamline Locations

(b) Streamlines.

Figure 18. Straight Blade Uniform Inlet Velocity (Re = 10^6, κ-ϵ Model 2000 Time Steps).

results and are as realistic as can be expected without a more extensive turbulence data base. For this blade thickness (0.22 in) and a representative velocity (188 fps), this corresponds to a frequency of 3.07 KHz. Such a frequency is characteristic of the experimentally observed wake structure and the oscillating lift coefficient, C_L. The drag coefficient, C_D; velocity; and pressure (in the near wake) oscillate at twice this frequency. This doubling of frequencies was also observed by Braza, et al (Ref. 8).

The case with the curved blade is shown in Figs. 19 & 20. The frequencies are essentially the same, but the amplitude of the pressure and velocity oscillations essentially double. The drag coefficient curve shown in Fig. 20 does not clearly indicate a doubling of frequency; rather the curve takes a more complex shape. Since the lift and drag coefficients are integrated values over the blade surfaces, the blade tips may tend to oscillate at a higher frequency than the entire blade. In the LOX tee, different velocities are expected on either side of the blade. Even with uniform velocity on either side of the vanes, the pressures and velocities shown in Fig. 18 indicate oscillations of about 3.08 kHz, which leads one to speculate that more realistic flowfield predictions could increase these values to the full 4 KHz in the primary mode without considering harmonics. This strongly suggests that the 4 kHz problem might be directly simulated with a CFD analysis.

Also notice that for the curved blade case both the blade and the bounding walls are curved and parallel to each other, much like the flow in the LOX tee. The experiment and analysis reported by Ref. 19 to analyze blade flow in the SSME LOX tee was for a curved blade in a straight walled duct. Undoubtedly, the duct walls caused the separation which was observed in both the experiment and the simulation. SECA does not believe that such

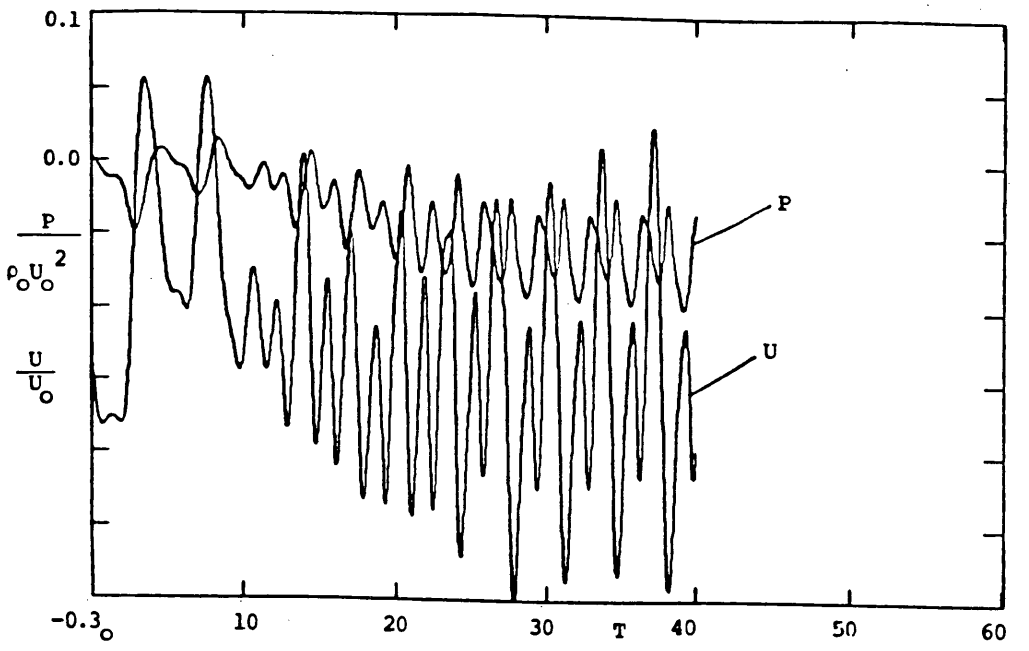

(a) Pressure and Velocity Oscillations.

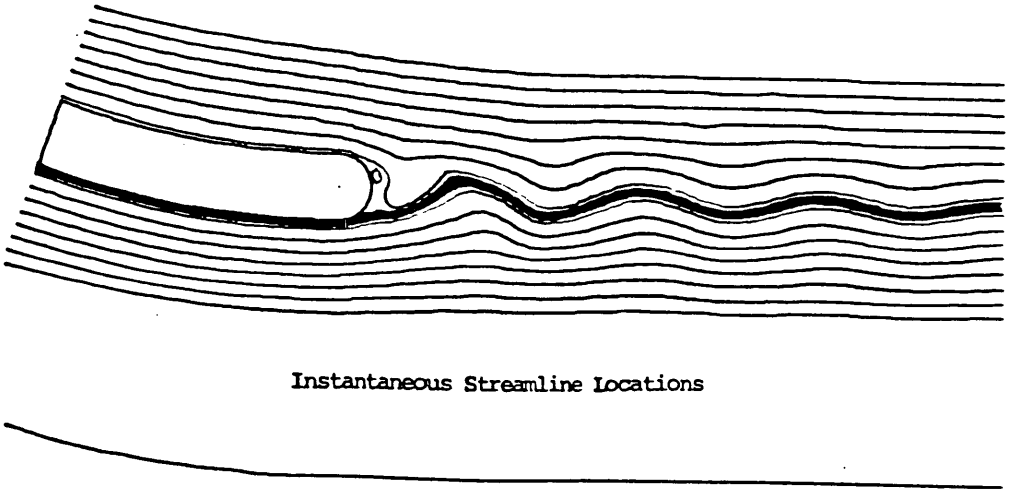

(b) Streamlines.

Figure 19. Curved Blade Uniform Inlet Velocity (Re = 10^6, κ-ϵ Model 2000 Time Steps).

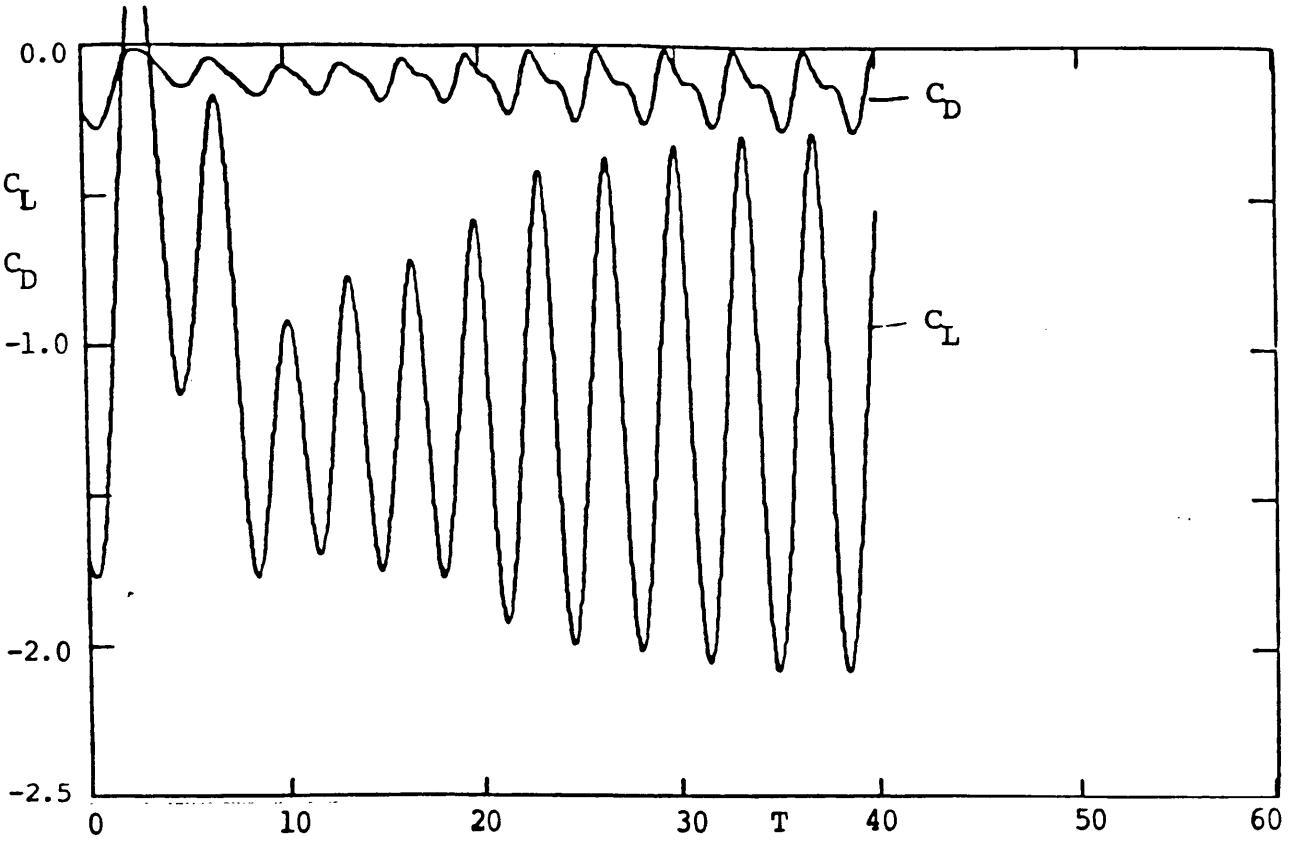

Figure 20. Drag coefficients for the curved blade (Re = 10^6 2000 Time Steps).

flow is representative of that found in the LOX tee.

To make the 2-dimensional simulations more realistic, cases were studied which had different velocities on either side of the vane. Specifically, (1) flow over straight and curved blades with mismatched velocities on either side of the blade and (2) flow over the modified blade configuration of the SSME were simulated.

A flat blade wake case for which the velocities on either side of the blade vary by 20 percent, i.e. 207 fps on one side and 169 fps on the other, was run at a Reynolds number of a million with the FDNS code and a k-ϵ turbulence model. Figure 21 shows the pressure and velocity oscillations and an instantaneous streamline plot. The apparent Strouhal number was 0.27; pressures and velocities oscillated at twice that frequency. The straight blade with uniform velocity at Re = 10E6 produced lift coefficient oscillations of 3078 Hz. The straight blade with velocity mismatch of 20% produced lift coefficient oscillations of 2828 Hz. Complex modes of the oscillation patterns were predicted for this case.

The curved blade flow with a 20% velocity mismatch was run for a Re = 10^6 and the results are shown in Fig. 22. A preliminary run was made at a Re = 10^3 to start the turbulent flow calculation. The flow is quite different from any blade flow that we have previously described. The velocity and pressure oscillations appear to be of the same frequency as the lift and drag coefficient oscillations; the near wake flow does not resemble other flows investigated. The lateral wake oscillations appear quite small in amplitude. The wake oscillations occur at a frequency of about 3913 Hz. Note: This appears to be the source of the 4000 Hz oscillation.

TIME-HISTORY OF SURFACE PRESSURE, CL AND CD:

CASE A-1:

- **LAMINAR:**

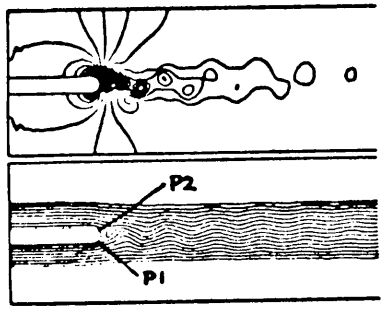

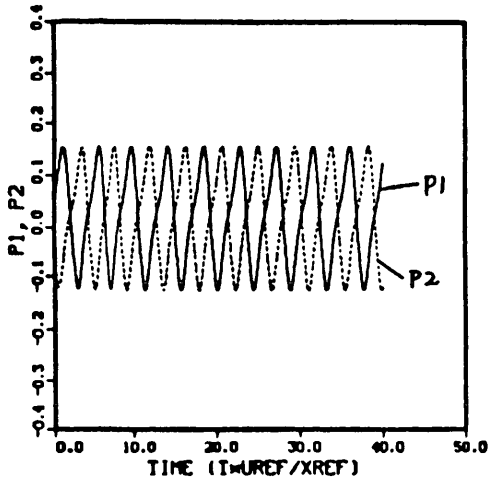

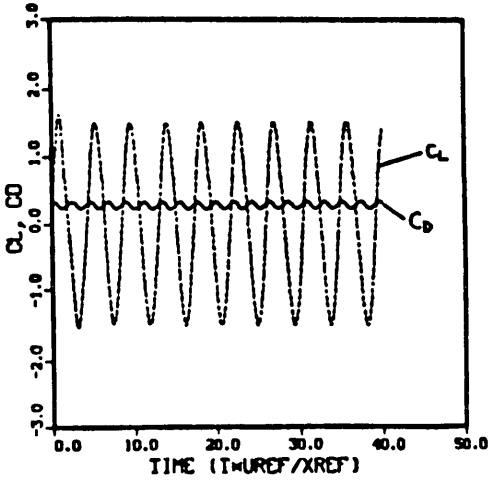

- **TURBULENT:**

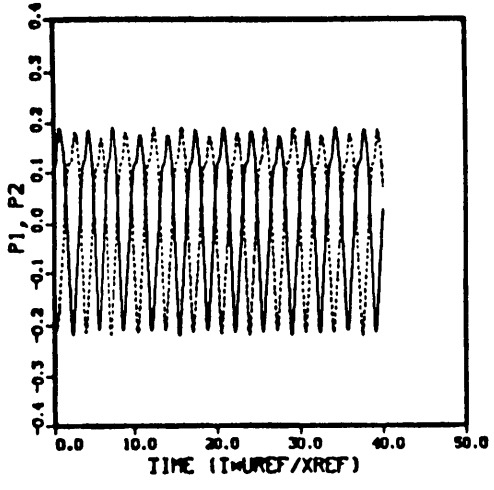

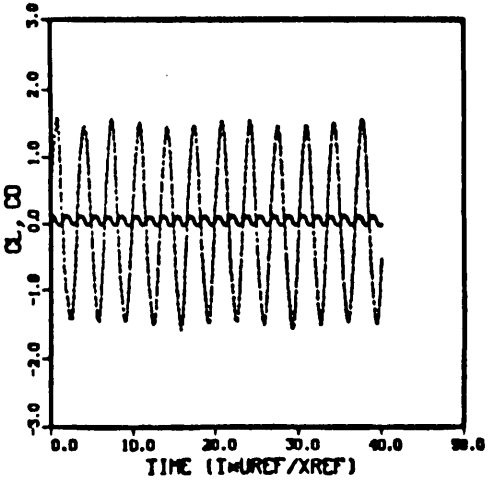

Figure 21. Flow Over a Vane with Mismatched Velocities.

TIME-HISTORY OF SURFACE PRESSURE, CL AND CD:

CASE B-1:

- TURBULENT:

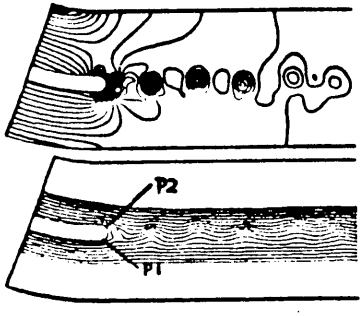

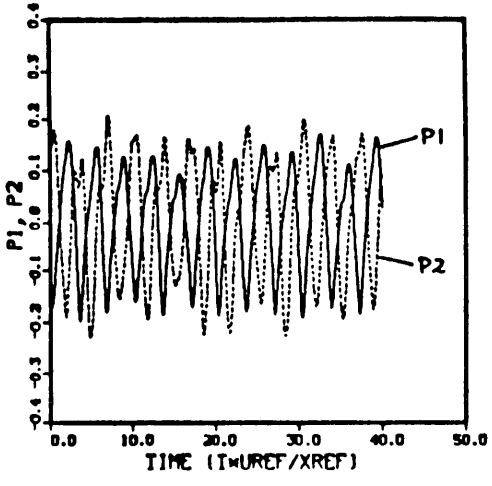

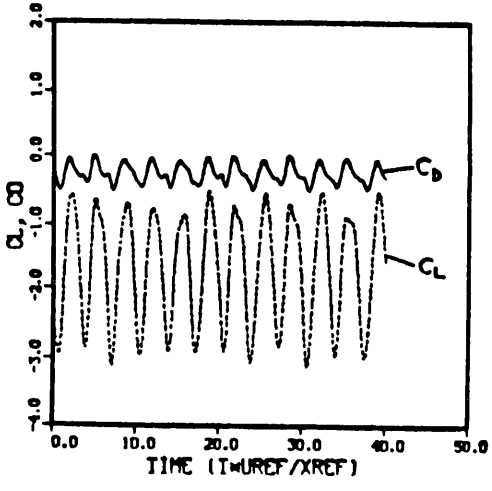

CASE B-2:

- TURBULENT:

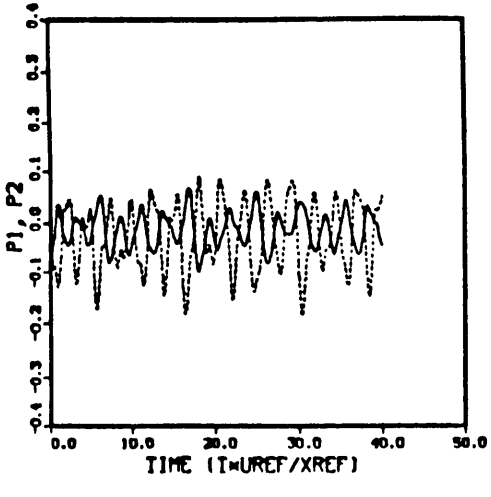

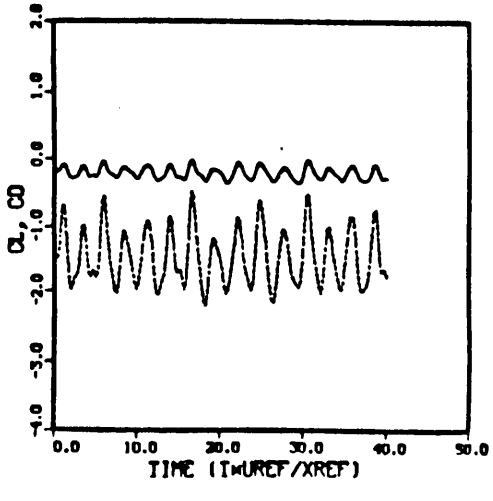

Figure 22. Curved Vane Flow with Mismatched Velocites (Re = 10^6).

The blades in the LOX tee manifold have been modified in order to eliminate the 4000 Hz vibration problem in the SSME. The trailing edges of the blades have been sharpened and the opening between the two blades has been enlarged. The effect of the sharpened trailing edge was studied with a two-dimensional CFD analysis using FDNS2D. The grid shown in Fig. 23 was used for this analysis. Modified vane cases are summarized in Fig. 24. Uniform flow on either side of the blade was simulated. A Re = 10^3 case was run until a periodic solution was obtained, then the Re was increased to 10^6. The periodic solution is shown in Fig. 25 for pressure contours and flow streamlines. Notice the smoothness of the streamlines and the pressure pattern does not indicate vortical flow; the blade shape change is performing as expected. Pressure and velocity were monitored at a point close to the trailing edge, point A, and were found to almost stabilize and then begin to oscillate at a high frequency. Although the C_L and C_D stabilized at about 20 units of dimensionless time, about 60 units of time were required before pressure and velocity became periodic. This behavior is shown in Figs. 26 and 27. Since the amplitude of the C_L and C_D oscillations were small, the pressure and velocity fluctuations were believed to be highly localized. Plots of pressure and velocity at points B, C, and D, located as shown in Fig. 27, are shown in Figs. 28 - 30. These figures indicate that these oscillations do die out very near the trailing edge.

The new trailing edge configuration was further studied by analyzing a velocity mismatch case. Again the turbulent flow solution was started from a periodic average Re = 10^3 solution. The pressure contours and streamlines are shown in Fig. 31 for an average Re = 10^6. Some vortex structure is shown very near the trailing edge for this case. The same temporal behavior of pressure, velocity, C_L, and C_D as was found for the uniform flow case is seen in the predictions shown in Figs. 32 and 33.

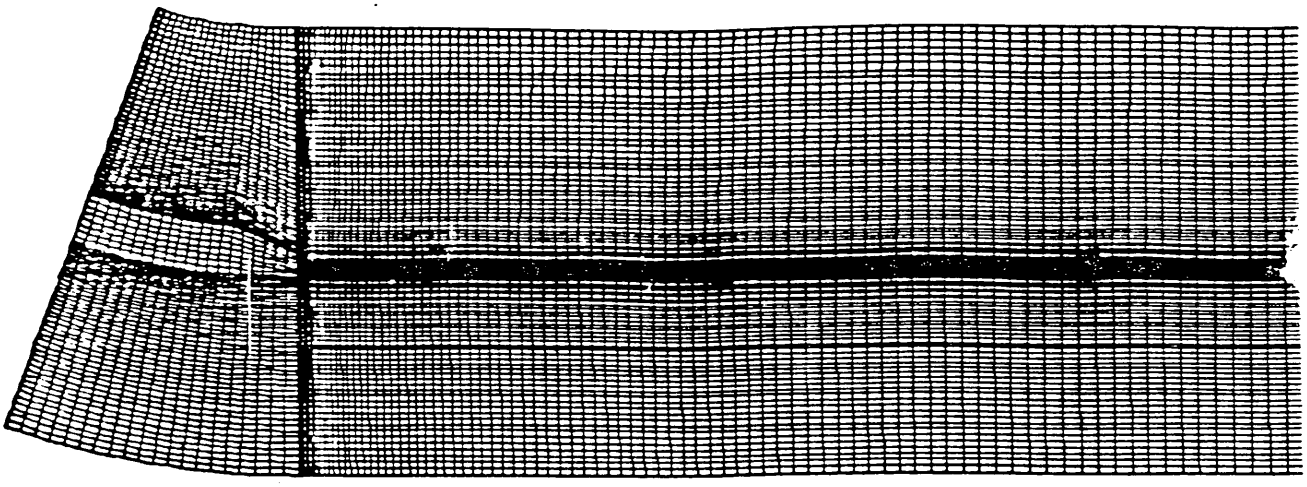

Figure 23. Grid for Modified Blade Shape.

TIME-HISTORY OF SURFACE PRESSURE, CL AND CD:

CASE C-1:

- TURBULENT:

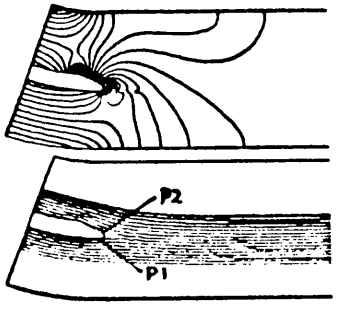

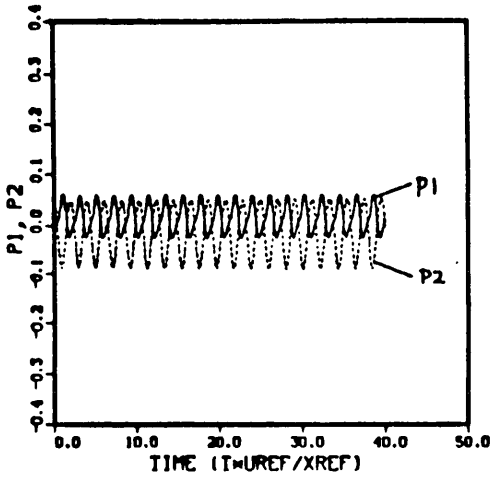

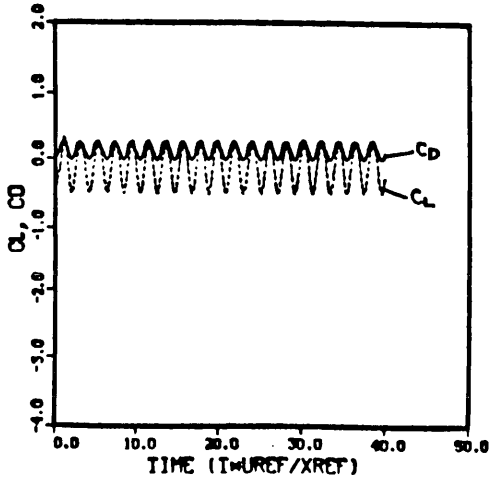

CASE C-2:

- TURBULENT:

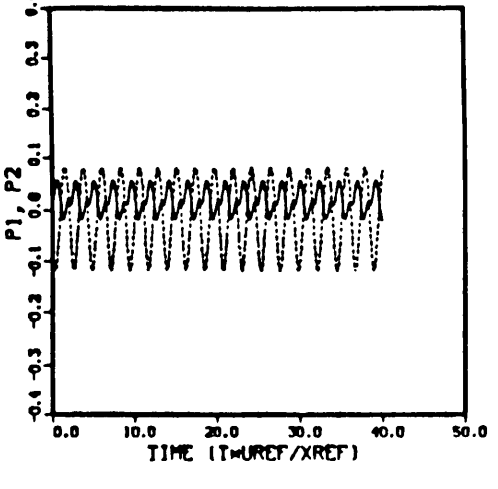

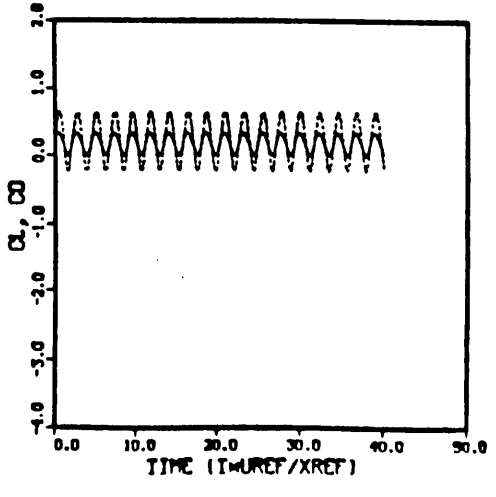

Figure 24. Modified Vane Cases

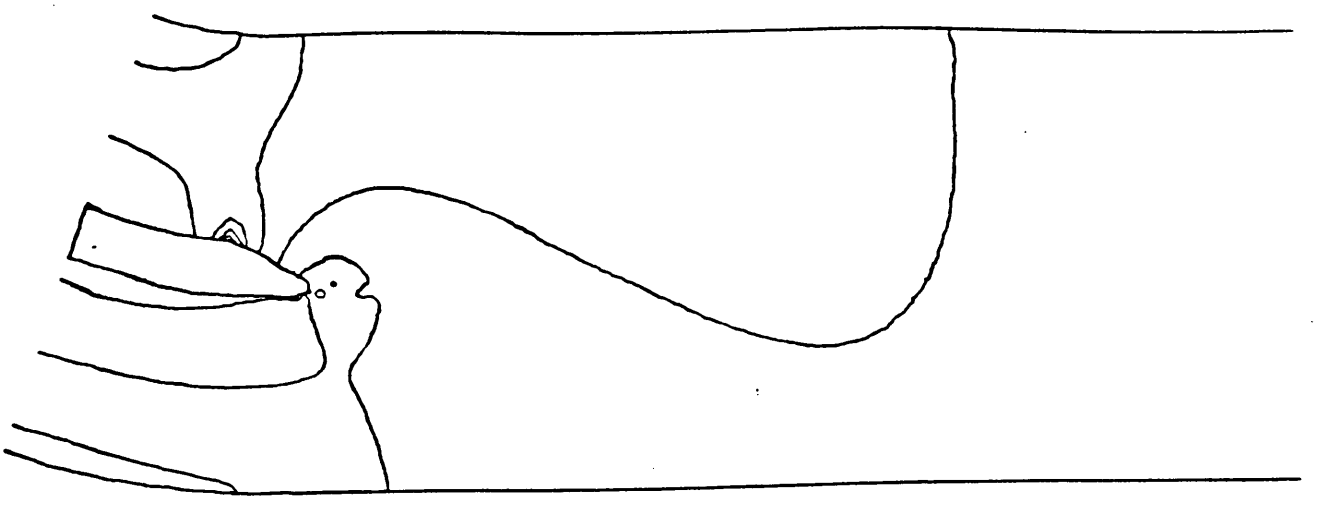

(a) Pressure Contours

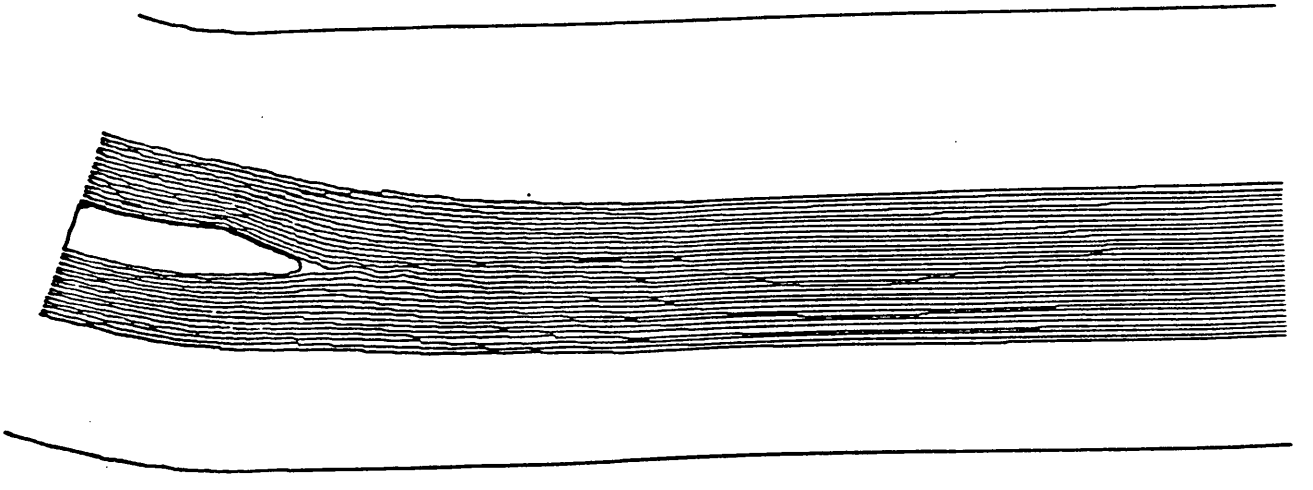

(b) Streamlines

Figure 25. Uniform Turbulent Flow (Re = 10^6)

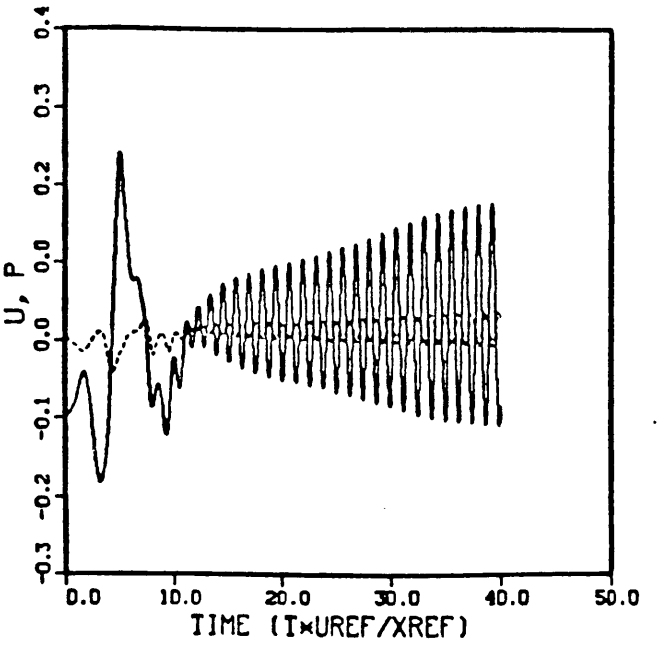

(a) Velocity and Pressure

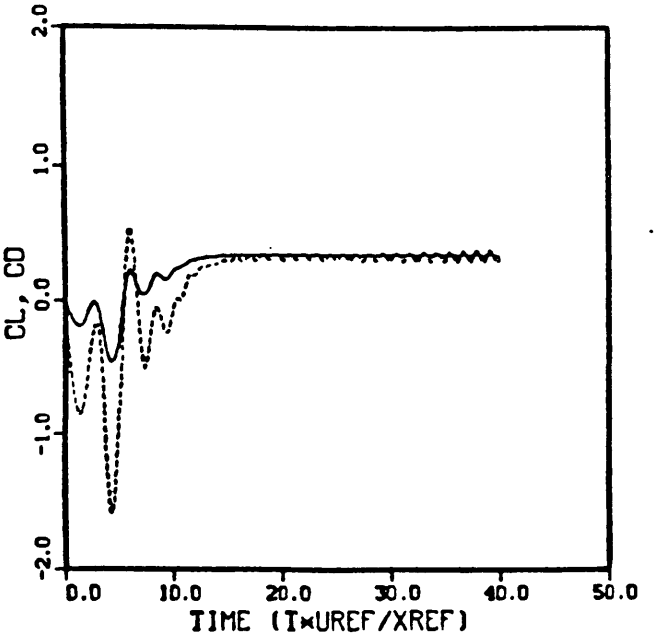

(b) Drag and Lift Coefficients

Figure 26. Solution History at Point A for a Modified Vane ($Re = 10^6$).

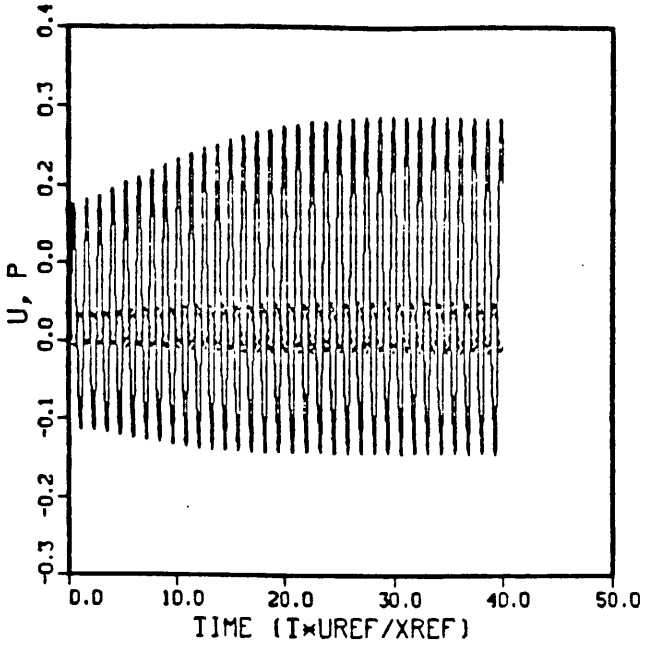

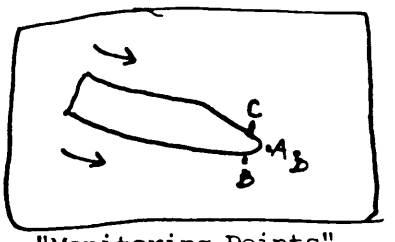

"Monitoring Points"

(a) Velocity and Pressure.

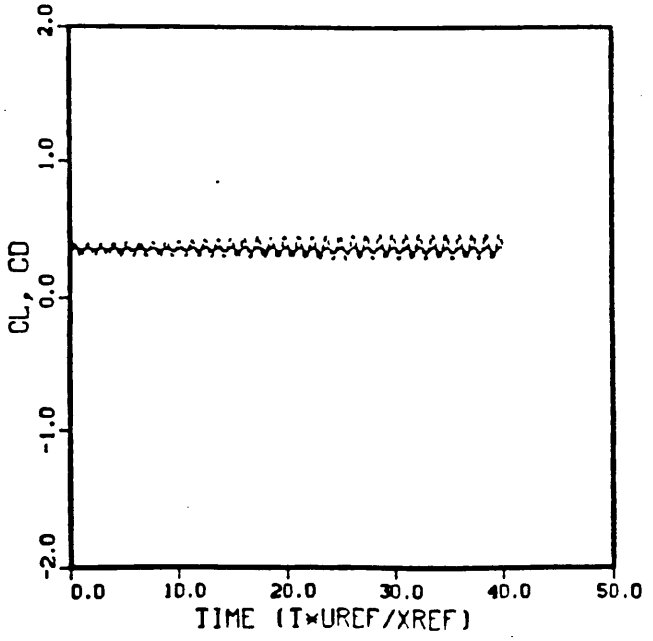

(b) Drag and Lift Coefficients.

Figure 27. Solution History at Point A for a Modified Vane.

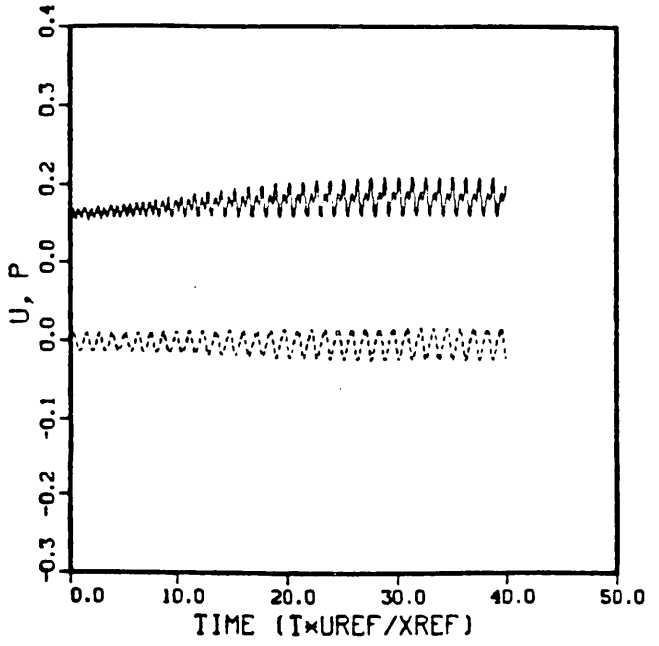

Figure 28. Solution History for a Modified Vane, at Point B.

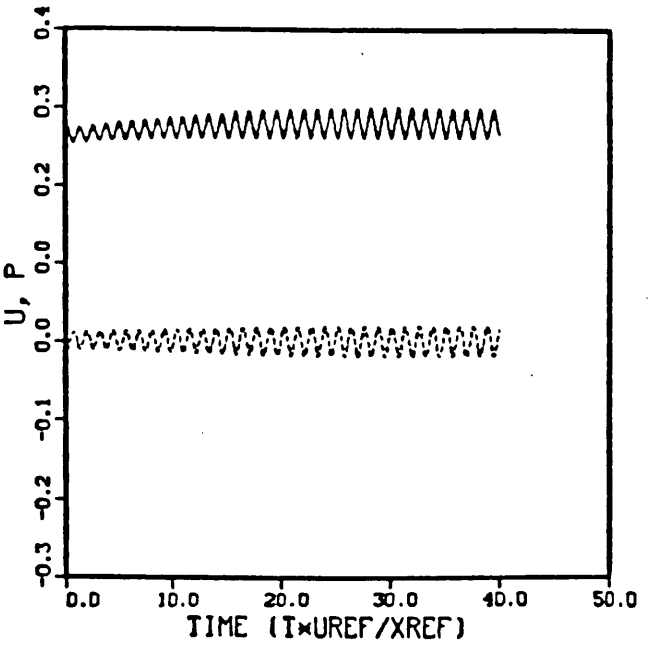

Figure 29. Solution History at Point C for a Modified Vane.

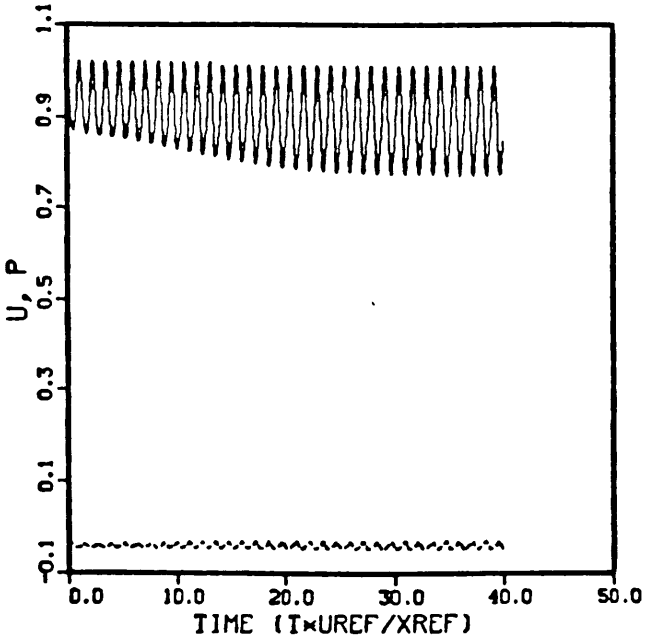

Figure 30. Solution History at Point D for a Modified Vane.

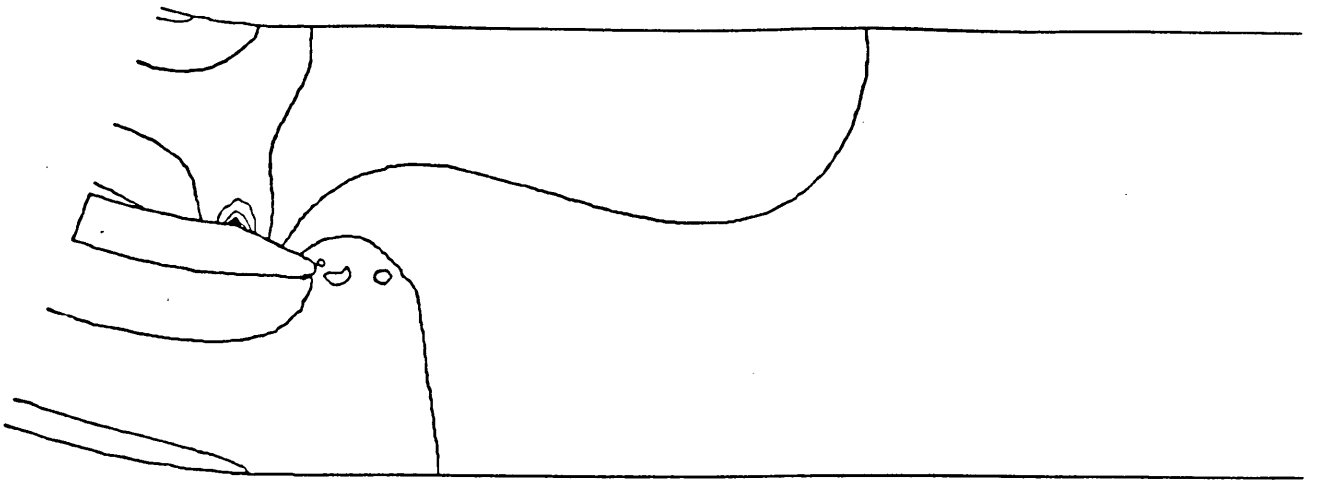

(a) Pressure Contours.

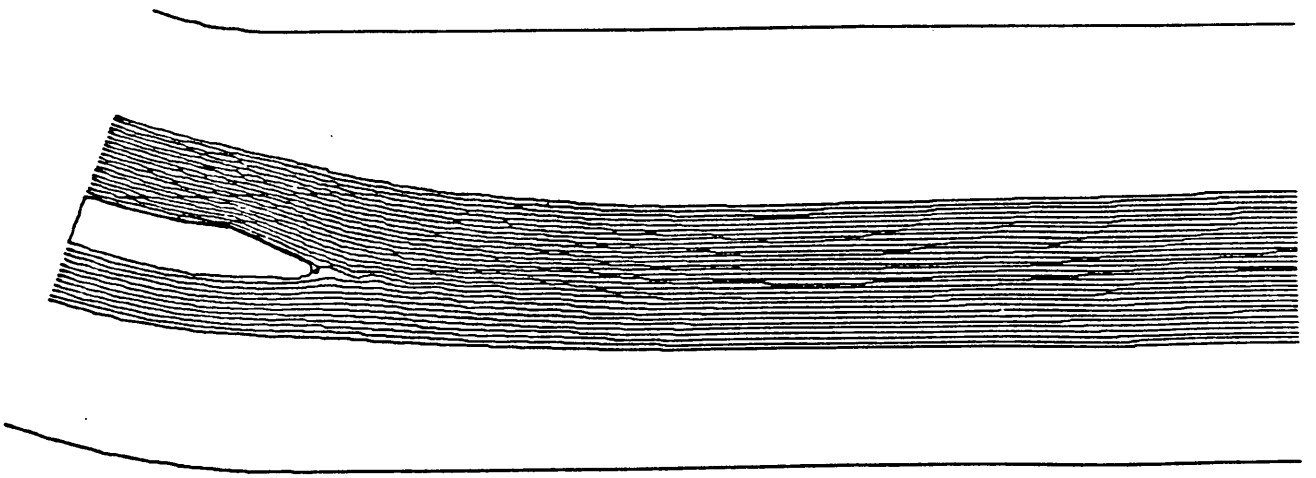

(b) Streamlines.

Figure 31. Non-Uniform Turbulent Flow (Re = 10^6).

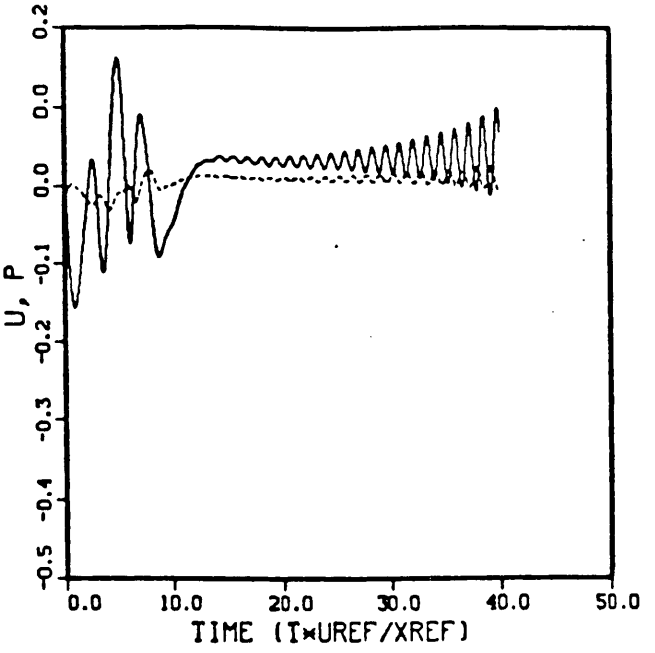

(a) Velocity and Pressure.

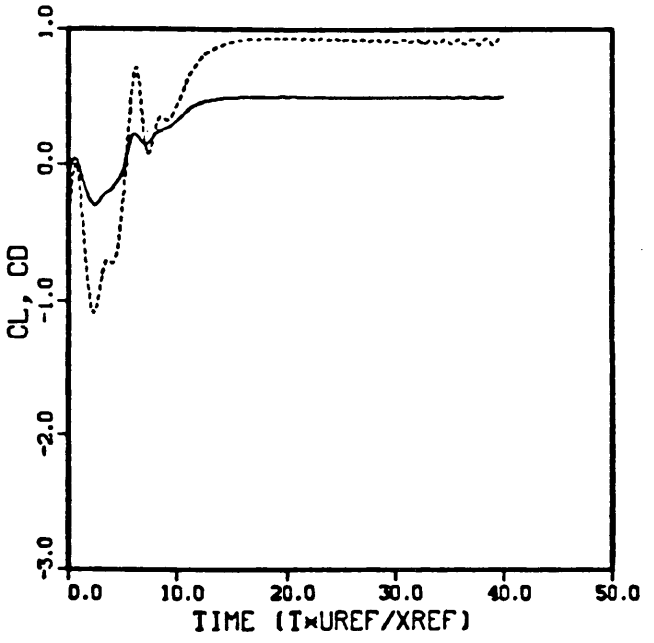

(b) Drag and Lift Coefficients.

Figure 32. Solution History at Point A for Non-Uniform Turbulent Flow.

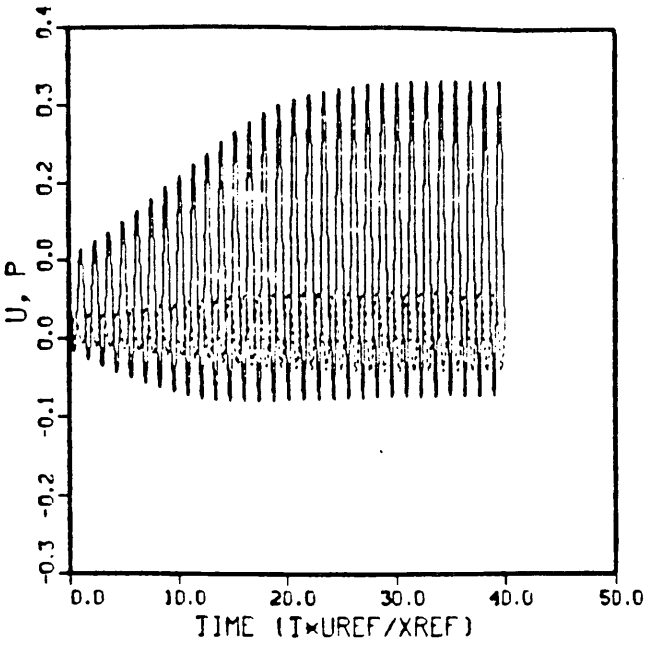

(a) Velocity and Pressure.

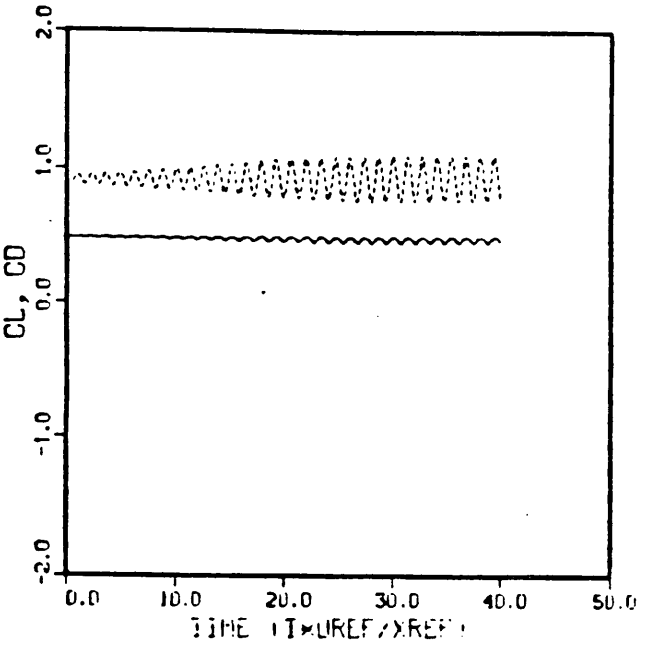

(b) Drag and Lift Coefficients.

Figure 33. Solution History at Point A for Non-Uniform Turbulent Flow.

The results of the new blade analyses compared to those for the old round blade indicate that almost all of the vortical flow in the blade wake should be removed.

The significant 2-dimensional blade wake flow analyses are summarized in Table 3. These predictions indicate that 4000 Hz oscillations could be predicted in the LOX manifold with this computational model. Performing a three-dimensional analysis of the LOX manifold using the FDNS3D code was the next step performed in this study.

LOX TEE MANIFOLD ANALYSIS

- LOX Tee Geometry

The geometry of the LOX tee manifold from the main LOX valve to the slots downstream of the vanes was described with analytical expressions in preparation for creating a 3-D computational grid for analyzing the flow in the manifold. All of the required geometric features were quantitatively established from system drawings and from discussions with MSFC and Rocketdyne personnel. The analytical expressions were incorporated into a computer code to generate the grid for the LOX tee. The code was compiled, executed, and verified on a microcomputer using standard FORTRAN.

Figs. 34 through 39 present various views of the geometry as represented by a bare minimum 5940 nodes. The actual geometry requires between 100,000 and 150,000 nodes. Fig. 34 shows the 90-degree elbow upstream of the tee. Fig. 35 shows the plane of symmetry (Z=0 plane) and illustrates relative postions of the elbow, the "ring" connecting the elbow and the tee, and the tee itself. Fig. 36 shows two views of the tee with the splitter vane. The 0.25 inch radius fillet around the top and bottom of the vane is exaggerated due to the coarse grid. Fig. 37 shows

Table 3. Summary of Blade Wake Studies

CASE	Re = 1,000		Re = 1,000,000	
	C_L (Hz)	Strouhal No.	C_L (Hz)	Strouhal No.
A-1	2348	0.225	3067	0.295
A-2	2348	0.225	2828	0.271
B-1	2765	0.265	3078	0.295
B-2	3078	0.295	3913	0.375
C-1	3235	0.310	5061	0.485
C-2	3287	0.315	4644	0.445

C_L is the frequency of the lift coefficient oscillation.

A - Blunt Straight Vane

B - Blunt Curved Vane

C - Tapered Curved Vane

1 - Equal Velocies

2 - 20% Velocity Difference

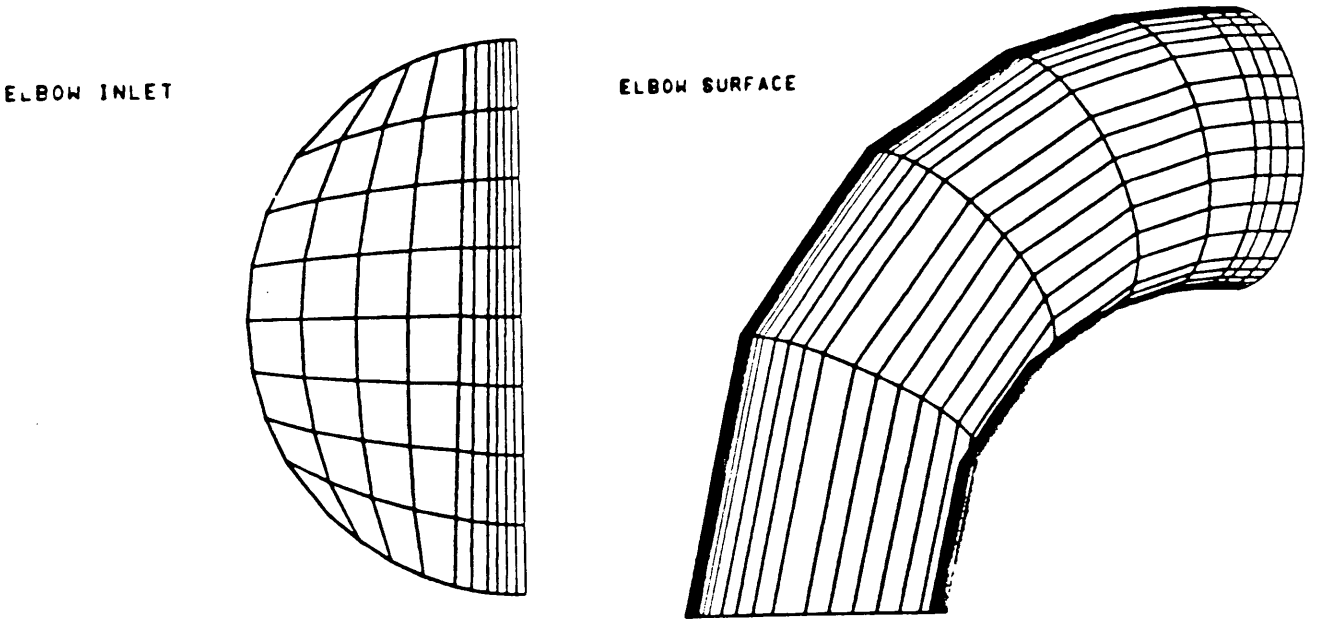

Figure 34. The 90° Elbow

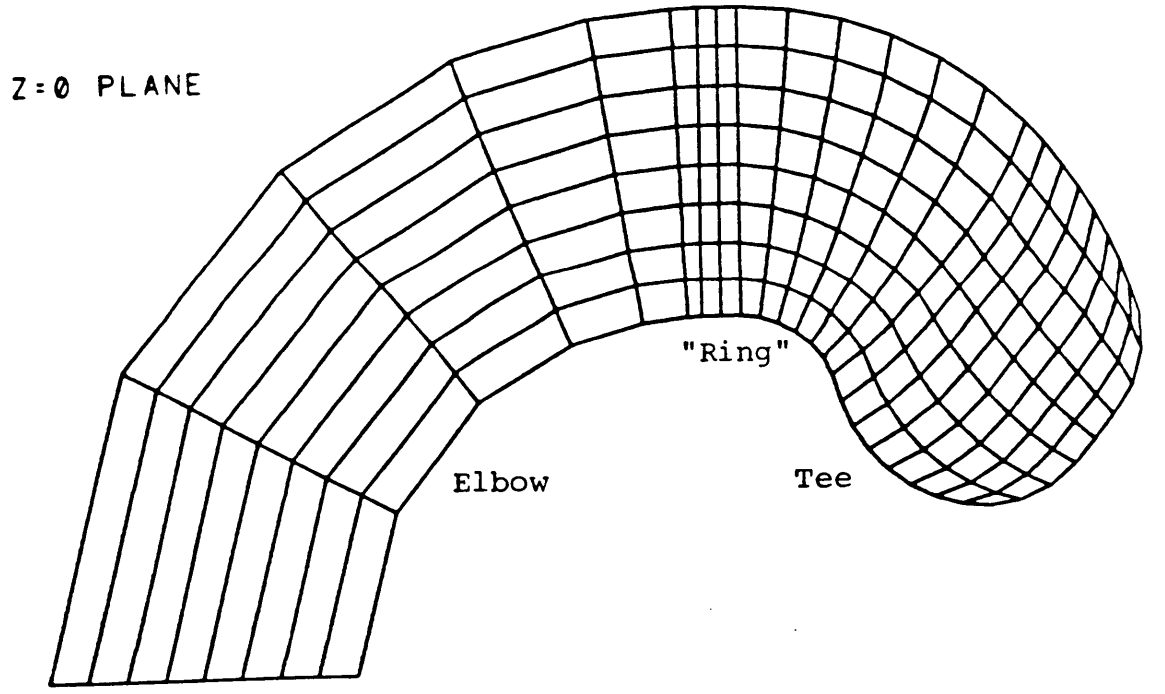

Figure 35. The Plane of Symmetry

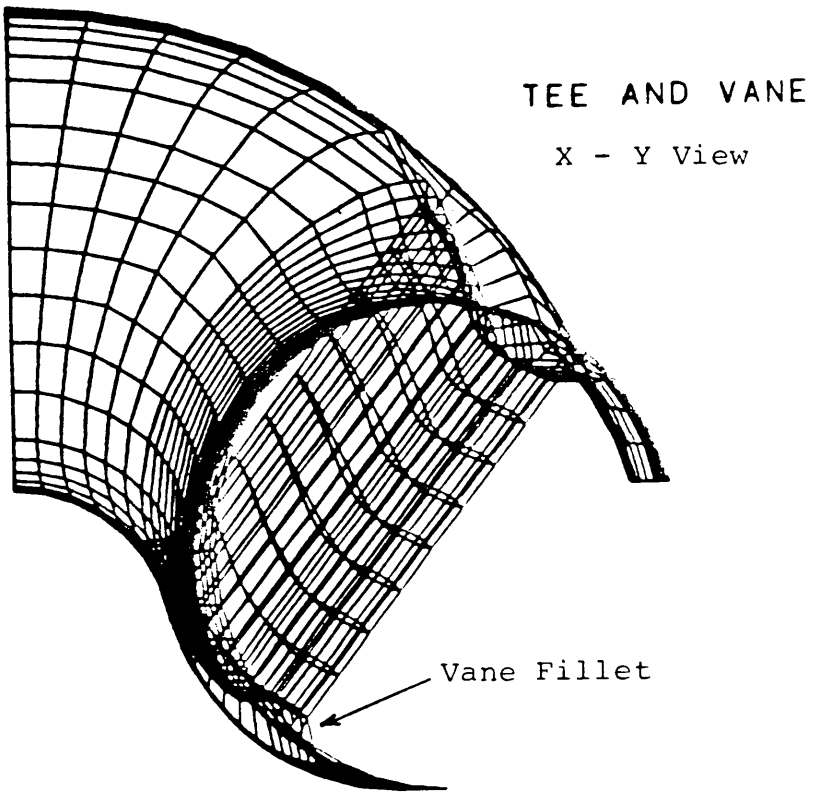

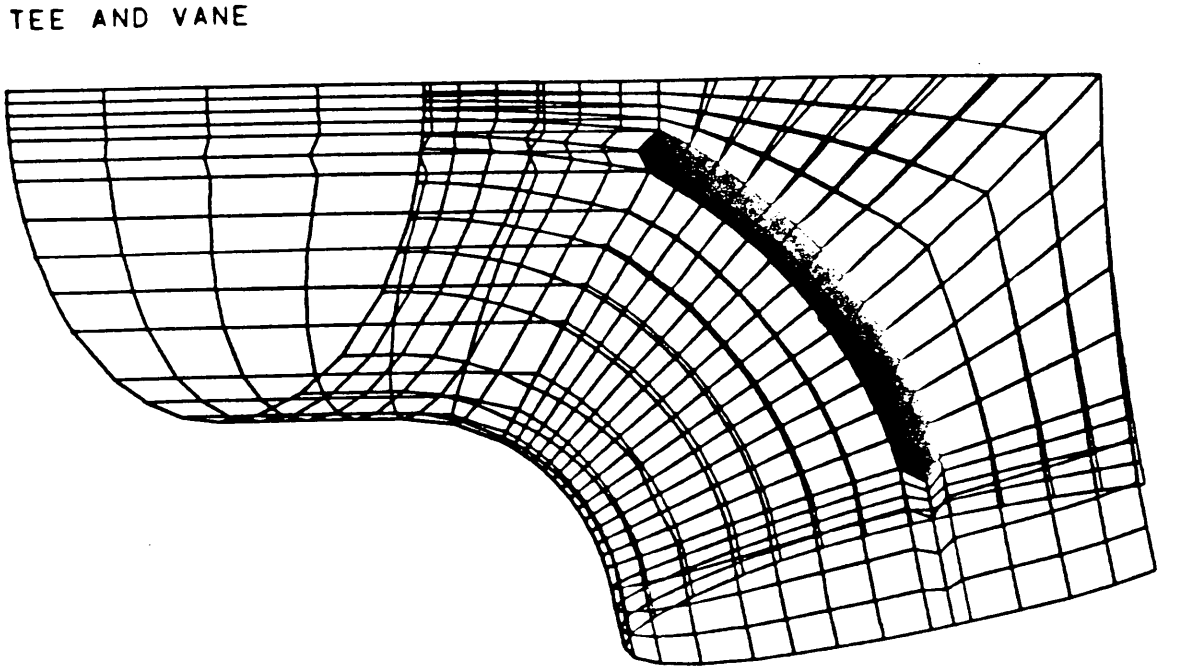

Figure 36. LOX Tee Splitter Vane

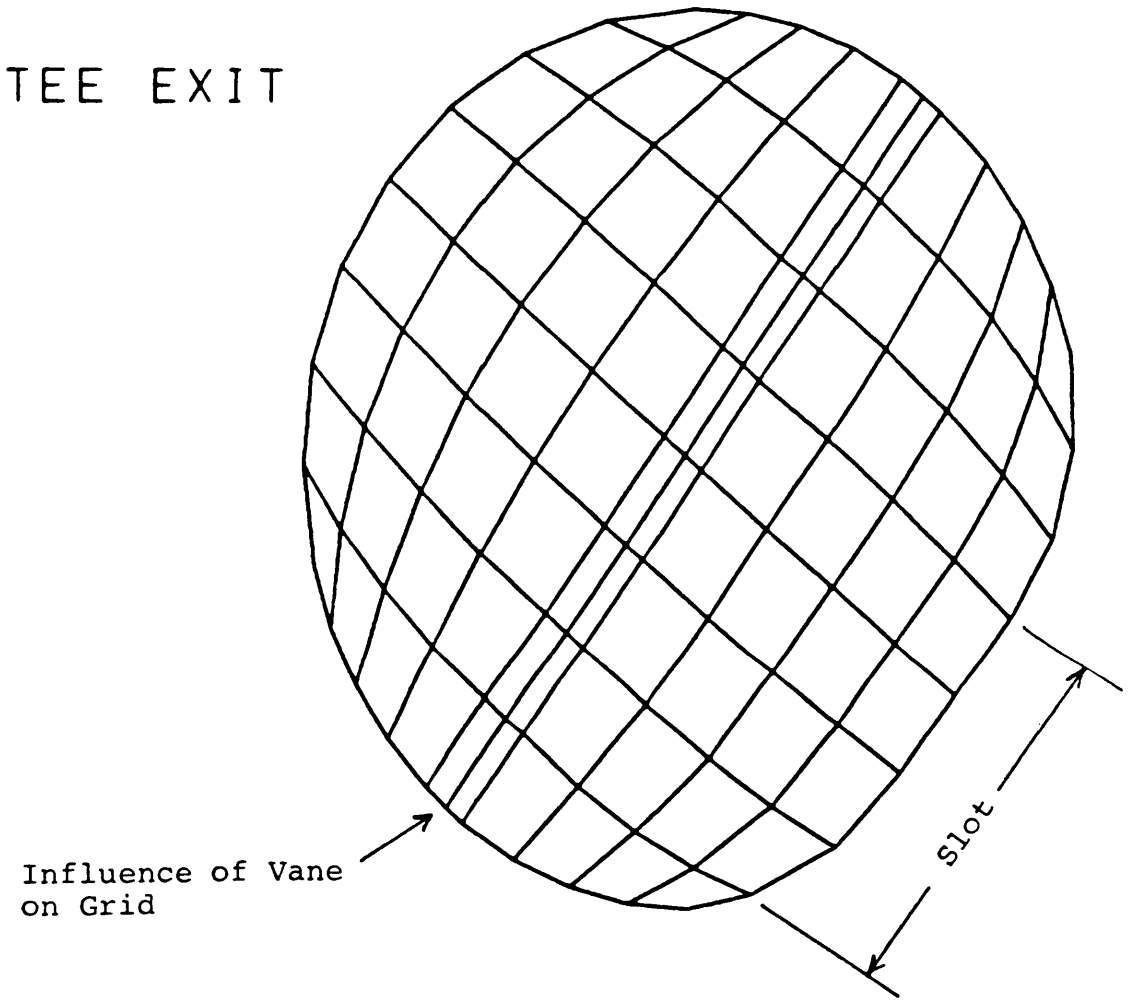

Figure 37. Exit Plane of the Tee.

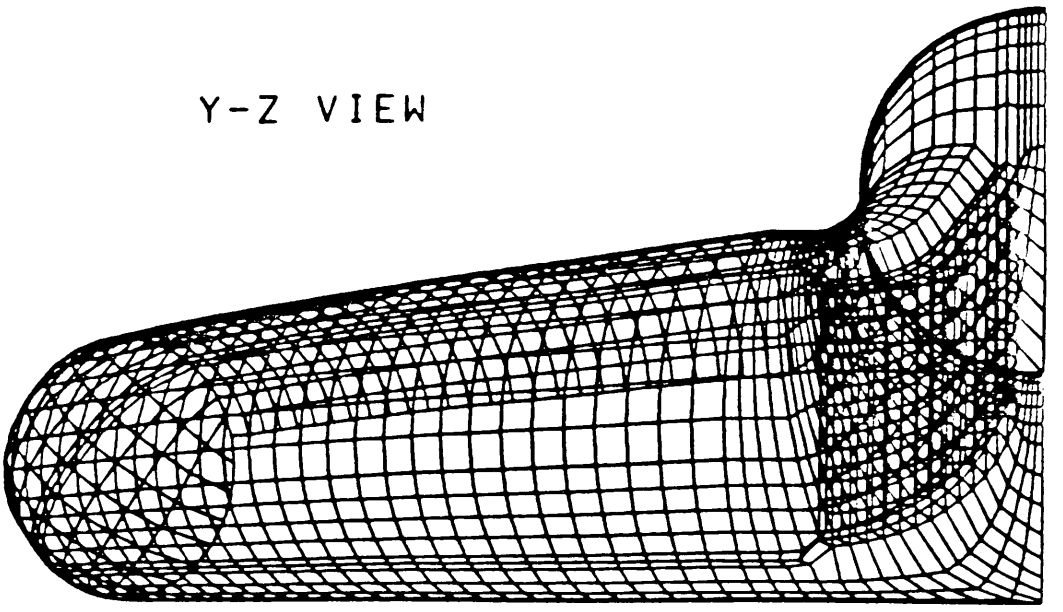

SLOTS

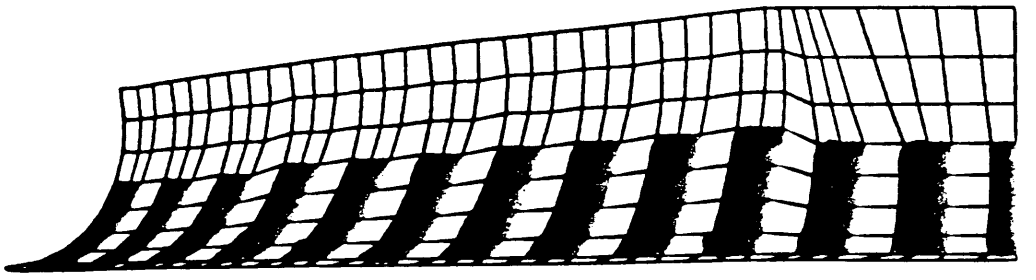

Figure 38. Slots.

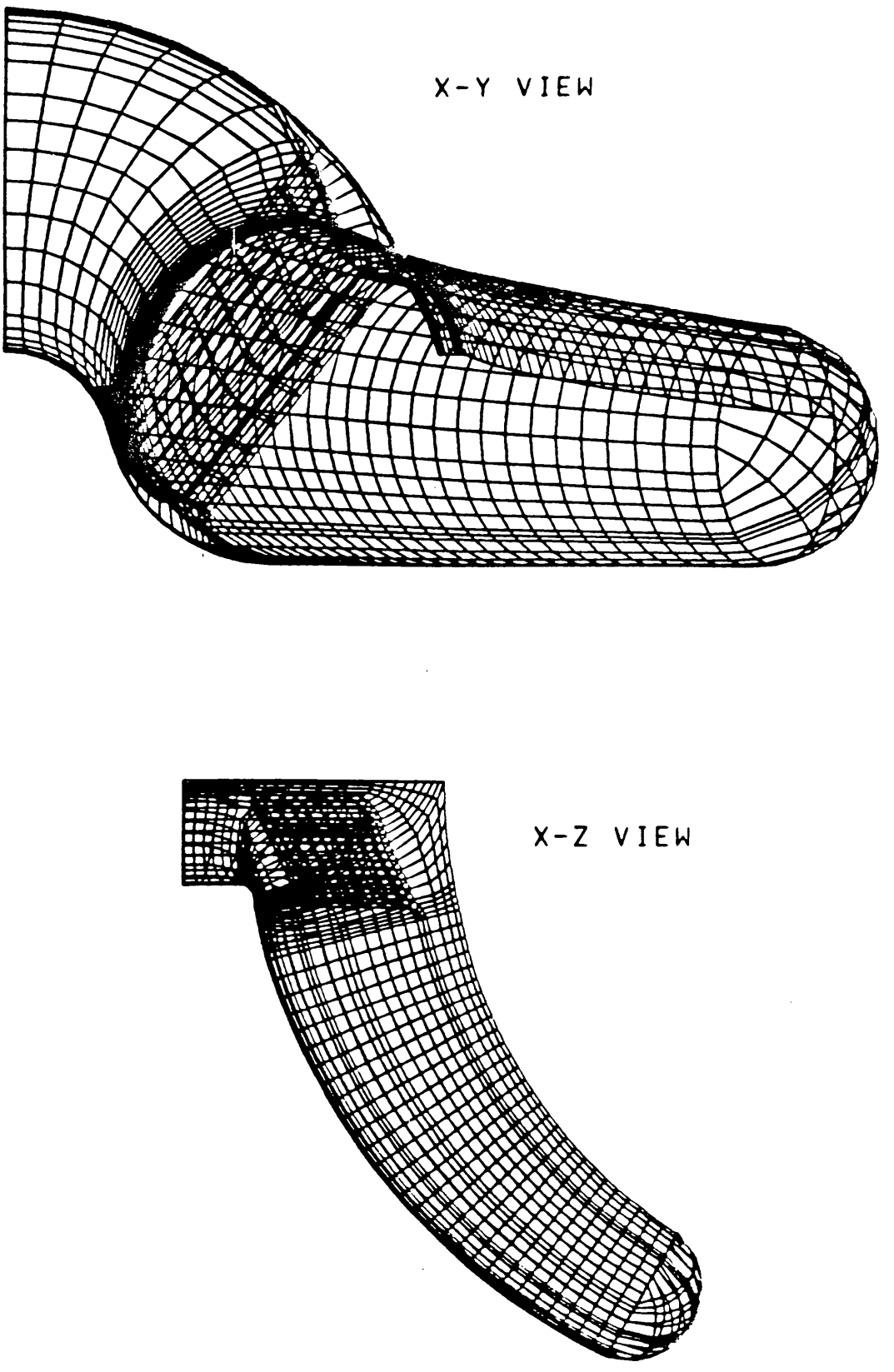

Figure 39. The Hot Dog - Outside View.

the grid distribution across the exit plane of the tee. Figs. 38 and 39 show views of the tee and hotdog. For clarity, the surface containing the slots has been removed and is shown separately. The slots have been darkened in to highlight their locations.

The code was transported to MSFC's CRAY computer where the final grid was generated and verified. Half of the symmetric geometry was modeled, with 99660 nodes. This distribution represents a minimum number of nodes necessary to approximate the Loxtee geometry. Stretching of the nodal distributions in all three directions was employed in an effort to minimize the number of nodes required.

- 3-D LOX Tee Flow

In order to reduce the required memory size, for a problem requiring a large grid size, FDNS3D was reorganized. Presently, FDNS3D can be run with 3.9 mega-words of memory on the Cray-XMP. Since some of the metric coefficients must be calculated repeatedly, this modification caused a two percent increase in CPU time for every time step. However, due to the nature of the non-iterative time marching scheme employed in the FDNS3D code, reasonably efficient turn-around time was still realized.

Initially, computation of a 3-D laminar flow field for the Loxtee was performed. The flow Reynolds number, based on the inlet mean velocity and the vane thickness, was assumed to be 1000. Results of this laminar flow problem were used as an initial flowfield for a turbulent flow case. The code ran at a speed of 1.75E-04 sec/grid/time-step on the Cray-XMP supercomputer which means that about 17 sec/time-step were required for the grid size used. A nearly periodic flowfield

solution, based on the monitoring values of velocity and pressure downstream on the vane trailing edge, was obtained in 1250 time steps. The preliminary results of this laminar flow study are shown in Figs. 40 and 41 and indicate a pressure oscillation frequency close to 4400 Hz. Figure 40 illustrates the perspective views of an instantaneous flow pattern inside the LOX tee geometry. It can be seen from Fig. 40(c) that a large velocity difference on both sides of the vane was predicted. This may have contributed to the high frequency pressure oscillation (compared with the case of uniform flow past a vane).

The velocity profiles upstream of the vane trailing edge, which were shown previously in the 2-D blade study to have substantial effects on the vortex shedding frequency in the wake of the vane, are shown in Fig. 42. Much higher flow speed was predicted along the concave side of the vane than that on the convex side of the vane. This effect is shown in Fig. 42 for the velocity profiles at three vane thicknesses upstream of the trailing edge. These velocity differences on the both sides of the vane can create large shear stress effects on the vortex shedding frequency in the wake. Results of this 3-D analysis can provide useful inflow boundary conditions for a more complete 2-D vortex shedding analyses.

The computation of a turbulent flow with Reynolds number about one million, inside the 3-D LOX tee geometry was accomplished. An extended two-equation turbulence model was used in the analysis. Several modifications to the outlet and wall boundary conditions were made in order to eliminate their influences on the final vortex shedding predictions. First, the outlet mass flow conservation condition was modified to let the flow speed corrections be proportional to the flow rate in each slot. The wall function formulation was also modified to reduce sensitivity to the near-wall grid skewness. However, all these modifications were not sufficient to stabilize the solution for

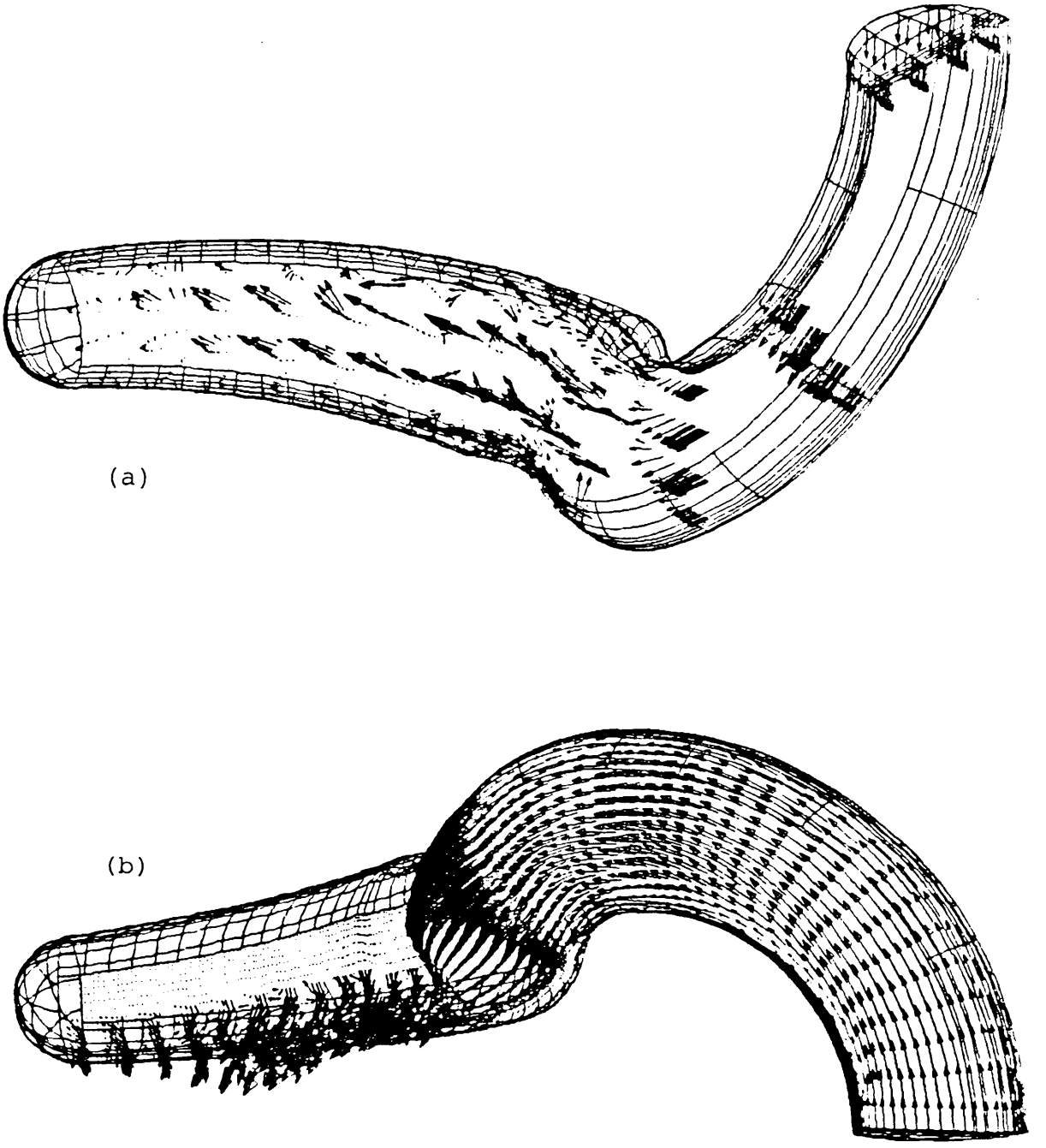

Figure 40. Perspective View for the Instantaneous Flow Pattern in the LOX Tee.

(c)

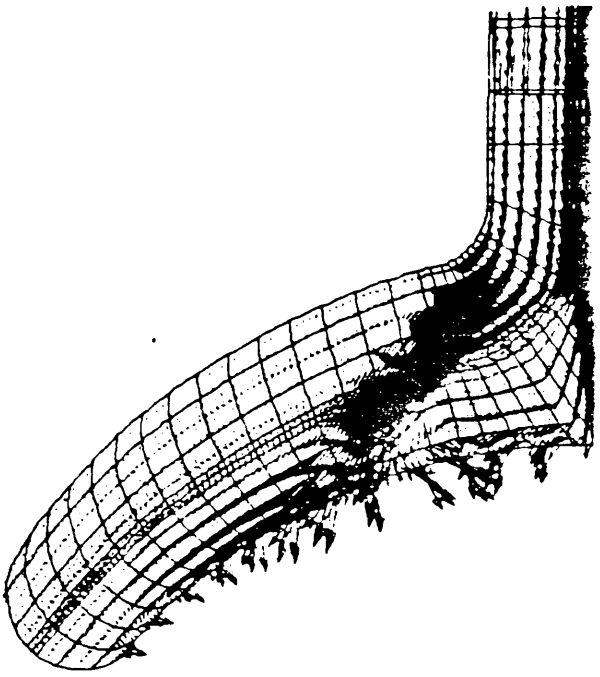

Figure 40. Perspective View for the Instantaneous Flow Pattern in the LOX Tee, Continued.

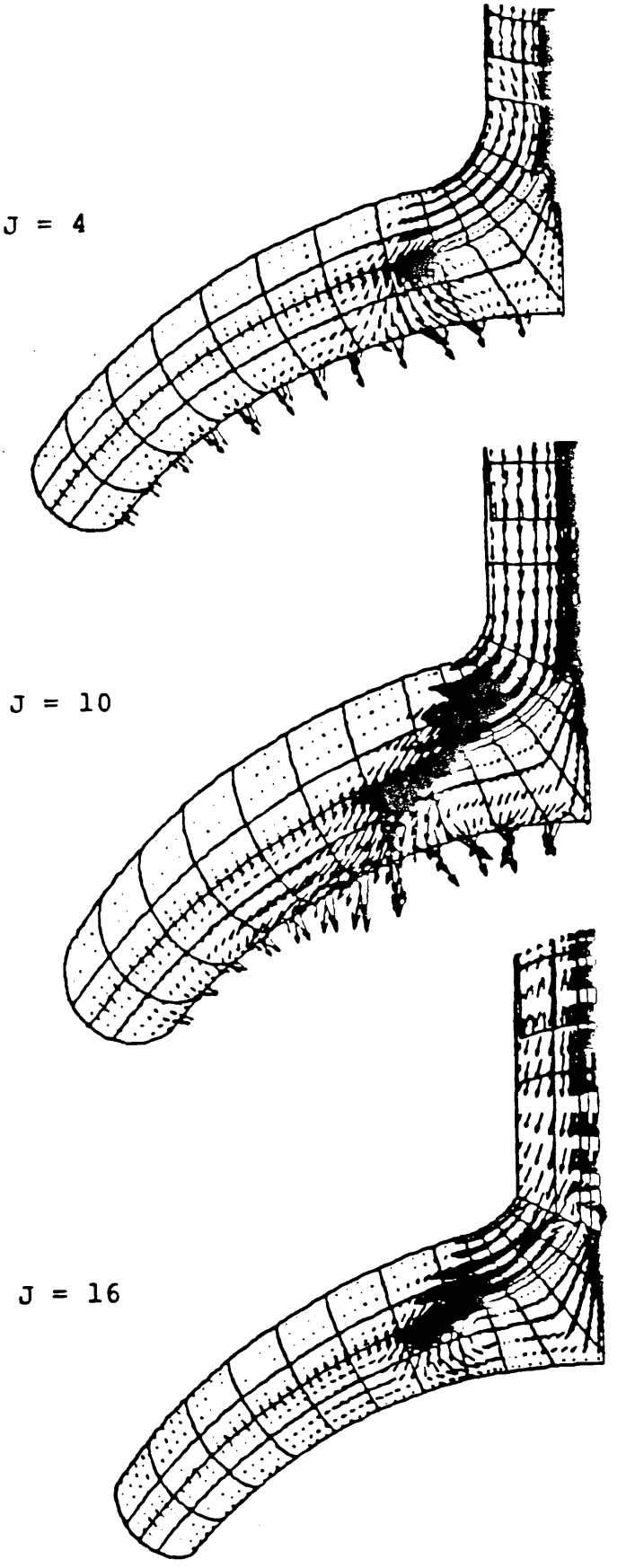

Figure 41. Three Cross Sections of Flow Past the Vane.

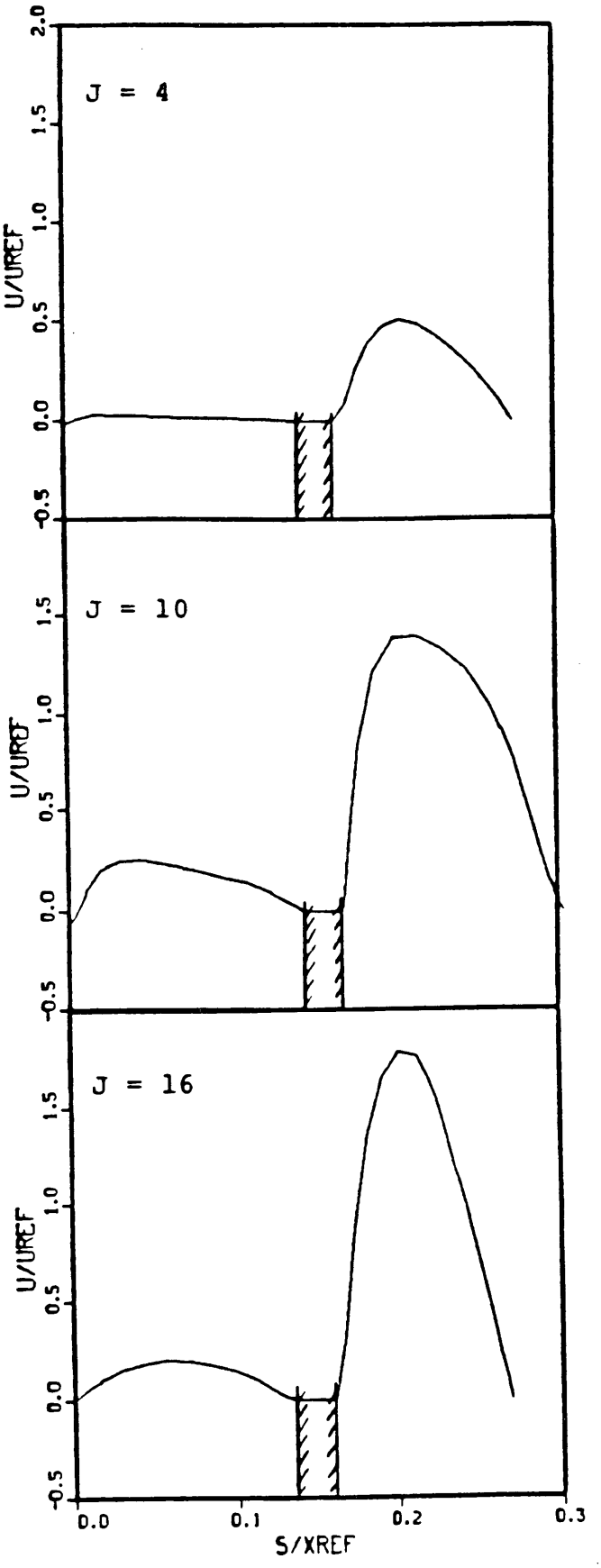

Figure 42. U-Velocity Upstream of Vane Trailing Edge.

this turbulent flow case. Therefore, the mesh near the cap end was modified to reduce the grid skewness near the corner points in the computational domain.

A new mesh system with grid size: 157 x 19 x 33, was generated by modifying the cap end of the tee to reduce the degree of grid skewness near that region, when this modification was made, the turbulent flow case became very stable. Since only a small amount of flow passed through the region at the end of the tee, this modification should not have significent influence on the wake flow solution downstream of the vane. An extended two-equation turbulence model was also employed in this investigation.

The same initial guess of the flowfield used for the laminar flow case was utilized to start the turbulent flow computation. The inlet turbulence intensity and turbulence length scale were assumed to be 5 percent of inlet flow velocity and 3 percent of the inlet duct diameter, respectively. It took 1600 time steps before a nearly periodic solution was obtained. A non-dimensional time step size (based on the inlet velocity and the vane thickness) of 0.02 was used in this case.

Figs. 43(a) - (d) illustrate four flow pattern projections for J=4, 8, 11 and 16 planes respectively. Large recirculation zones on the upper surface of the tee and on the convex surface of the vane were predicted. Except for the stronger recirculation, the basic features of the flow were very similar to the laminar flow solutions. The flow has gone through a sharp turn before exiting from the downstream slots. The entire flow structure was highly three-dimensional, as can be seen from six cross-sectional views (I=61, 71, 81, 91, 93 and 101 planes) of secondary flow patterns given in Figs. 44(a) - (f). Two eddies with counter-clockwise rotation, Fig. 44(a), were formed upstream

(a)

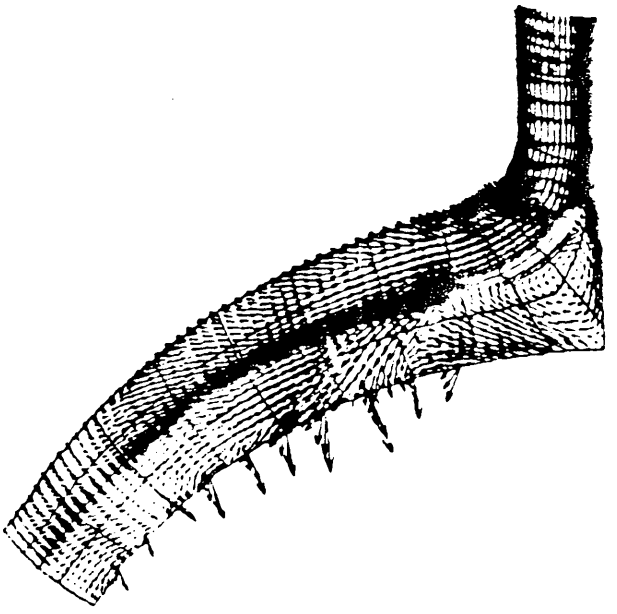

J=4

(b)

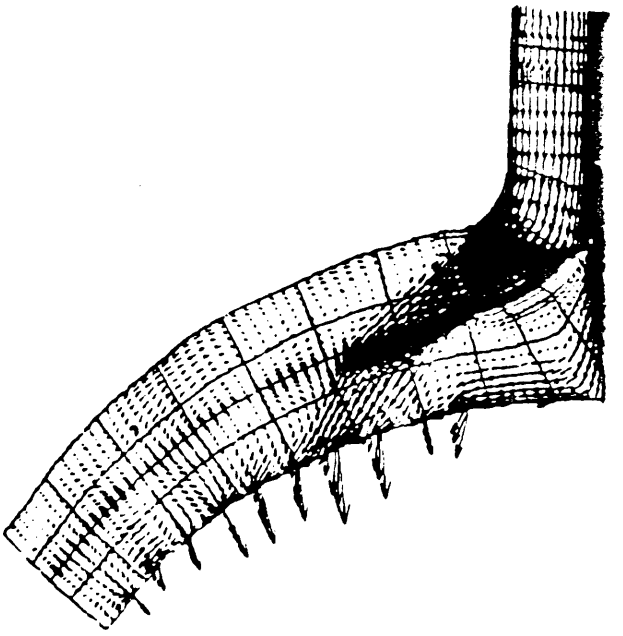

J-8

Figure 43. Turbulent LOX Tee Flow

(c)

J-11

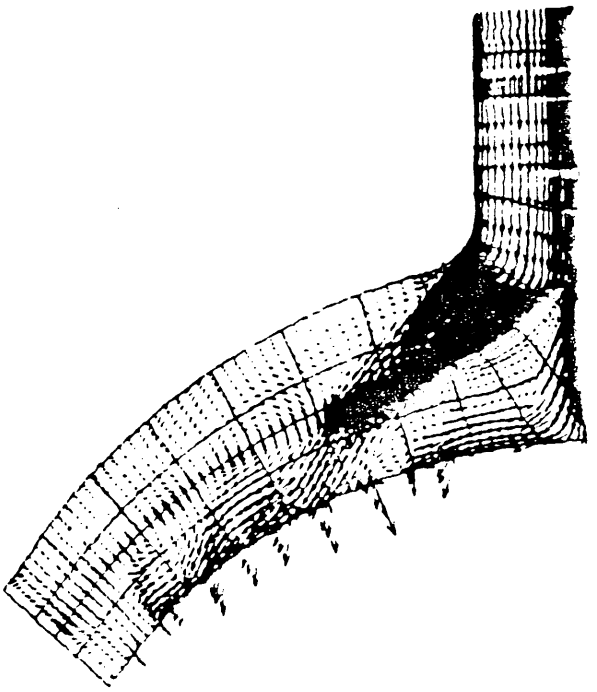

(d)

J=16

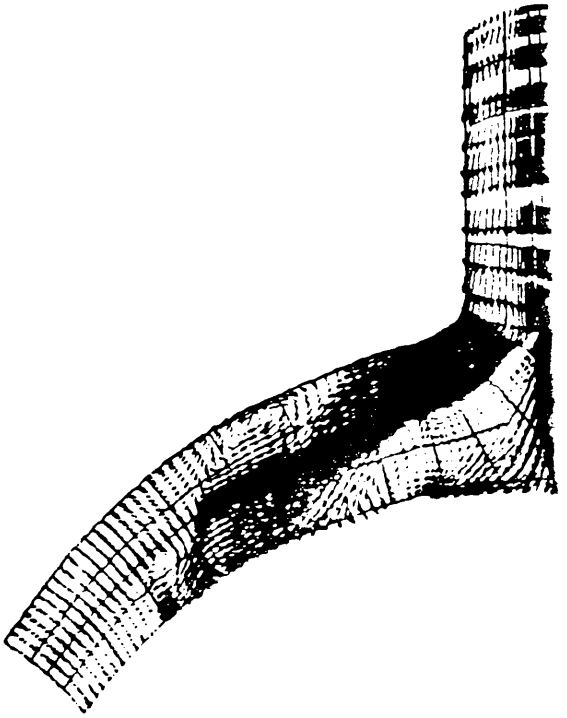

Figure 43. Turbulent LOX Tee Flow, Continued.

(a)

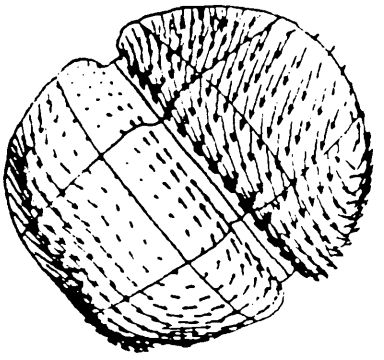

I=61

(b)

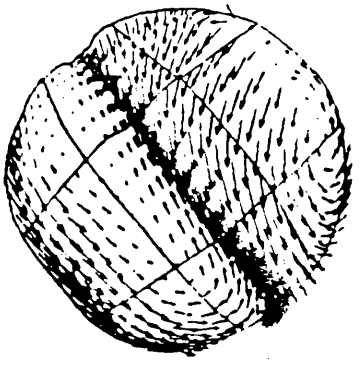

I-71

Figure 44. Turbulent LOX Tee Flow in The Cross-Plane.

(c)

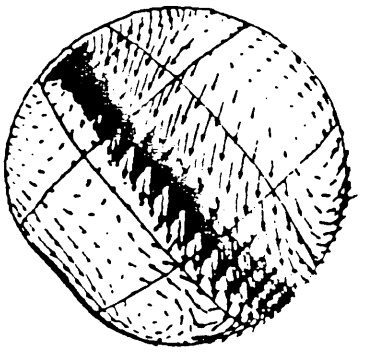

I-81

(d)

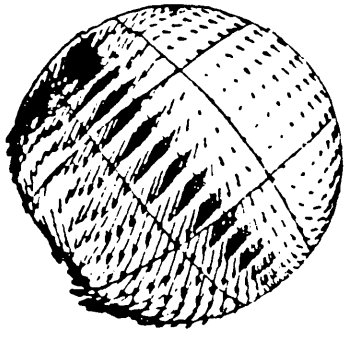

I-91

Figure 44. Turbulent LOX Tee Flow in The Cross-Plane, Continued.

(e)

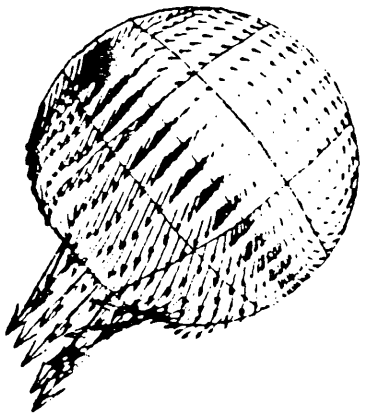

I=93

(f)

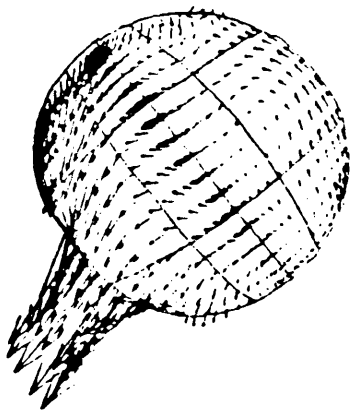

I=101

Figure 44. Turbulent LOX Tee Flow in The Cross-Plane, Continued.

of the vane trailing edge (the vane trailing edge was located at I=67). A strong shear layer was then generated downstream of the vane trailing edge, Fig. 44(b). This pattern persists until a prevailing flow through the exit slots is established, Figs. 44(c) - (f).

The computation of a turbulent flow inside a half-domain LOX tee geometry indicated that a periodic solution was obtained in 2400 time steps. The periodicity was based on the time history of the integrated lift forces on the LOX tee vane. This result showed a Strouhal number of 0.25, or an oscillation frequency of 2485 Hz. The predicted low oscillation frequency may be attributed to the basic assumption of the present simulation that a symmetry boundary condition was imposed along the center plane between two vanes. This may have omitted one important feature of the LOX tee flow; namely that a bi-stable flowfield downstream of the vanes may exist. Experimental observations of the water flow tests suggest that the 4000 Hz oscillations may have originated from the vane to which the flow was attached after a bi-stable flow pattern was established.

Three extensions of the half-plane simulation were made. First, a complete LOX tee geometry was incorporated in the computation. This increases the grid size to around 200,000 nodes. In order to run this problem within 4M words memory size, a multi-zone algorithm was implemented by using the SSD device on the Cray-XMP. Two blocks of SSD areas were used to store the grid and flow variables of two zones. For each time step, data for each zone were read from SSD in sequence. Solutions of each zone were then stored back to SSD after every time integration. This procedure was tested and found to be successful. However, due to the necessity of doing SSD input/output, the CPU time required for each time step has increased by a factor of 4.

Three hundred time steps were completed using this method. At the end, the flowfield was still symmetric with respect to the symmetry plane. Figs. 45(a) - (d) show the velocity fields on 4 J-planes. The integrated forces on both vanes were also found to be coincidental for each time step. This suggested that further runs would not be able to produce a bi-stable flowfield. The initial guesses of the flowfield and the outlet mass flow rate distributions, which were symmetric at the beginning, may have prevented the development of a bi-stable solution.

An alternative to the above approach could also be employed to study the effect of the bi-stable flowfield on the vortex shedding frequency. An excess mass flow can be assigned along the symmetry plane downstream of the vane of the half-domain. It can be assumed that the entire mass flow through the gap between the vanes is attached to one of the vanes. This approach may give reasonable results with more efficient computer turn-around time. This approach was not tested, rather a fully coupled, entire tee domain simulation was performed on the NASA/Ames Cray.

In order to have a better turn-around time in the computation of a full 3-D turbulent flow around the LOX tee vanes using a multizone approach, the NASA/Ames Cray-2 and Cray-YMP supercomputers were used to carry out the calculations. The Cray-2 and Cray-YMP computers can handle a much larger grid size than Marshall's Cray-XMP. A two-block mesh system with a grid size of 2 x (157 x 19 x 33) was generated using the grid generator. This size of mesh system requires about 8 mega-words of memory when using the FDNS code with two-equation turbulence models. A new zonal interface routine was incorporated in the FDNS code to provide faster data updating along the interface without using the solid state device (SSD). This zonal interface interpolation procedure is performed in parallel with the matrix solver in the FDNS. This two-zone method was running at speeds

(a) J = 4

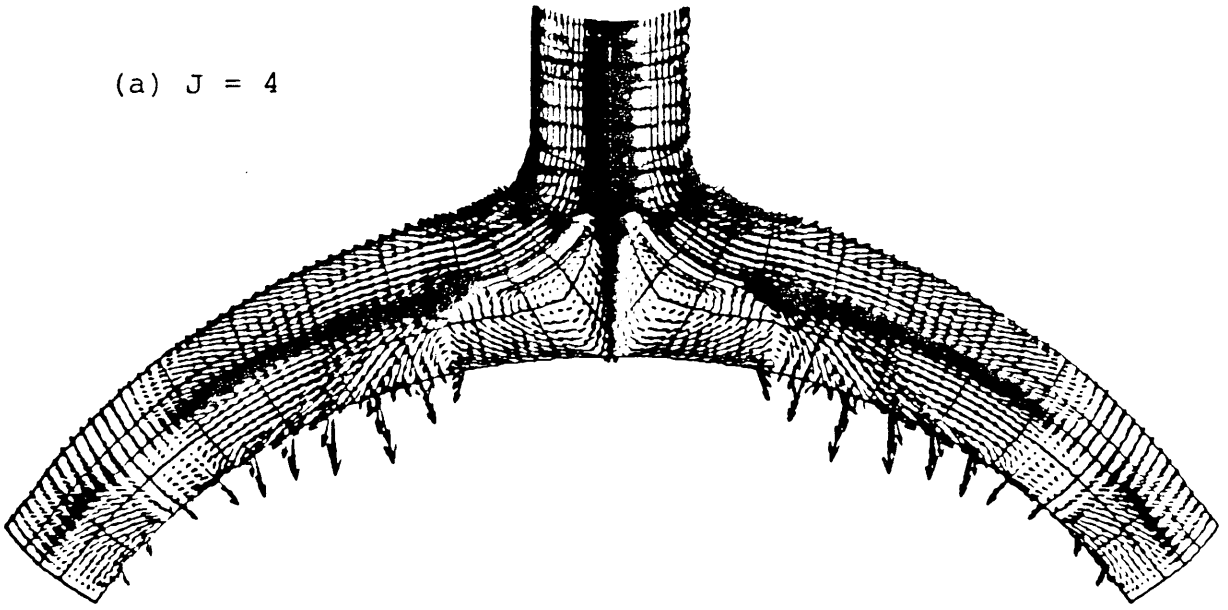

(b) J = 8

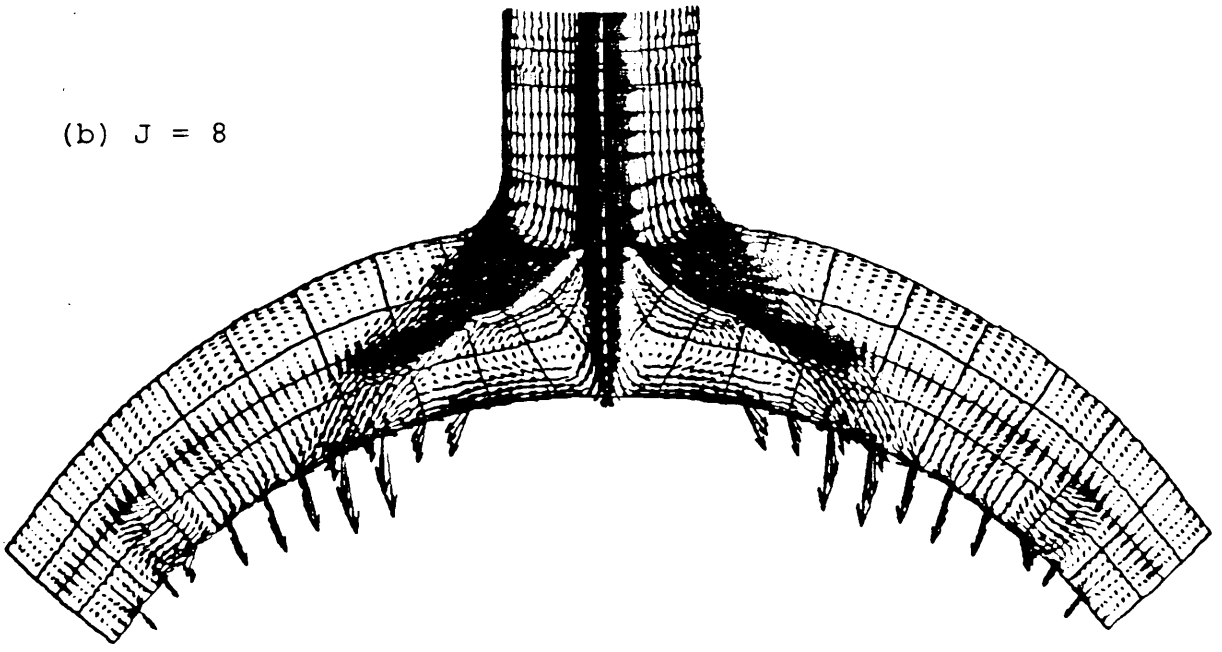

Figure 45. LOX Tee Flowfield for a Full-Domain Calculation, Continued.

(c) J = 11

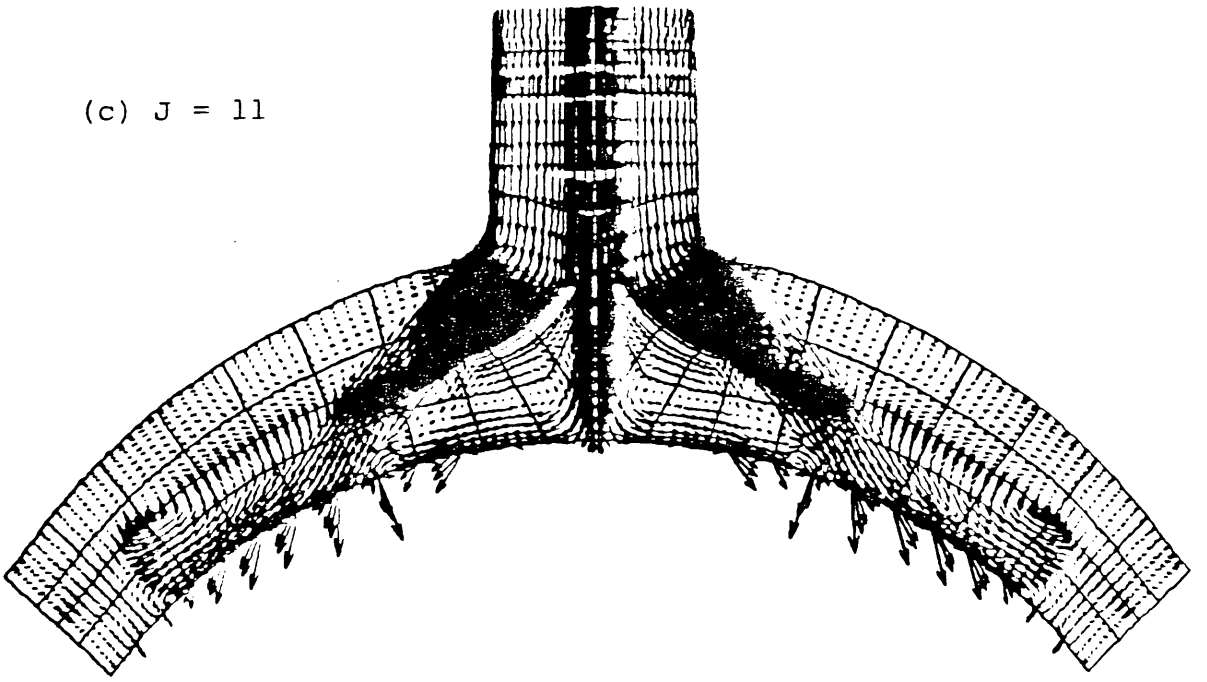

(d) J = 16

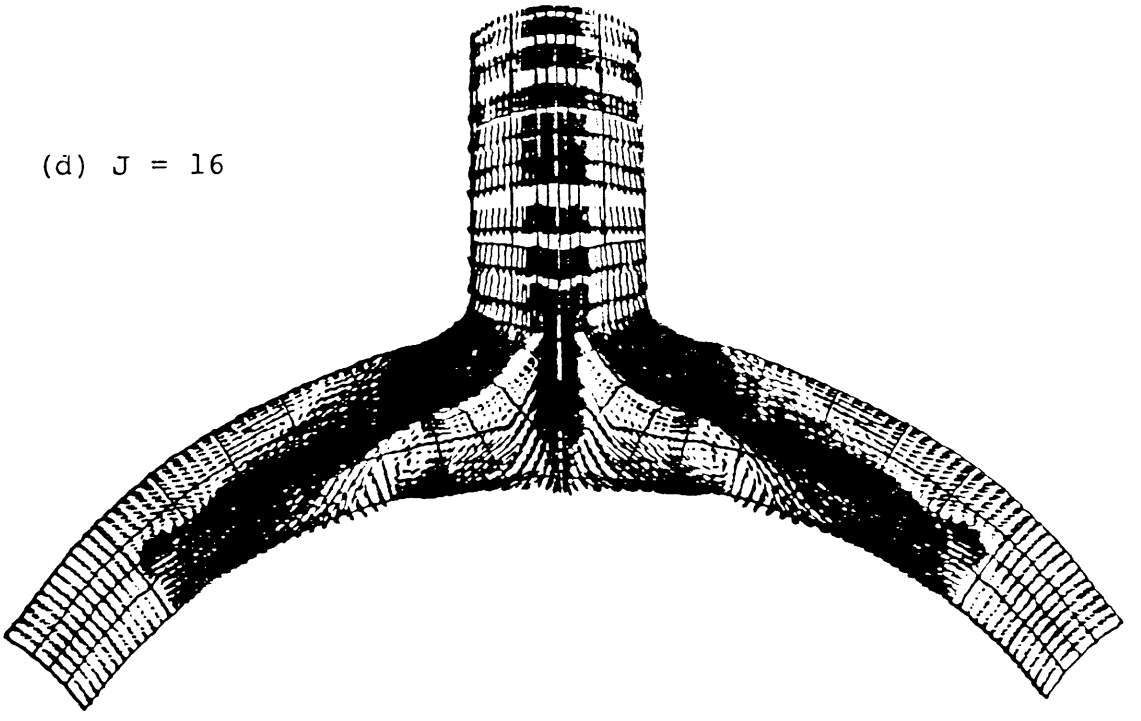

Figure 45. LOX Tee Flowfield for a Full-Domain Calculation, Continued.

of 75 sec/time-step and 25 sec/time-step on the Cray-2 and the Cray-YMP computers respectively. These are about 3 and 9 times faster than the case using the two-zone SSD on the Cray-XMP. Since much better turn-around was experienced using the Cray-YMP machine, most of the results presented here were computed using the Cray-YMP computer. Eleven consecutive runs (a total of 1699 time steps) with a dimensionless time step size of 0.02 (normalized with the vane thickness and the average inlet velocity) were performed. Subsequently, an additional run of 517 time steps with a dimensionless time step size of 0.01 was completed.

With 98,439 nodes representing one-half of the flow domain (a zonal interface is located between two vanes), the grid resolution is considered to be coarse compared with that which was used for the 2-D cases. It would be difficult to obtain accurate time-resolved vortex shedding structures with the current grid density. The main objective of this 3-D case is therefore aimed at the general flow patterns around the LOX tee vanes.

Figs. 46 shows the final result of the 0.02 time step case mentioned above; the calculated lift coefficient and monitoring values of pressure and velocity at a point inside the near-wake of one of the vanes with respect to the normalized time are shown in this figure. It is clear from these results that the solutions have not yet reached a quasi-steady-state vortex shedding pattern. This may be caused by the coarse grid in the wake regions or by disturbances from boundary conditions imposed along the exit boundary (which is not far away from the vane trailing edges). However, results of this investigation have indicated different lift forces on the two LOX tee vanes which also indicate non-symmetric flow patterns on the downstream side of the vanes. The same features were not found in the previous

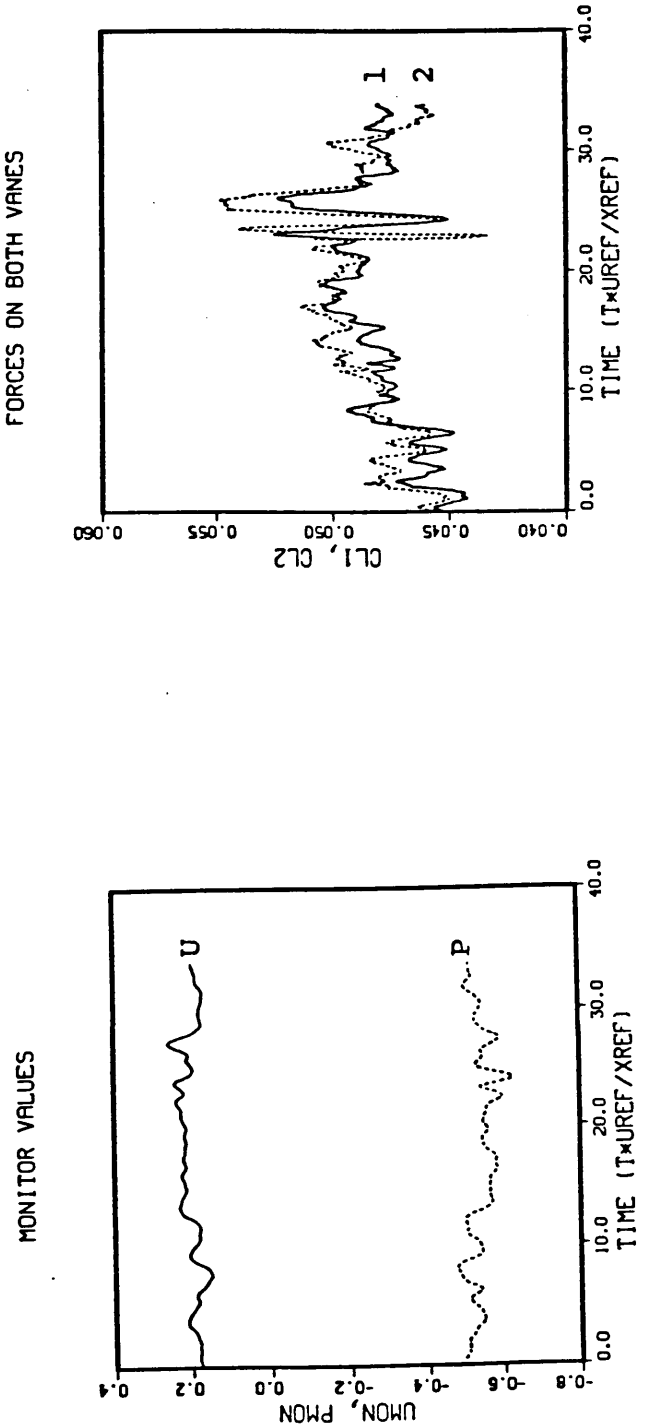

Figure 46. Calculated Monitoring Parameters for the Full 3-D LOX Tee Flowfield

investigations using two-zone SSD approach on the Cray-XMP. This phenomenon is consistent with the experimental observations in a water flow test program. Fig. 47 and 48 illustrate several cross-sections of the predicted flow pattern at the end of the calculation. The predicted velocity distributions upstream of the trailing edge of the vane indicate more attached flow along the suction surface, in the plane shown on p. 86. Again, large velocity differences on both sides of the vane were predicted in this investigation. But, the velocity difference magnitudes are less than that of the previous one-zone solution with symmetric boundary conditions. This is also consistent with the water flow test results and the assumption made in the calculations for 2-D vane configurations.

In summary, based on the 2-D results, half a million grid points would be required to resolve the vortex shedding structure in the LOX tee. Therefore, the 200,000 grid points used for the 3-D calculation indicate only the general features of the flowfield. These general flow features are useful for making a more thorough 2-D vane wake analysis. Due to the near proximity of the surface on which exit conditions are specified to the vanes in the tee, exit boundary conditions should be further investigated to more accurately simulate the LOX tee flow.

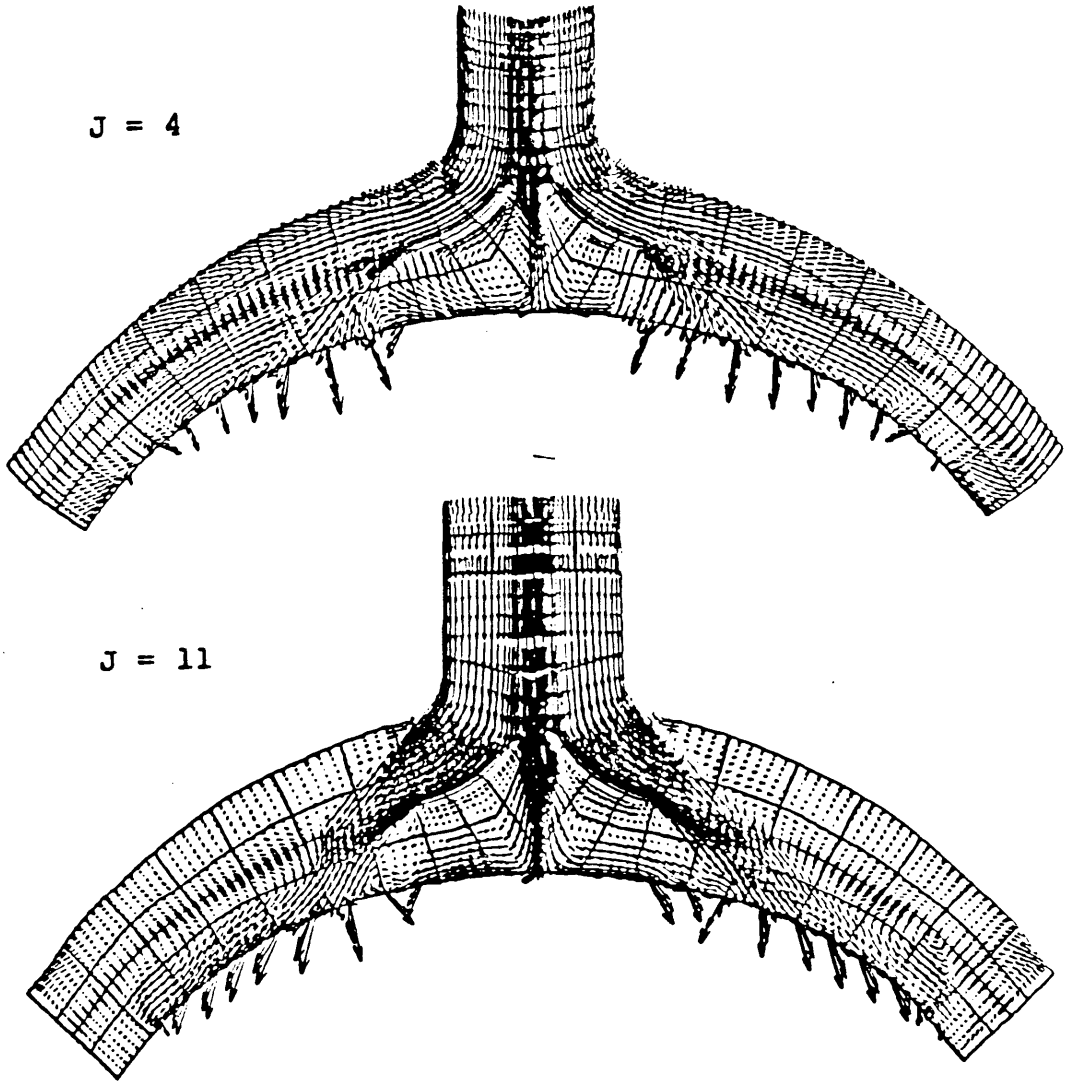

Figure 47. Velocity Vectors for the Full 3-D LOX Tee Flowfield

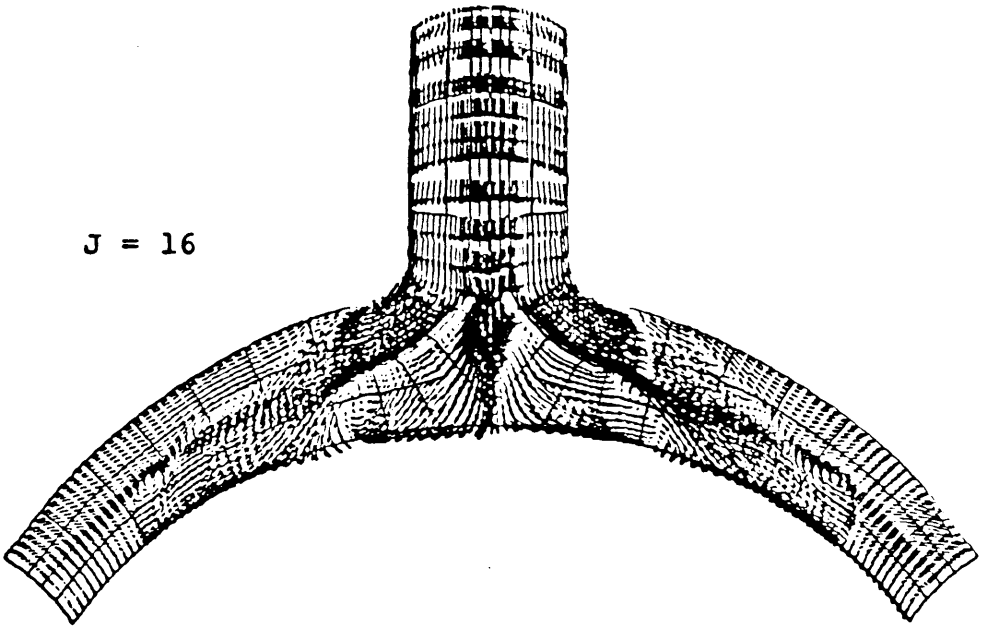

Figure 47. Velocity Vectors for the Full 3-D LOX Tee Flowfield, Continued

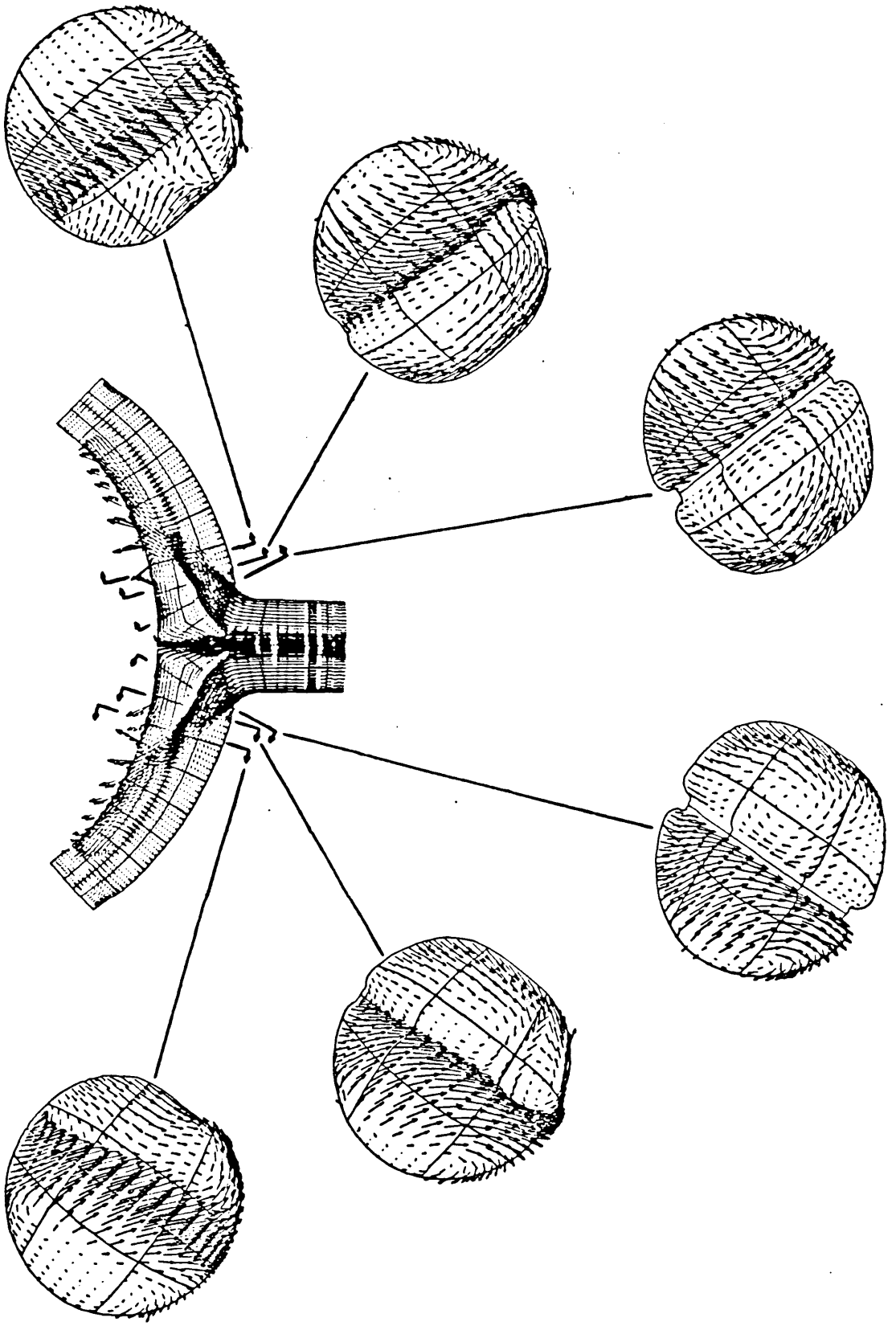

Figure 48. Flow over the Vanes for the Full 3-D LOX Tee Flowfield

CONCLUSIONS AND RECOMMENDATIONS

Based on the computational results reported herein and the apparent success of the proposed fix to the 4000 Hz problem which NASA and Rocketdyne are currently using, SECA offers the following conclusions and recommendations for this investigation.

1. The FDNS CFD code was verified to be useful in analyzing unsteady oscillating phenomena at least up to the 6 kHz range using wall function boundary conditions and a sufficiently dense computational grid.

2. The two-dimensional blade wake investigation demonstrated that flow disturbances at the 4000 Hz frequency level could originate in the wake of the splitter vanes. Furthermore, analyses of this type could be used to avoid flow conditions and geometric configurations which might cause similar problems in future engine designs.

3. Full 3-dimensional CFD solutions for LOX tee flow were generated. These solutions revealed the general features of the flowfield, but current computer size and speed limitations prevent a sufficiently detailed analysis to identify wake fluctuation features. The general flow features are suitable for use as boundary conditions for detailed 2-dimensional wake analyses.

4. Even though the physics simulated in a CFD solution is correct, complex 3-dimensional problems, like the LOX tee flow, must still be addressed by looking in detail at small, select regions of the overall flowfield. Carefully designed parametric CFD investigations of unsteady, internal liquid flows can yield invaluable design information.

REFERENCES

1. Struck, H.G. MSFC memo ED31-85-58, p. 43, December 2, 1985.

2. Struck, H.G. MSFC memo ED31-86-34, p. 43, May 20, 1986.

3. Rogers, S.E., and D. Kwak, "An Upwind Differencing scheme for the Time-Accurate Incompressible Navier-Stokes Equations," AIAA-88-2583, AIAA 6th Applied Aerodynamics Conference, Williamsburg, VA, June 6-8, 1988.

4. Roder, H.M., and L.A. Weber, "ASRDI Oxygen Technology Survey, Vol. I: Thermophysical Properties," NASA SP-3071, 1972.

5. Wang, T.S., et al, "Investigation of the Transient Fuel Preburner Manifold and Combustor," Rpt. No. 89-10, SECA, Inc., Huntsville, AL, June, 1989.

6. Hirschfelder, J. D., et al, "Generalized Equation of State for Gases and Liquids," I. & E. Chem., 50, pp. 375-385, March 1958.

7. Coutanceau, and Bouard, " JFM, 79, pp. 231-256, 1977.

8. Braza, et al, JFM, 165, pp. 79-130, 1986.

9. Hinze, "Turbulence," 1975.

10. Welty, et al, Fundamentals of Momentum, Heat & Mass Transfer, Wiley, 1976.

11. Schlichting, H., Boundary Layer Theory, McGraw Hill, 1979.

12. Baldwin, B. and H. Lomax, AIAA Paper 78-257, 16th Aerospace Sciences Meeting, Huntsville, AL, Jan 16-18, 1978.

13. Chien, AIAA J, 20, 1982.

14. Patel, V.C., et al, AIAA J, 23, pp. 1308, 1985.

15. So, et al, AIAA Paper No. 88-3583 - CP, 1988.

16. Chen, Y.S., "Viscous Flow Computations Using a Second-Order Upwind Differencing Scheme," AIAA-88-0417, 26th Aerospace Sciences Meeting, Reno, NV, January 11-14, 1988.

17. Chen, Y.S., "Compresssible and Incompressible Flow Computations with a Pressure Based Method," AIAA-89-0286, 27th Aerospace Sciences Meeting, Reno, NV, January 9-12, 1989.

18. Haji-Haidari, A., and C. R. Smith, "A Comparative Study of the Development of the Turbulent Near-Wake Behind a Thick Flat Plate with both a Circular and Tapered Trailing Edge Geometry," Report FM-6, M. E. Dept., Lehigh University, October 1984.

19. Liu, B.L., et al, "Time-Dependent Navier-Stokes Computations For Flow-Induced Vibrations on a Vane," Advanced Earth-to-Orbit Propulsion Technology 1989, NASA Conference, 1989.

APPENDIX A - LWIND

1. INTRODUCTION

This document describes LWIND, a code developed by SECA, Inc., to provide solutions to complex liquid flow problems. LWIND solves the Navier-Stokes equations using an equation of state for liquids that accurately defines the liquid in the flow regime of interest. The code currently operates in 2-D or axisymmetric modes with options for inviscid, laminar or turbulent flows. Both Baldwin-Lomax and k-ε turbulence models have been included in the code. In addition to the algorithm discussed below, the code has a grid generator, a preprocessor and a graphics package.

The following sections present the derivations of the liquid equation of state and thermodynamic properties and the windward algorithm employed by the code.

2. THERMODYNAMIC PROPERTIES OF LIQUIDS

This section discusses the derivations of the equation of state, enthalpy and internal energy for any liquid. These relationships are to be used in a Navier Stokes solver and, therefore, must be consistent with the continuity, momentum and energy equations. Namely, the density must be the inverse of the specific volume, the internal energy and enthalpy must differ only by P/ρ, and the eigenvalues of the set of equations must involve only the velocity and speed of sound. For instance, many text books assume ρ is constant in the derivation of the equation of state. This leads to an inconsistency between density and specific volume which, in turn, results in inconsistencies between internal energy and enthalpy and extraneous terms in the eigenvalues. The following derivations result in a set of relations for the liquid thermodynamic properties which is consistent throughout the analysis.

2.1 Equation of State

The thermal equation of state for any fluid may be expressed in a differential form as

$$d\rho = (\partial\rho/\partial T)_P \, dT + (\partial\rho/\partial P)_T \, dP$$

where ρ is the density, P is the pressure and T is the temperature. But, by definition

$$(\partial\rho/\partial T)_P \equiv -\rho\beta$$

where β is the coefficient of volume expansion and

$$(\partial\rho/\partial P)_T \equiv \rho\kappa$$

where κ is the isothermal compressibility. Substituting these definitions into the equation of state and rearranging yields

$$d\rho/\rho = -\beta dT + \kappa dP$$

It is at this point that the assumption of constant ρ results in the aforementioned inconsistency. Instead, assume that β and κ are constant over the range of interest for a given problem and are evaluated at reference conditions ρ_r, P_r, and T_r. Integrating the equation of state yields

$$\ln \rho = -\beta T + \kappa P + C_\rho$$

where C_ρ is a constant of integration evaluated at the reference conditions. That is

$$C_\rho = \ln \rho_r - \kappa P_r + \beta T_r$$

For multi-component mixtures of miscible liquids the density of the fluid is the sum of the densities of the components. Care should be taken in the assumption of miscibility of the components. If the components α are mixed at the same pressure and temperature, the equation of state becomes

$$\ln \rho = \ln(-T\sum_\alpha \beta_\alpha + P\sum_\alpha \kappa_\alpha) + C_\rho$$

where $\beta = \sum_\alpha \beta_\alpha$, $\kappa = \sum_\alpha \kappa_\alpha$, and C_ρ is for the mixture only.

The static pressure is obtained directly from the equation of state

$$P = (\beta T + \ln \rho - C_\rho)/\kappa$$

If the reference conditions are judiciously chosen from thermodynamic property data for any liquid, the above equation of state will usually be valid over a sufficient range of pressures and densities.

2.2 Enthalpy

The enthalpy of any fluid may be derived using the same process. The differential form of the equation for enthalpy is given by (Ref. Sears, Thermodymanics, p 169)

$$dH = (\partial H/\partial T)_P \, dT + (\partial H/\partial P)_T \, dP$$

C-2

$$= C_p dT + [v - T(\partial v/\partial T)_p]dP$$

where H is the enthalpy, v is the specific volume, and C_p is the specific heat at constant pressure. Some mathematical manipulation using the Chain Rule leads to

$$dH = [C_p - (\beta^2 vT/\kappa)]dT - dv/\kappa + (\beta/\kappa)d(vT)$$

where, referring to Sears, p. 149,

$$C_p - (\beta^2 vT/\kappa) = C_p - (C_p - C_v) = C_v$$

It can be shown (Sears, p. 150) that the specific heat at constant volume C_v is independent of the specific volume v if the pressure is a linear function of the temperature. Referring to the equation for pressure above, it can be seen that pressure is indeed linear in temperature. Therefore,

$$C_p - (\beta^2 vT/\kappa) \cong C_p - (\beta^2 v_r T/\kappa)$$

Since C_p varies little it can be assumed constant. These relations reduce the equation for enthalpy to a form which is easily integrated.

$$dH = [C_p - (\beta^2 v_r T/\kappa)]dT - dv/\kappa + (\beta/\kappa)\, d(vT)$$

Integrating the above equation yields

$$H = C_p T - (\beta^2 v_r T^2/2\kappa) - v/\kappa + \beta vT/\kappa + C_H$$

where C_H is a constant of integration

$$C_H \equiv H_R - C_p T_r + (\beta^2 T_r{}^2/2\kappa\rho_r) + 1/\kappa\rho_r - (\beta T_r/\kappa\rho_r)$$

Now the equation for enthalpy becomes

$$H = C_a T - 1/\kappa\rho + \beta T/\kappa\rho + C_H$$

where $C_a \equiv 0.5(C_p + C_v)$

For multiple components the intensive enthalpies are additive, that is

$$\rho H = \sum_\alpha \rho_\alpha H_\alpha$$

The enthalpy equation becomes

$$\rho C_a T - 1/\kappa + \beta T/\kappa + \rho C_H = \sum_\alpha [\rho_\alpha (C_a)_\alpha T - 1/\kappa_\alpha + T\beta_\alpha/\kappa_\alpha + \rho_\alpha (C_H)_\alpha]$$

Comparison of the two sides of the above relation infers the following relations for multiple component liquids.

$$\rho C_p = \sum_\alpha \rho_\alpha (C_p)_\alpha$$

$$\rho C_v = \sum_\alpha \rho_\alpha (C_v)_\alpha$$

$$\rho C_H = \sum_\alpha \rho_\alpha (C_H)_\alpha$$

2.3 Internal Energy

The equation for internal energy may be derived using the same method, starting with the differential form (Sears p. 148)

$$dE = (\partial E/\partial T)_v dT + (\partial E/\partial v)_T dv = C_v\, dT + (\beta T/\kappa - P)dv$$

Applying manipulations similar to those for enthalpy and integrating yields

$$E = C_p T - (\beta^2 T^2/2\kappa\rho_r) + (v \ln v - v + C_\rho v)/\kappa + C_E$$

$$E = C_a T - 1/\kappa\rho + \beta T/\kappa\rho - P/\rho + C_E$$

Comparing this equation to the equation for enthalpy indicates that relationship $H = E + P/\rho$ is satisfied if $C_E = C_H$, therefore the equation for internal energy becomes

$$E = C_a T - 1/\kappa\rho + \beta T/\kappa\rho - P/\rho + C_H$$

2.4 Speed of Sound

A relationship for the speed of sound will be required for the eigenvalue analysis to follow. The equation for the speed of sound is (Sears p. 155-156)

$$C^2 = 1/\rho\kappa_S$$

where k_S is the adiabatic compressibility. Denoting the ratio of specific heats as γ, the adiabatic compressibility becomes

$$\kappa_S \equiv \kappa/\gamma$$

and the speed of sound relationship becomes

$$C^2 = \gamma/\rho\kappa$$

2.5 Derivatives

The formulation of the Jacobian matrices in the following section will require taking the derivatives of pressure and enthalpy. These derivatives were derived realizing that the partial derivatives of the independent variables with respect to each other are zero.

2.5.1 Pressure

Starting with the relationship for pressure

$$P = (\beta T + \ln \rho - C_\rho)/\kappa$$

the derivative of pressure with respect to θ becomes

$$\partial P/\partial \rho = C^2 - \alpha(H_T - q^2)$$

where α is defined as $\beta/\kappa\rho C_v$. Also,

$$\partial P/\partial \rho u = \beta(-u/\rho C_v)/\kappa = - \alpha u$$

$$\partial P/\partial \rho v = - \alpha v$$

$$\partial P/\partial \rho E_T = \alpha$$

2.5.2 Total Enthalpy

$$\partial H_T/\partial \rho = [C^2 - \alpha(H_T - q^2) + H_T]/\rho$$

$$\partial H_T/\partial \rho u = - \alpha u/\rho$$

$$\partial H_T/\partial \rho v = - \alpha v/\rho$$

$$\partial H_T/\partial \rho_T = (\alpha + 1)/\rho$$

The relations derived in this section will be used in the next section to provide the thermodynamic properties of the liquid for the windward algorithm.

3. WINDWARD ALGORITHM

An explicit windward algorithm using a finite volume flux splitting technique has been developed for solving the conservation equations for a liquid. The explicit method was chosen because of the need to solve real time problems. Total conservation in the integral sense is guaranteed by employing the elemental flux integrals to form the spatial derivatives found in the conservation equations. The viscous terms in the flow equations are resolved using standard central differences and are

not included in the following discussion of the derivation of the algorithm. The energy equation is included to permit the treatment of heat transfer or liquids with different energy levels.

For 2-D and axisymmetric flow, the conservation equations may be cast in the form:

$$Q_t + F_x + G_y + \sigma H/y = 0$$

$$Q = [\rho, \rho u, \rho v, \rho E_T]^T$$

$$F = [\rho u, \rho u^2 + P, \rho uv, \rho u H_T]^T$$

$$G = [\rho v, \rho uv, \rho v^2 + P, \rho v H_T]^T$$

$$H = [\rho v, \rho uv, \rho v^2, \rho v H_T]^T$$

where t is time; x & y are Cartesian coordinates; u & v are velocity components in the x & y directions, respectively; ρ is density; P is pressure; E_T is total specific internal energy; H_T is total specific enthalpy and σ = 1 for axisymmetric flow and σ = 0 otherwise.

The conservation equations may be transformed to local, computational coordinates (ξ,η) where $\Delta\xi = \Delta\eta = 1$.

$$(y^\sigma/J)Q_t + (y^\sigma \hat{F})_\xi + (y^\sigma \hat{G})_\eta + \sigma\hat{H} = 0$$

where:

$$J = \xi_x \eta_y - \xi_y \eta_x$$

$$\xi_x = J\, y_\eta$$

$$\eta_x = -J\, y_\xi$$

$$\xi_y = -J\, x_\eta$$

$$\eta_y = J\, x_\xi$$

$$\hat{F} = [\rho\hat{U}, \rho u\hat{U} + \xi_x P/J, \rho v\hat{U} + \xi_y P/J, \rho\hat{U}H_T]^T$$

$$\hat{G} = [\rho\hat{V}, \rho u\hat{V} + \eta_x P/J, \rho v\hat{V} + \eta_y P/J, \rho\hat{V}H_T]^T$$

$$\hat{H} = [0, 0, -P/J, 0]^T$$

$$\hat{U} = (\xi_x/J)u + (\xi_y/J)v$$

$$\hat{V} = (\eta_x/J)u + (\eta_y/J)v$$

The vectors $\hat{F}$ and $\hat{G}$ can be locally linearized by first

obtaining the Jacobian matrices using the formulas

$$\hat{F}_\xi = \frac{\partial \hat{F}}{\partial Q} Q_\xi = A\, Q_\xi$$

$$\hat{G}_\eta = \frac{\partial \hat{G}}{\partial Q} Q_\eta = B\, Q_\eta$$

The mathematical treatment of the Jacobian matrices A and B is identical, therefore by letting D represent A or B, n represent ξ/J or η/J, and $U = n_x u + n_y v$, the D matrix becomes

$$D = \begin{bmatrix} 0 & n_x & n_y & 0 \\ -uU + n_x\theta^2 & U + (1-\alpha)un_x & un_y - \alpha v n_x & \alpha n_x \\ -vU + n_y\theta^2 & vn_x - \alpha u n_y & U + (1-\alpha)vn_y & \alpha n_y \\ U(\theta^2 - H_T) & H_T n_x - \alpha uU & H_T n_y - \alpha vU & (1+\alpha)U \end{bmatrix}$$

where

$$\theta^2 = \partial P/\partial \rho = C^2 - \alpha(H_T - q^2)$$

$$q^2 = u^2 + v^2$$

The D matrix can been shown to be equivalent to the corresponding matrix for an ideal gas by noting that, for an ideal gas

$$\alpha = \gamma - 1$$

$$\beta = 1/T$$

$$\kappa = 1/P$$

$$\theta^2 = 0.5(\gamma - 1)q^2.$$

The eigenvalues for the matrix D are obtained by setting the determinant of D to zero and solving for the roots. The eigenvalues are equivalent to those for gases, namely

$$\lambda = [U,\ U,\ U + nC,\ U - nC]$$

where $n = (n_x^2 + n_y^2)^{0.5}$.

The eigenvector matrix for D is obtained by solving the following relationship for each of the four eigenvalues.

$$(D - \lambda)Q_n = 0$$

In expanded form the above relationship becomes

$$\begin{bmatrix} -\lambda & n_x & n_y & 0 \\ -uU+n_x\theta^2 & U+(1-\alpha)un_x-\lambda & un_y-\alpha vn_y & \alpha n_x \\ -vU+n_y\theta^2 & vn_x-\alpha un_y & U+(1-\alpha)vny-\lambda & \alpha n_y \\ U(\theta^2-H_T) & H_Tn_x-\alpha uU & H_Tn_y-\alpha vU & (1+\alpha)U-\lambda \end{bmatrix} Q_n = 0$$

The resultant eigenvector matrix is

$$M_D = \begin{bmatrix} 1 & 0 & 1 & 1 \\ u & n_y & m_1 & m_4 \\ v & -n_x & m_2 & m_5 \\ q^2-\theta^2/\alpha & -V & m_3 & m_6 \end{bmatrix}$$

where $V = n_xv - n_yu$

$m_1 = u + n_xC/n$

$m_2 = v + n_yC/n$

$m_3 = H_T + UC/n$

$m_4 = u - n_xC/n$

$m_5 = v - n_yC/n$

$m_6 = H_T - UC/n$

and C is the speed of sound. The determinant of the eigenvector martix is

$$|M_D| = 2\ C^3\ n/\alpha$$

The inverse of M_D is obtained using the standard formula

$$M_D^{-1} = M_{ji}/\ |M_D|$$

where $M_{ij} = (-1)^{i+j}c_{ij}$ and c_{ij} are the minors of M_D. Then

$$M_D^{-1} = (\alpha/C^2)\begin{bmatrix} H_T-q^2 & u & v & -1 \\ VC^2/\alpha n^2 & n_yC^2/\alpha n^2 & -n_xC^2/\alpha n^2 & 0 \\ (\theta^2-UC/n)/2\alpha & (n_xC/\alpha n-u)/2 & (n_yC/\alpha n-v)/2 & 1/2 \\ (\theta^2+UC/n)/2\alpha & -(n_xC/\alpha n+u)/2 & -(n_yC/\alpha n+v)/2 & 1/2 \end{bmatrix}$$

It has been verified that $M_DM_D^{-1}$ is equal to the identity matrix.

The matrix D may be spectrally decomposed into components corresponding to each of the eigenvalues by using the spectral theorem. Since two of the eigenvalues are identical the decomposition results in only three components. These components are obtained by performing the following matrix multiplications

$$D = M_D \quad U\begin{bmatrix} 1 & & & \\ & 1 & & \\ & & 0 & \\ & & & 0 \end{bmatrix} + (U+nC)\begin{bmatrix} 0 & & & \\ & 0 & & \\ & & 1 & \\ & & & 0 \end{bmatrix} + (U-nC)\begin{bmatrix} 0 & & & \\ & 0 & & \\ & & 0 & \\ & & & 1 \end{bmatrix} \quad M_D^{-1}$$

or

$$D = D_1 + D_2 + D_3$$

$$D_1 = (\alpha\ U/C^2) \times$$

$$\begin{bmatrix} (C^2-\theta^2)/\alpha & u & v & -1 \\ (n_xUC^2/n^2-u\theta^2)/\alpha & u^2+n_y{}^2C^2/\alpha n^2 & uv-n_xn_yC^2/\alpha n^2 & -u \\ (n_yUC^2/n^2-v\theta^2)/\alpha & uv-n_xn_yC^2/\alpha n^2 & v^2+n_x{}^2C^2/\alpha n^2 & -v \\ (U^2C^2/n^2-\theta^2H_T)/\alpha & u\omega-n_yVC^2/\alpha n^2 & v\omega+n_xVC^2/\alpha n^2 & -\omega \end{bmatrix}$$

where $\omega = q^2 - \theta^2/\alpha$

$$D_2 = \alpha(U+nC)/2C^2 \begin{bmatrix} W_1 & W_2 & W_3 & 1 \\ W_1m_1 & W_2m_1 & W_3m_1 & m_1 \\ W_1m_2 & W_2m_2 & W_3m_2 & m_2 \\ W_1m_3 & W_2m_3 & W_3m_3 & m_3 \end{bmatrix}$$

where $W_1 = (\theta^2 - UC/n)/\alpha$

$W_2 = (n_xC/\alpha n - u)$

$W_3 = (n_yC/\alpha n - v)$

$$D_3 = \alpha(U-nC)/2C^2 \begin{bmatrix} W_4 & W_5 & W_6 & 1 \\ W_4m_4 & W_5m_4 & W_6m_4 & m_4 \\ W_4m_5 & W_5m_5 & W_6m_5 & m_5 \\ W_4m_6 & W_5m_6 & W_6m_6 & m_6 \end{bmatrix}$$

where

$W_4 = (\theta^2 + UC/n)/\alpha$

$W_5 = -(n_xC/\alpha n + u)$

$W_6 = -(n_yC/\alpha n + v)$

The quantity DQ_n now becomes $(D_1 + D_2 + D_3)Q_n$ where D_1 has eigen direction U, D_2 has eigen direction $\bar{U} + nC$ and D_3 has eigen direction $U - nC$. Recall that DQ_n represents either

$$\hat{F}_\xi = (\hat{F}_1)_\xi + (\hat{F}_2)_\xi + (\hat{F}_3)_\xi$$

or $$\hat{G}_\eta = (\hat{G}_1)_\eta + (\hat{G}_2)_\eta + (\hat{G}_3)_\eta$$

The components D_1, D_2 and D_3 may be simplified by applying the chain rule to replace derivatives of (ρE_T) with derivatives of P. The equation for the differential form of the internal energy, dE, from section 2.3 may be expanded to the differential of the total energy, dE_T, to give

$$dE_T = C_v dT - (\beta T/\kappa - P)d\rho/\rho^2 + qdq$$

But

$$dT = \kappa dP/\beta - d\rho/\beta\rho$$

$$d(\rho E_T) = \rho dE_T + E_T d\rho$$

$$d(\rho q) = \rho dq + q d\rho$$

Combining the above four relations yields

$$d(\rho E_T) = dP/\alpha - \theta^2 d\rho/\alpha + ud(\rho u) + vd(\rho v)$$

Substituting the above equation into the three components of D eliminates many of the terms in the matrices. Another simplification involves using the chain rule to replace $(\rho u)_n$ and $(\rho v)_n$ with $(\rho U)_n$ and $(\rho V)_n$. These two operations reduce the complicated component matrices into much more simplified forms, namely:

$$D_i Q_n = D^*_i Q^*_n, \quad \text{where } Q^* = [\rho,\ \rho U,\ \rho V,\ P]^T \quad \text{and}$$

$$D^*_1 = U \begin{bmatrix} 1 & 0 & 0 & -1/C^2 \\ n_x U/n^2 & 0 & -n_y/n^2 & -u/C^2 \\ n_y U/n^2 & 0 & n_x/n^2 & -v/C^2 \\ U^2/n^2 - \theta^2/\alpha & 0 & V/n^2 & -\omega/C^2 \end{bmatrix}$$

$$D^*_2 = \frac{U+nC}{2nC} \begin{bmatrix} -U & 1 & 0 & n/C \\ -Um_1 & m_1 & 0 & m_1 n/C \\ -Um_2 & m_2 & 0 & m_2 n/C \\ -Um_3 & m_3 & 0 & m_3 n/C \end{bmatrix}$$

$$D^*_3 = \frac{U-nC}{2nC} \begin{bmatrix} U & -1 & 0 & n/C \\ Um_4 & -m_4 & 0 & m_4 n/ \\ Um_5 & -m_5 & 0 & m_5 n/C \\ Um_6 & -m_6 & 0 & m_6 n/C \end{bmatrix}$$

$D^*_1Q^*_n$ can be expanded by noting that

$$(\rho U)_n = (\rho U)_n$$

$$(\rho uU)_n = -uU\rho_n + (u + n_xU/n^2)(\rho U)_n - (n_yU/n^2)(\rho V)_n$$

$$(\rho vU)_n = -vU\rho_n + (v + n_yU/n^2)(\rho U)_n + (n_xU/n^2)(\rho V)_n$$

$$(\rho UH_T)_n = -U(H_T + \theta^2/\alpha)\rho_n + (H_T + U^2/n^2)(\rho U)_n + (UV/n^2)(\rho V)_n + U(\alpha + 1)P_n/\alpha$$

Substituting the above relations into $D^*_1Q^*_1$ puts the actual fluxes back into the algorithm. The algorithm then becomes the fluxes plus biases in the windward directions. $D^*_1Q^*_n$ becomes

$$D^*_1Q^*_1 = F_n + [U\rho_n - (\rho U)_n] \begin{bmatrix} 1 \\ a_1 \\ a_2 \\ a_3 \end{bmatrix} - nP_n/C^2 \begin{bmatrix} U/n \\ b_1 \\ b_2 \\ b_3 \end{bmatrix}$$

where F_n is either of the original flux vectors, $\hat{F}$ or $\hat{G}$, and

$$a_1 = u + n_xU/n^2$$

$$a_2 = v + n_yU/n^2$$

$$a_3 = H_T + U^2/n^2$$

$$b_1 = (uU + n_xC^2)/n$$

$$b_2 = (vU + n_yC^2)/n$$

$$b_3 = U(H_T + C^2)/n$$

Defining several convenient groupings of parameters

$$f_1 = [U\rho_n - (\rho U)_n] \begin{bmatrix} 1 \\ a_1 \\ a_2 \\ a_3 \end{bmatrix} \qquad f_2 = nP_n/C^2 \begin{bmatrix} U/n \\ b_1 \\ b_2 \\ b_3 \end{bmatrix}$$

$$f_3 = [U\rho_n - (\rho U)_n]/C \begin{bmatrix} U/n \\ b_1 \\ b_2 \\ b_3 \end{bmatrix} \qquad f_4 = nP_n/C \begin{bmatrix} 1 \\ a_1 \\ a_2 \\ a_3 \end{bmatrix}$$

then $D^*_1Q^*_n = (F_1)_n = F_n + f_1 - f_2$

$D^*_2Q^*_n$ and $D^*_3Q^*_n$ can also be expanded to yield

$$D^*_2Q^*_n = (F_2)_n = 0.5(f_2 - f_1) + 0.5(f_4 - f_3)$$

$$D^*_3Q^*_n = (F_3)_n = 0.5(f_2 - f_1) - 0.5(f_4 - f_3)$$

Again the eigen directions of F_1, F_2 and F_3 are U, U + nC and U - nC, respectively.

Once the flux components have been evaluated, the windward algorithm determines which nodes in the element receive each of the flux components. The windward algorithm is stated as:

$$F_n = e_1(F_1)_n + e_2(F_2)_n + e_3(F_3)_n$$

where: $e_1 = 1$ if $U \geq 0$

$= 0$ if $U < 0$

$e_2 = 1$ if $U + nC \geq 0$

$= 0$ if $U + nC < 0$

$e_3 = 1$ if $U - nC \geq 0$

0 if $U - nC < 0$

For supersonic flow, which is unlikely for liquid flows, $e_1 = e_2 = e_3$, so that

$$F_n = e_1(F_1 + F_2 + F_3)_n$$

$$= e_1[F + f_1 - f_2 + 0.5 (f_2 - f_1 + f_4 - f_3)$$

$$+ 0.5 (f_2 - f_1 - f_4 + f_3)]$$

$$= e_1F = e_1(F)_n$$

For subsonic flow where U < nC the e's may be redefined as:

$$e_1 = 0.5(1 + \varepsilon_1), \quad \text{where } \varepsilon_1 = \text{SIGN}(U)$$

$$e_2 = 0.5(1 + \varepsilon_2), \quad \text{where } \varepsilon_2 = \text{SIGN}(U+nC) = \text{SIGN}(n)$$

$$e_3 = 0.5(1 + \varepsilon_3), \quad \text{where } \varepsilon_3 = \text{SIGN}(U-nC) = \text{SIGN}(-n) = -\varepsilon_2$$

In subsonic flow any node in the flow grid will have either e_2 or e_3 equal to unity and the other equal to zero, therefore for any node

$$F_n = 0.5[(1+\varepsilon_1)F + \varepsilon_1(f_1-f_2) + \varepsilon_2(f_4-f_3)]$$

By simply evaluating the signs on U for supersonic flow and for U and n for subsonic flow the algorithm automatically determines the proper directions in which to difference the three components of the flux vectors. The method by which the differencing is accomplished in LWIND is described below.

LWIND employs a numbering system convention which applies to each element in the flow field regardless of orientation. This numbering system is detailed below.

Typical Element

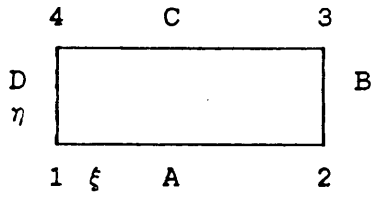

Nodes: 1 - 4
Faces: A - D
Elements do not need to be rectangles; sketch indicates numbering system only.

The position vector for any point in the element is $P = [x, y]^T$ or

$$P = (1-\xi)(1-\eta)P_1 + \xi(1-\eta)P_2 + \xi\eta P_3 + (1-\xi)\eta P_4$$

$$P_\xi = (1-\eta)(P_2 - P_1) + \eta(P_3 - P_4)$$

$$P_\eta = (1-\xi)(P_4 - P_1) + \xi(P_3 - P_2)$$

$$|A| = x_\xi\, y_\eta - x_\eta\, y_\xi = 1/J$$

In order to understand the physical interpretation of the equations used in the algorithm, first note that the outward-pointing normals

$$\vec{N} = N_x \vec{i} + N_y \vec{j}$$

on each face of the element are:

Face	N_x	N_y
A	y_2-y_1	x_1-x_2
B	y_3-y_2	x_2-x_3
C	y_4-y_3	x_3-x_4
D	y_1-y_4	x_4-x_1

Evaluation of the derivatives P_ξ and P_η at each node of the element yields

Node	x_ξ	y_ξ	x_η	y_η
1	x_2-x_1	y_2-y_1	x_4-x_1	y_4-y_1
2	x_2-x_1	y_2-y_1	x_3-x_2	y_3-y_2
3	x_3-x_4	y_3-y_4	x_3-x_2	y_3-y_2
4	x_3-x_4	y_3-y_4	x_4-x_1	y_4-y_1

But from before

$$\xi_x = J\, y_\eta \qquad \eta_x = -J\, y_\xi$$

$$\xi_y = -J\, x_\eta \qquad \eta_y = J\, x_\xi$$

so that

Node	ξ_x	ξ_y	η_x	η_y
1	$-J_1 N_{xD}$	$-J_1 N_{yD}$	$-J_1 N_{xA}$	$-J_1 N_{yA}$
2	$J_2 N_{xB}$	$J_2 N_{yB}$	$-J_2 N_{xA}$	$-J_2 N_{yA}$
3	$J_3 N_{xB}$	$J_3 N_{yB}$	$J_3 N_{xC}$	$J_3 N_{yC}$
4	$-J_4 N_{xD}$	$-J_4 N_{yD}$	$J_4 N_{xC}$	$J_4 N_{yC}$

Therefore $\nabla\xi/J$ and $\nabla\eta/J$ are area normals at the 2 faces associated with each node in the positive ξ and η directions. U is the dot product of the velocity vector and the area normal vector. Consequently, the local computational coordinate form of the conservation equations represents the fluxes through the faces of the element and are, in fact, identical to the flux integral form of the conservation equations. LWIND departs from standard finite difference methods at this point by employing the integral form of the equations and actually integrating the fluxes through each element. This results in a finite volume integral approach using a windward algorithm.

The above table reveals that ξ_x and ξ_y involve only the normals on faces B and D of the typical element while η_x and η_y only involve the normals on faces A and C. Consequently,

$\hat{F}$ is evaluated only on faces B and D while $\hat{G}$ is evaluated only on faces A and C.

The adopted convention for the typical element, with its numbering system for the nodes and faces relative to the ξ and η directions, dictates the following for ε_2 = SIGN(n). The outward-pointing normal for face B points in the direction of positive ξ while the outward-pointing normal for face D points in the negative ξ direction. Therefore,

ε_2 = 1 for nodes 2 & 3 for $\hat{F}_\xi$

= -1 for nodes 1 & 4 for $\hat{F}_\xi$

Likewise, the outward-pointing normal directions for faces A and C dictate that

ε_2 = 1 for nodes 3 & 4 for $\hat{G}_\eta$

= -1 for nodes 1 & 2 for $\hat{G}_\eta$

If U_a is defined as the average U in either the ξ or η direction, recalling that U is the dot product of the velocity and area normal vectors, then, since the area normal vectors on opposite faces have opposite signs, the following is true:

ε_1 = SIGN(U_a) for nodes 2 & 3 for $\hat{F}_\xi$

= -SIGN(U_a) for nodes 1 & 4 for $\hat{F}_\xi$

ε_1 = SIGN(U_a) for nodes 3 & 4 for $\hat{G}_\eta$

= -SIGN(U_a) for nodes 1 & 2 for $\hat{G}_\eta$

Applying the above conventions for ε_1 and ε_2 to the equation for F_n and noting that each node on a face receives half of F_n

yields:

For nodes 2 & 3 (for $\hat{F}_\xi$) or nodes 3 & 4 (for $\hat{G}_\eta$),

$$F^+ = 0.25[(1 + \varepsilon_1)F + \varepsilon_1(f_1 - f_2) + (f_4 - f_3)]$$

For the opposite nodes,

$$F^- = 0.25[(1 - \varepsilon_1)F - \varepsilon_1(f_1 - f_2) - (f_4 - f_3)]$$

or

$$F^\pm = 0.25[(1 \pm \varepsilon_1)F \pm \varepsilon_1(f_1 - f_2) \pm (f_4 - f_3)]$$

$$= 0.25F_n \pm 0.25(\varepsilon_1 F_n + B]$$

where

$$B = \varepsilon_1(f_1 - f_2) + (f_4 - f_3)$$

The flux equation consists of a center differenced term involving F_ξ or G_η only and a bias term B which is windward differenced but sums to zero over the element, thus ensuring the integral conservation of the flow equations over the element.

The bias term B can be simplified using the following groupings of parameters:

$$b_1 = \varepsilon_1 C - U/n$$

$$b_2 = \varepsilon_1 U/n - C$$

$$b_3 = [U\rho_n - (\rho U)_n]b_1/C - nP_n b_2/C^2$$

$$b_4 = [U\rho_n - (\rho U)_n]b_2 - nP_n b_1/C$$

Then

$$B = \begin{bmatrix} b_3 \\ b_3 u + b_4 n_x/n \\ b_3 v + b_4 n_y/n \\ b_3 H_T + b_4 U/n \end{bmatrix}$$

The above derivation results in a finite volume, totally conservative, windward algorithm consisting of center differenced fluxes with a windward bias involving no time-consuming matrix multiplications.

Appendix B - FDNS

The Navier Stokes conservation equations to be solved, along with k-ϵ turbulence model equations, are given below in curvilinear coordinates.

$$J^{-1}(\partial \rho q/\partial t) = \partial[-\rho U_i q + \mu G_{ij}(\partial q/\partial \xi_j)]/\partial \xi_i + S_q$$

where U_i = 1, u, v, w, h, k, and ϵ, respectively, for mass, momentum, enthalpy, turbulent kinetic energy, and turbulent kinetic energy dissipation conservation. J, U_i, and G_{ij} are given by

$$J = \varphi(\xi,\eta,\zeta)/\partial(x,y,z)$$

$$U_i = (u_j/J)(\partial \xi_i/\partial x_j)$$

$$G_{ij} = (\partial \xi_i/\partial x_k)(\partial \xi_j/\partial x_k)/J$$

Also, $\mu = (\mu_l + \mu_t)/\sigma_q$ is the effective viscosity when the turbulent eddy viscosity is used to model turbulent flows. The turbulent eddy viscosity is $\mu_t = \rho C_\mu k^2/\epsilon$; C_μ and σ_q are turbulent modeling constants. Wall functions are used to reduce the number of grid points required very near no-slip walls.

The source terms are given by:

$$S_q = J^{-1}\begin{bmatrix} 0 \\ -p_x + \nabla[\mu(u_j)_x] \\ -p_y + \nabla[\mu(u_j)_y] \\ -p_z + \nabla[\mu(u_j)_z] \\ \Phi \\ \rho(P_r - \epsilon) \\ (\rho\epsilon/k)(C_1P_r - C_2\epsilon + C_3P_r^2/\epsilon) \end{bmatrix}$$

An upwind scheme is used to approximate the convective terms of the momentum, energy, and continuity equations; the scheme is based on second and fourth order central differencing with artificial dissipation. First order upwinding is used for the turbulence equations since the parameters involved are all positive quantities. Different eigenvalues are used for weighing the dissipation terms depending on the conserved quantity being evaluated, in order to give correct diffusion fluxes near wall

boundaries (Ref. B1). This procedure is different from those proposed by other investigators (Refs. B2 - B4) in which the sum of the absolute value of the convective velocity and the local sound speed is used to weigh the dissipation terms. For simplicity, consider fluxes in the ξ-direction only. That is:

$$\partial F/\partial \xi \simeq 0.5(F_{i+1} - F_{i-1}) - (d_{i+1/2} - d_{i-1/2})$$

A general form of the dissipation term is given as follows.

$$d_{i+1/2} = 0.5[\epsilon_1|\rho U|]_{i+1/2}(q_{i+1} - q_i) + [\epsilon_2(1-\epsilon_1)\ MAX\{0.5\Delta s\rho(|u|,|v|),$$

$$2|\rho U|\} + \epsilon_3\Delta s]_{i+1/2}(q_{i-1} - 3q_i + 3q_{i+1} - q_{i+2})$$

where: d_1 = REC (upwinding control parameter) and $d_3 = 0.005$

Different values for ϵ_1, ϵ_2, and ϵ_3 are used for the continuity, energy and momentum equations, as shown in Table 1.

Table 1. Dissipation Parameters

	Momentum & Energy	Continuity
ϵ_1	d_1	0
ϵ_2	0.015	0
ϵ_3	0	d_3

To maintain time accuracy, a time-centered, time-marching scheme with a multiple pressure corrector algorithm is employed. In general, a noniterative time-marching scheme is used for time dependent flow computations; however, pressure corrector subiterations can be used if necessary. The pressure corrector scheme is described as follows. A simplified momentum equation was combined with the continuity equation to form a pressure correction equation. This equation is:

$$\partial \rho u_i/\partial t \simeq - \nabla p'$$

or in discrete form:

$$u_i' \simeq - \beta(\Delta t/\rho)\nabla p' \qquad (1)$$

where β represents a pressure relaxation parameter ($\beta = 10$ is typical). The velocity field in the continuity equation is then perturbed to form a correction equation. That is:

$$\nabla(\rho u_i)^{n+1} = \nabla[\rho^n(u_i^n + u_i')] = 0$$

or,

$$\nabla(\rho u_i') = - \nabla(\rho u_i)^n$$

Substituting equation (1) into (2), the following pressure correction equation is obtained.

$$- \nabla(\beta \Delta t \nabla p') = - \nabla(\rho u_i)^n \qquad (3)$$

Once the solution of equation (3) is obtained, the velocity field and the pressure field are updated through equation (1) and the following relation:

$$p^{n+1} = p^n + p'$$

To ensure that the updated velocity and pressure fields satisfy the continuity equation, the pressure correction procedure is repeated several times (usually 4 times is sufficient) before marching to the next time step. This constitutes a multi-corrector subiteration procedure.

For the description of cavitating flow, an additional conservation equation for the gas phase is required. This equation contains a source term, ρW_t, which is evaluated as follows: Derivation of the bubble growth rate two-phase model follows the method given in (Ref. B5), the basic equations used in this model are the Clausius-Clapeyron equation and the simplified one-dimensional momentum and energy equations. The final expression can be written as:

$$dm/dp = (v_{fg}/h_{fg}) \ (m - CT/h_{fg})$$

where m, p, v, h, C and T represent the mass fraction (or quality) of the bubbly phase, pressure, specific volume, enthalpy, specific heat and fluid temperature respectively. The subscript $_{fg}$ denotes differences due to phase change.

The rate of production of heterogeneous nuclei per unit volume as proposed in (Ref. B6) is:

$$dn/dt = N_n(2\sigma/M\pi)^{0.5} \exp[-(16\pi\sigma^3\delta/3\kappa T)/(p_g - p_f)^2]$$

where: N_n, number of heterogeneous nucleation sites per unit volume;

σ, surface tension of oxygen;

M, mass of a mulecule;

κ, Boltzmann's Constant;

δ, function of bubble contact angle. (assumed to be unity in this study);

p_g; vapor pressure at temperature, T; and

p_f; fluid pressure.

By combining these equations, an expression for the bubble growth rate results:

$$dr/dt = [K_f R^2 T_f^2 / h_{fg}^2 p_g^2 (3Kt/\pi)^{0.5}] \; (p_g^2/p_{gr}) \; \ln(p_g/p_{gr})$$

where: K_f, thermal conductivity of fluid;

K, thermal diffusivity of fluid;

p_{gr}, pressure inside a bubble of radius, r;

R, gas constant.

Finally, the source term for the mass fraction equation can be written as:

$$\rho W_t = \rho_g (1-\alpha) \; (4\pi/3) \; (U/\Delta s) \; (dn/dt)(dr/dt)^3$$

where s is an average cell size and the volume fraction, α, can be calculated from the following homogeneous relation:

$$\alpha = m(\rho_f/\rho_g)/[1 + m(\rho_f/\rho_g - 1)]$$

References for Appendix B

B1. Chen, Y.S., "Compressible and Incompressible Flow Computations with a Pressure Based Method," AIAA Paper 89-0286 (1989).

B2. Harten, A., "High Resolution Schemes for Hyperbolic Conservation Laws," J. Comp. Physics, 49, pp. 357-393 (1983).

B3. McCormack, R.W., "Current Status of Numerical Solutions of the Navier-Stokes Equations," AIAA Paper 85-0032 (1985).

B4. Jameson, A., et al, "Numerical Solution of the Euler Equations by Finite Volume Methods Using Runge-Kutta Time Stepping Schemes," AIAA Paper 81-1259 (1981).

B5. Rohatgi, U.S. and Reshotko, E., "Non-Equilibrium One-Dimensional Two-Phase Flow in Variable Area Channels," Symp. on Two Phase Flow, Proc. Instn. Mech. Engrs., 1976.

B6. Simpson, H.C. and Silver, R.S., "Theory of One-Dimensional, Two-phase Homogeneous Non-equilibrium Flow," Symp. on Two Phase Flow, Proc. Instn. Mech. Engrs., pp. 45-56, 1962.